Dissertation zur Erlangung des
Doktorgrades der Naturwissenschaften (Dr. rer. nat.)
im Fachbereich Geowissenschaften der Freien Universität Berlin

Oceanographic applications of GRACE gravity data on global and regional scales

Inga Bergmann-Wolf
Berlin, Juni 2015

Institut für Meteorologie
Freie Universität Berlin

1. Gutachter:	Prof. Dr. Maik Thomas
2. Gutachter:	Prof. Dr. Frank Flechtner

Tag der Einreichung:	09.06.2015
Tag der Disputation:	27.10.2015

Eidesstattliche Erklärung

Hiermit versichere ich, die vorliegende Dissertation selbstständig und ohne unerlaubte Hilfe angefertigt zu haben. Es wurden keine anderen als die im Text aufgeführten Hilfsmittel und Quellen verwendet. Ein Promotionsverfahren wurde zu keinem früheren Zeitpunkt an einer anderen Hochschule oder bei einem anderen Fachbereich beantragt.

Inga Bergmann-Wolf
Berlin, Juni 2015

Abstract

This work demonstrates applications of GRACE gravity data on oceanographically relevant questions concerning global eustatic sea level rise and water mass transport in the region of the Antarctic Circumpolar Current (ACC). Due to the development of the background model OMCT in the AOD1B product from RL04 to RL05 during the preparation of this work GRACE data of two releases (RL04 and RL05) will be used for each application. Therefore, a description of the improvements of the latest RL05 will be given.

Transport variations in the ACC region will be estimated from three temporally different GRACE solutions (GFZ RL04, CNES/GRGS RL02, ITG-GRACE2010) and will be compared to in situ observations of ocean bottom pressure from OBP recorders and sea level variations from tide gauge stations along the Antarctic continent. Connections of the mean atmospheric dynamics of the Southern Hemisphere to the transport variations will be made by comparing the transport time series to the Southern Annular Mode index.

Estimations of the global ocean mass variations will be made with the current RL05 solutions of GFZ. Therefore, the problem of including degree-1 information in the GRACE data will be discussed by enhancing the determination method of Swenson *et al.* (2008). Also the impact of including a homogeneous distributed eustatic signal or regionally different due to effects of Loading and Self-Attraction will be assessed.

Kurzfassung

Diese Arbeit demonstriert ozeanographische Anwendungsmöglichkeiten von GRACE Schwerefelddaten. Es werden zum einen der eustatische Anteil am globalen Meeresspiegelanstieg ermittelt und zum anderen Massentransportvariationen im Bereich des Antarktischen Zirkumpolarstroms (ACC) aus den GRACE Daten abgeleitet. Da während der Bearbeitungszeit beider Themen gleichzeitig eine Weiterentwicklung des Ozeanmodells OMCT des AOD1B Produktes für die GRACE Prozessierung stattgefunden hat, werden jeweils verschiedene GRACE Lösungen (RL04 und RL05) für die jeweiligen Anwendungen verwendet. Zudem erfolgt eine Beschreibung der Weiterentwicklung des neuen Release 05.

Transportvariationen des ACCs werden mit drei unterschiedlich zeitlich aufgelösten GRACE Lösungen ermittelt (GFZ RL04, CNES/GRGS RL02, ITG-GRACE2010) und anschließend mit in situ Beobachtungen von Ozeanbodendruckrekordern und Meeresspiegelvariationen von Pegelstationen entlang der antarktischen Küste verglichen. Vergleiche der Zeitreihen von Transportvariationen und dem Klimaindex der Southern Annular Mode geben Aufschluss über den Einfluss der mittleren Atmosphärendynamik auf der Südhalbkugel auf den Massentransport im ACC.

Die Ableitung globaler Ozeanmassenvariationen erfolgt auf Grundlage der aktuellen RL05 Lösungen des GFZ. Hierbei wird besonders auf die Problematik der Grad-1 Terme eingegangen. Dafür wird die Methode von Swenson *et al.* (2008) zur Ableitung von Grad-1 Termen aus den GRACE Schwerefeldlösungen weiterentwickelt. Es erfolgt zudem eine Abschätzung des Einflusses des eustatischen Signals und wie dieses in die Prozessierung eingebracht wird. Hierbei werden eine homogene und eine regional unterschiedliche Verteilung, die sich durch die Berücksichtigung von Auflast- und Selbstanziehungseffekten ergibt, untersucht.

Contents

List of Figures

List of Tables

List of Acronyms

ACC	Antarctic Circumpolar Current
AOD1B	Atmosphere and Ocean De-Aliasing Level-1B product
AWI	Alfred-Wegener-Institute
BODC	British Oceanographic Data Centre
CESM	Community Earth System Model
CF	Center of Figure system
CM	Center of Mass system
CNES	Centre National d'Etudes Spatiales
CPC	Climate Prediction Centre
CSR	Center for Space Research, University of Texas
DLR	National aeronautic and space research centre of Federal Republic of Germany
DORIS	Doppler Orbit determination and Radio positioning Integrated on Satellite
ECCO	Estimating the Circulation and Climate of the Ocean model
ECMWF	European Centre for Medium-Range Weather Forecast
ENSO	El Niño Southern Oscillation
EOF	Empirical Orthogonal Function
ESM	Earth System Model
FES2004	Finite Element Solutions tidal model 2004
FRAM	Fine Resolution Antarctic Model
GAA	non-tidal contribution of atmosphere
GAB	non-tidal contribution of ocean
GAC	sum of GAA and GAB
GAD	sum of GAA and GAB but continents were set to zero
GAST	Greenwich Apparent Sidereal Time
GECCO-2	German part of ECCO synthesis for 2002 - 2007
GFZ	GeoForschungsZentrum Potsdam
GIA	Glacial Isostatic Adjustment
GLOSS	Global Sea Level Observing System
GMSL	Global Mean Sea Level

GPS	Global Positioning System
GRACE	Gravity Recovery And Climate Experiment
GRACE-FO	GRACE Follow-On
GRGS	Groupe de Recherches de Géodésie Spatiale
GSM	Spherical Harmonics of Earth's gravity field
HOPE	Hamburg Ocean Primitive Equation Model
IB	Inverted Barometric correction
IERS	International Earth Rotation and Reference System Service
IPCC	Intergovernmental Panel on Climate Change
ISDC	Information System and Data Centre
JPL	Jet Propulsion Laboratory Pasadena
KBRR	K-Band Range Rate
LRI	Laser Ranging Interferometer
LSA	Loading and Self Attraction
LSDM	Land Surface Discharge Model
MOG2D	2D Gravity Wave Model
MPIOM	Max-Planck-Institute for Meteorology Ocean Model
MSL	Mean Sea Level
NAM	Northern Annular Mode
NDBC	National Data Buoy Centre
NOAA	National Oceanic and Atmospheric Administration
NTOL	Non-Tidal Ocean Loading
OBP	ocean bottom pressure
OBPR	Ocean Bottom Pressure Recorder
OCCAM	Ocean Circulation and Climate Advanced Model
OMCT	Ocean Model for Circulation and Tides
PDO	Pacific Decadal Oscillation
PO.DAAC	Physical Oceanography Distributed Active Archive Centre
PREM	Preliminary Reference Earth Model
PSMSL	Permanent Service for Mean Sea Level
RACMO-2	Regional Atmospheric Climate Model
RDC	Raw Data Centre
RMS	root mean square
RSL	Relative Sea Level
SACCF	Southern ACC Front

SAM	Southern Annular Mode
SAR	Synthetic Aperture Radar
SLP	Sea Level Pressure
SLR	Satellite Laser Ranging
SOI	Southern Ocean Index
STF	Subtropical Front

Chapter 1

Introduction

The world ocean covers approximately 71% of the Earth's surface. Separating the continents by the five major oceanic subdivisions (Pacific, Atlantic, Indian, Arctic and Southern Ocean), humans have always been searching for ways to cross the ocean for discovering new living environments. Voyages by sailing ships laid the basis of oceanographic measurements and for physical oceanography itself. Precise knowledge of winds and currents in the ocean as well as tidal dynamics due to sun and moon were necessary to find trading routes in the different ocean regions. During the last 5000 years, a wide collection of observations of e.g. wind, currents, waves, temperature, have been made by ships. In the second half of the 20th century, developments of new oceanographic instruments (Conductivity-Temperature-Depth device, eXpendible BathyThermographs) enabled the discovery of deep ocean processes in more detail. Nevertheless, until the end of the 20th century most of the oceans have been sparsely observed and were under sampled. The great breakthrough has been achieved by the launch of dedicated ocean-viewing satellites. Today, satellite data build up a fundamental data source for ocean processes on global, regional and local scales. Together with data from moored buoys, floating drifters , autonomous underwater vehicles, acoustic tomography and shipborn observations, processes in the ocean are resolved in all three dimensions.

One of the first techniques to study the ocean from space were ocean color remote sensing satellites equipped with passive radiometers working in the visible and near-infrared wavelengths (Robinson, 2004). The color of the ocean is an indicator of different water masses which are indirectly related to ocean currents. Also dynamical processes, mostly on meso scales, were determined from the color pattern. Further satellites were also able to measure the temperature of the ocean surface. This allowed detecting ocean features like e.g. tidal mixing, heat-exchange or mesoscale eddies. Active instruments sense the roughness of the

ocean surface and therefore the surface wind field (velocity and direction) and ocean surface itself (sea surface height, velocity). Further satellites are equipped with different active radar instruments. Satellites of the European Space Agency ERS-1 and ERS-2 consisted of scatterometer and Synthetic Aparture Radar (SAR) to measure the ocean surface roughness and also of a radar altimeter to measure the sea surface height at the same time. All those methods have in common that they are just observing the ocean surface. Observations of temporal changes in the Earth's gravity field by the Gravity Recovery And Climate Experiment (GRACE) satellite mission, launched in 2002, contributed to the exploration of deep oceanic processes. For the first time it is now possible to determine the amount of mass contributing to total global mean sea level change (Cazenave *et al.*, 2009; Chambers & Schroeter, 2011), and also the impact of water inflow from melting ice masses like glaciers or large ice sheets could be assessed (Wouters *et al.*, 2011).
Ocean bottom pressure (OBP) variations are determined from GRACE gravity field variations and used for mass transportation studies in the global ocean. By using GRACE based fields of OBP variations, transport variations in the ACC have been determined in the Southern Ocean. Results by Zlotnicki *et al.* (2007) showed transport differences for the three ocean basins (Pacific, Atlantic and Indian Ocean) in the Southern Ocean. Early studies by Wearn & Baker (1980) with in situ observation of OBP but also later by e.g. Ponte & Quinn (2009) with GRACE based OBP showed a correlation of ACC transport variations and the upper wind field.
Similar transport variations of the North Atlantic Meridional Overturning Circulation (AMOC) have been estimated from pressure differences of in situ observations of the western and eastern boundary of the Atlantic Ocean for a specific latitude (Bingham & Hughes, 2008, 2009). Cromwell *et al.* (2007) started their feasibility study on these theoretical findings and used simulated data of OBP and sea surface height (SSH) for estimating the total geostrophic flow which allows the estimation of the full depth mass transport of the AMOC. They suggested the application of this method on satellite based observations for time series longer than a decade minimum due to the influence of trend signals and the correct determination of them. The better differentiation of mass and steric based contributions to total sea level variations provides also the opportunity to assess the heat budget of the deeper ocean regions which is not observed by Argo drifters (Llovel *et al.*, 2014).

Since the launch of the twin-satellites in 2002, GRACE gravity field observations proofed their ability for many different oceanographic applications. Due to the measurement principle a number of processing steps are necessary to get applicable data. Background models of tidal and non-tidal short term processes of atmospheric and oceanic variations need to be applied (Flechtner & Dobslaw, 2013). Additionally, filtering and decorrelation methods are

developed to reduce correlations in the higher spatial frequencies of the GRACE data which induce striping artifacts in the estimated gravity fields (Wahr *et al.*, 1998; Kusche, 2007). Also auxiliary data for variations of geocenter motion and the Earth's oblateness are needed, which are not or only poorly resolved by GRACE. Especially, including estimates of geocenter motion has a large impact on the precise determination of oceanic mass variations (Chambers, 2004).
During the mission lifetime of GRACE, five versions of standard monthly gravity field data have been released due to the fast development and ongoing improvement of the processing steps (Bettadpur, 2012; Dahle *et al.*, 2012; Watkins & Yuan, 2012). A good database of in situ observations is needed for a proper validation of each new release. Furthermore, end-to-end simulation studies with realistic earth system models, like the recently released ESA Earth System Model (Dobslaw *et al.*, 2016), are important to assess the error budget of newly developed processing strategies.

This work will provide oceanographic application examples of GRACE on global and regional scales. Therefore, the physical background for describing the Earth's gravity field and associated dynamical ocean processes will be given in Chapter 2. A detailed description of the GRACE mission and the postprocessing steps to obtain applicable data for further work is the topic of Chapter 3. After a short presentation of necessary steps in dealing with in situ observations (Chapter 4), the development of a new release of the Ocean Model for Circulation and Tides (OMCT) as a background model for the processing of GRACE will be described by extensive validation with a newly prepared in situ database (Chapter 5). The application of GRACE data on global scales will be the theme for Chapter 6. Therein, the impact of precisely estimated geocenter motion from GRACE data on global ocean mass variations will be assessed. The second application part (Chapter 7) will be focussed on the Southern Hemisphere and the coupling of the wind field and transport variations estimated from bottom pressure observations based on GRACE. Finally, a summary of this work will be given in Chapter 8 together with an outlook of future satellite gravity missions continuing the time series of observations from GRACE.

The content of this work and the results presented are based on a number of publications: Chapter 5 is based on Dobslaw *et al.* (2013); Zenner *et al.* (2014) and Dobslaw *et al.* (2016). Chapter 6.1 is published as Bergmann-Wolf *et al.* (2014); Chapter 7.1 is published as Bergmann & Dobslaw (2012); and Chapter 7.2 is based on Petrick *et al.* (2014).

Chapter 2

Theory

2.1 The Earth's gravity field

Any mass element at the Earth experiences a gravitational force and additionally a centrifugal force due to the Earth's rotation. The sum of both gives the force of gravity which is mainly a function of horizontal and vertical position and shows temporal variations.
The centrifugal force $\vec{z}$ is given by the constant angular velocity ω of the rotating Earth at a given point $\vec{p} = (x, y, z)$ with

$$\vec{z} = \omega^2 \vec{p} \tag{2.1}$$

The centrifugal force is sufficiently determined. Satellite observations are not affected by the Earth's rotation and therefore just monitor changes in the gravitational force field. From this point onwards, only the gravitational force will be taken into account.
A point mass will experience a gravitational acceleration of

$$\vec{b} = -G\frac{m}{l^2}\frac{\vec{l}}{l} \tag{2.2}$$

where G is the gravitational constant, m the mass situated at the attracting point and l the distance between two attracting masses. The gravitational acceleration at the point P is the sum of all mass elements. The vector field of the gravitational force outside the Earth is irrotational and therefore conservative and may be represented as the gradient of a potential. Therefore, the gravitational force is expressed as the gradient of the vector field and describes the gravitational potential V

$$V(l) = G\iiint \frac{dm}{l} = G\iiint \frac{\rho}{l} dv \tag{2.3}$$

where dv is the volume element of continuously distributed mass elements. The density ρ is a function of the radial distance to the Earth's mass center. The complete density distribution of the Earth is not known. Therefore, Eq. (2.3) cannot be used for the determination of the gravity field. As a first approximation, the Earth can be discretized by a sphere with a centrally symmetric density structure. Using spherical coordinates (radius r, colatitude θ, longitude λ), the gravitational potential is written as

$$V = G\rho dr \iint \frac{d\Omega}{l} \tag{2.4}$$

where $d\Omega = r^2 \sin\theta d\theta d\lambda$ is the surface element. At the exterior the gravitational potential fulfills Laplace's Differential Equation

$$\Delta V = 0 \tag{2.5}$$

which means, that the first and second order derivatives of the gravitational potential are also continuous functions, which defines them as harmonic functions (Torge, 1991). A solution of this differential equation is a series of expansion of the gravitational potential. Therefore, the reciprocal distance will be expanded with help of the Legendre Polynomials $P_l(\cos\theta)$ and the associated Legendre Functions $P_{lm}(\cos\theta)$. Using the surface harmonics

$$P_{lm}(\cos\theta)\cos m\lambda \qquad \text{and} \qquad P_{lm}(\cos\theta)\sin m\lambda \tag{2.6}$$

the gravitational potential is given as

$$V = \frac{GM}{r}\left(1 + \sum_{l=1}^{\infty}\sum_{m=0}^{l}\left(\frac{a}{r}\right)^l P_{lm}(\cos\theta)(C_{lm}\cos m\lambda + S_{lm}\sin m\lambda)\right) \tag{2.7}$$

The first term describes the potential of the Earth's mass M at the centre of mass. Gravity potential coefficients (C_{lm}, S_{lm}) for different degree l and order m determined from GRACE observations (see Chapter 3) are typically given as fully normalized potential coefficients using the fully normalized Legendre Functions $\tilde{P}_{lm}(\cos\theta)$ (Heiskanen & Moritz, 1967)

$$\tilde{P}_{lm}(\cos\theta) = \sqrt{k(2l+1)\frac{(l-m)!}{(l+m)!}}P_{lm}(\cos\theta) \qquad k = \begin{cases} 1 & \text{for } m = 0 \\ 2 & \text{for } m \neq 0 \end{cases} \tag{2.8}$$

2.1.1 Temporal surface gravity field variations

Temporal variations in the Earth's gravity field happen on the one side due to earth tides, ocean tides and variations in the rotation, on the other side due to non-tidal mass redistribution on the Earth's surface and in the interior. Gravimetric effects due to earth and oceanic tides by far have the largest effects. Forced by the gravitational attraction of Sun and Moon, diurnal and semi-diurnal signals are observable. Additionally, atmospheric tides contribute with periodical mass redistributions due to thermal effects in the atmosphere caused by the solar radiation. Solid Earth tides affect mainly the degree 2 terms but also induce changes in the degree 3 and 4 terms. Corrections of the Solid Earth tides follow the IERS conventions (Petit & Luzum, 2010) and have been applied in the GRACE processing (Dahle *et al.*, 2012). Large mass redistributions occur in the surface layer of atmosphere, ocean, cryosphere and hydrosphere as in the Solid Earth. A huge amount is described by the global water cycle where the water balance equation of precipitation, evapotranspiration and runoff of the total land water storage is balanced by variations in ocean and atmospheric mass. Besides the tidal variations in ocean and atmosphere, also longterm (annual or longer), seasonal and short term (a few days) variations are observed which have different spatial scales from large (ocean gyres) to small (meso-scale eddies) scales. In the atmosphere, weather phenomena like El Niño lead to large mass redistributions as well. In the glaciated regions, i.e. Greenland and Antarctica, besides the seasonal variations in ice thickness, an increasing melting is observable. Whereas just parts in Antarctica show increasing trends, the whole ice sheet of Greenland is affected. Also an interaction between increased ice runoff and seasonal variations in sea surface temperature of the coastal currents is detected (Murray *et al.*, 2010; Bergmann *et al.*, 2012). Due to the redistributions in the surface layer the Solid Earth beneath is affected due to loading effects. The largest signal is the still ongoing Glacial Isostatic Adjustment with secular signals of up to 4 cm equivalent water height per year (Peltier *et al.*, 2015).

By applying the assumption of Wahr *et al.* (1998) that all mass redistributions appear in a thin surface layer with a thickness of around 10–15 km, the mass variations are expressed as surface density variations $\Delta\sigma$

$$\Delta\sigma(\theta,\lambda) = a\rho_w \sum_{l=0}^{\infty}\sum_{m=0}^{l} \tilde{P}_{lm}(\cos\theta)(\Delta\hat{C}_{lm}\cos m\lambda + \Delta\hat{S}_{lm}\sin m\lambda) \tag{2.9}$$

where ρ_w is the density of water and $(\Delta\hat{C}_{lm}, \Delta\hat{S}_{lm})$ are the variations of the fully normalized surface mass coefficients. The fully normalized harmonic coefficients are related to the fully normalized surface mass coefficients via

$$\left\{ \begin{array}{c} \Delta C_{lm} \\ \Delta S_{lm} \end{array} \right\} = \frac{3\rho_w}{\rho_{ave}(2l+1)} \left(\left\{ \begin{array}{c} \Delta\hat{C}_{lm} \\ \Delta\hat{S}_{lm} \end{array} \right\} + k_l \left\{ \begin{array}{c} \Delta\hat{C}_{lm} \\ \Delta\hat{S}_{lm} \end{array} \right\} \right) \tag{2.10}$$

where ρ_{ave} is the mean density of the Earth and k_l are the Load Love numbers. The first term describes the direct gravitational effect due to mass redistributions. The second term results in the loading and the deformation of the underlying Earth due to the mass change. The vertical displacement is given with the Load Love numbers.
Finally, temporal variations of surface density are determined by changes in the fully normalized coefficients with

$$\Delta\sigma(\theta,\lambda) = \frac{a\rho_{ave}}{3} \sum_{l=0}^{\infty} \sum_{m=0}^{l} \frac{2l+1}{1+k_l} \tilde{P}_{lm}(\cos\theta)(\Delta C_{lm}\cos m\lambda + \Delta S_{lm}\sin m\lambda) \tag{2.11}$$

The surface density changes are also given as changes of equivalent water height ($\Delta h = \Delta\sigma/\rho_w$) or pressure changes by application of the hydrostatic equation ($\Delta p = \rho_w g \Delta h = g\Delta\sigma$).

2.1.2 Loading and self-attraction

In Eq. (2.11) changes in the gravitational potential due to loading and deformation of the Earth has been taken into account. Additionally, mass variations in the ocean lead to gravitational attraction to water masses at the current position and also from the far-field. This leads to deformation of the sea floor and therefore to additional load which then results in mass redistribution in the Earth's interior and to changes in the gravitational potential again. This effect is described as Loading and Self-Attraction (LSA) in the literature (e.g. Ray, 1998; Stepanov & Hughes, 2004). The phenomena is not restricted to the ocean but also appears in the atmosphere or hydrology.

The effect is described by two terms: first the additional mass deforms the seafloor. The Earths response like an elastic body for short term processes with

$$\Delta r_{el} = \frac{h_l V_l}{g} \tag{2.12}$$

where Δr_{el} is the vertical displacement of the Earth's crust and h_l the Love number. Due to this displacement, again a gravitational change (V_d) is induced with

$$V_d = k_l V_l \tag{2.13}$$

where k_l is the same Load Love Number as in Eq. (2.11). The potential change due to LSA is summarized according to Kuhlmann *et al.* (2013) as

$$V(p) = \frac{3}{\rho_{ave}} \sum_{l=0}^{\infty} (1 + k_l - h_l) \frac{1}{2l+1} p_{B,l}(\theta, \lambda) \tag{2.14}$$

where $p_{B,l}$ is the ocean bottom pressure change at a given location (θ, λ) and degree l.

Eq. (2.14) will be reformulated with a Green's Function for the potential change at the Earth's surface

$$\mathcal{G}(\theta) = \frac{R}{M_e} \sum_{l=0}^{\infty} (1 + k_l - h_l) P_l(\cos\theta) \tag{2.15}$$

For estimating the sea level change due to changes in the mass load of water and ice, Eq. (2.15) has to be convolved with the mass distribution of $p_{B,l}(\theta, \lambda)$ and integrated over the surface. This results in an integral equation, known as Sea Level Equation (Farrell & Clark, 1976).

The Sea Level Equation describes the mass redistribution between land and ocean in a gravitational consistent way. It attempts to correct the current sea level at time step t for the LSA effects. The current geoid height $n(\theta, \lambda, t)$ is defined as

$$n(\theta, \lambda, t) = e(\theta, \lambda, t) + h_{wl}(t) \tag{2.16}$$

where $e(\theta, \lambda, t)$ is the height of the reference equipotential surface and h_{wl} the shift between the reference and current equipotential surface due to mass redistributions. The relative sea level variations h_{RSL} are defined as

$$h_{RSL}(\theta, \lambda, t) = [n - u](\theta, \lambda, t) - [n - u](\theta, \lambda, t_0) \tag{2.17}$$

where u is the displacement of the equipotential surface. Applying the Sea Level Equation, the relative sea level variations are determined by

$$h_{RSL} = [h_{wl}(t) + e(\theta, \lambda, t) - u(\theta, \lambda, t)]\mathcal{O}(\theta, \lambda, t) \tag{2.18}$$

where $\mathcal{O}(\theta, \lambda, t)$ is the ocean function defining the area of land and ocean for the given time step. The homogeneous part h_{wl} describes the shift of the reference geoid

$$h_{wl}(t) = \frac{-M_{land}(t)}{\rho_{oce} A_{oce}(t)} - \frac{1}{A_{oce}} \int_{\Omega} [e(\theta, \lambda, t) - u(\theta, \lambda, t)] \mathcal{O}(\theta, \lambda, t) d\Omega \tag{2.19}$$

with the ocean area A_{oce}

$$A_{oce}(t) = \int_{\Omega} \mathcal{O}(\theta, \lambda, t) d\Omega \tag{2.20}$$

and M_{land} is the mass load of the land defined area affecting the ocean field. An iterative processing strategy for solving the Sea Level Equation is given in Klemann (2013). In the first step the sea level has to be determined from the surface mass redistributions. In the next step, the shift of the reference geoid is computed and then afterwards the relative sea level signal. With this new distribution of water mass the geoid is recalculated. Normally, the iteration converges very quickly after 3 to 5 cycles.

2.2 Ocean dynamics

As indicated in section 2.1.1, mass redistributions in the ocean lead to changes in the gravity field. For a given region, GRACE monitors the sum of mass changes in the ocean and the above atmosphere, usually defined as changes in the equivalent water column height and is further expressed as changes in ocean bottom pressure. Pressure gradients in the ocean are used to estimate water mass transport in specific regions, e.g. large ocean currents. In this section, the basic equations of ocean dynamics which are important for the following work are summarized.

2.2.1 Momentum equation and geostrophy

The dominant forces in the ocean are pressure gradients (∇p), Coriolis force ($2\vec{\Omega} \times \vec{v}$), gravity ($\vec{g}$) and friction ($\vec{F}_r$). The acceleration of a particle of water is expressed as (Pond & Pickard, 1983)

$$\frac{D\vec{v}}{Dt} = -\frac{1}{\rho} \nabla p - 2\vec{\Omega} \times \vec{v} + \vec{g} + \vec{F}_r \tag{2.21}$$

Expanding the derivatives by application of cartesian coordinates results in

$$\begin{aligned}
\frac{\partial u}{\partial t} + u\frac{\partial u}{\partial x} + v\frac{\partial u}{\partial y} + w\frac{\partial u}{\partial z} &= -\frac{1}{\rho}\frac{\partial p}{\partial x} + 2\Omega v \sin\phi + F_x \\
\frac{\partial v}{\partial t} + u\frac{\partial v}{\partial x} + v\frac{\partial v}{\partial y} + w\frac{\partial v}{\partial z} &= -\frac{1}{\rho}\frac{\partial p}{\partial y} - 2\Omega u \sin\phi + F_y \\
\frac{\partial w}{\partial t} + u\frac{\partial w}{\partial x} + v\frac{\partial w}{\partial y} + w\frac{\partial w}{\partial z} &= -\frac{1}{\rho}\frac{\partial p}{\partial z} + 2\Omega u \cos\phi - g + F_z
\end{aligned} \tag{2.22}$$

The simplest solution of this equation is an ocean at rest. This means, that the fluid is motion-less ($u, v, w = 0$) and will remain stationary ($du/dt = dv/dt = dw/dt = 0$) and there is no friction ($f_x = f_y = f_z = 0$). Eq. (2.22) simplifies to

$$\frac{1}{\rho}\frac{\partial p}{\partial x} = 0 \quad ; \quad \frac{1}{\rho}\frac{\partial p}{\partial y} = 0 \quad ; \quad \frac{1}{\rho}\frac{\partial p}{\partial z} = -g(\phi, z) \tag{2.23}$$

By integration of the third term, pressure p is determined at any given depth h (hydrostatic pressure equation)

$$p = \int_{-h}^{0} g(\phi, z)\rho(z)dz \tag{2.24}$$

Assuming a homogeneous ocean with constant gravity and density, pressure is given as

$$p = \rho g h \tag{2.25}$$

In the deeper ocean, beneath the Ekman Layer (see below), and for timescales longer than a few days, the ocean is assumed to be in geostrophic balance, i.e. the horizontal pressure gradient is in equilibrium with the Coriolis force. There is no acceleration in the current and the horizontal velocity is much larger than the vertical component. Eq. (2.22) is written as

$$\frac{\partial p}{\partial x} = \rho f v \quad ; \quad \frac{\partial p}{\partial y} = -\rho f u \quad ; \quad \frac{\partial p}{\partial z} = -\rho g \tag{2.26}$$

where $f = 2\Omega \sin\phi$ is the Coriolis parameter. Nevertheless, the geostrophic equations fail for flows with smaller spatial scales (less than 50km) and higher temporal variability (less than a few days). Near the Equator (latitudes lower than 2°) the geostrophic balance does not apply because the Coriolis force goes to zero.

2.2.2 Wind driven currents and mass transports

The time-averaged surface wind field differs regionally in direction and intensity due to the spatially varying distribution of solar heating and continental land masses, and to mass cir-

culation in the vertical planes of the atmosphere. In the mid latitudes from 40° to 60° strong westerly winds are located. Weak winds exist in the subtropics near 30° latitude. In the tropics, there are westward directed trade winds. In the Equator region weak winds from the east are observable (Stewart, 2008). The horizontal force of the wind fields excited on the oceans is described by the wind stress τ. Therefore, a vertical transfer of horizontal momentum occurs from the atmosphere in the ocean and sets the water masses into movement. Ongoing winds lead to a steady homogeneous horizontal flow in a thin surface layer, also called Ekman Layer. In this layer, a balance between frictional and Coriolis force is build up. The thickness varies between 45 and 300 m and the currents decrease exponentially with depth.

A series of papers by Sverdup, Stommel and Munk between 1947 and 1951 outlined the theory for wind-driven geostrophic currents. The main achievement was letting the Coriolis parameter vary by latitude. Also the friction has been taken into account. With those considerations, realistic currents could be calculated.

Sverdrup and Stommel developed the main theories for the connection of wind stress τ and the mass transport in the upper ocean layer and included the latitude dependence of the Coriolis force into the geostrophic equations. Finally, Munk combined the findings of Sverdrup and Stommel and included information from Rossby on lateral eddy viscosity. Therefore, he introduced two friction terms, one for the vertical and one for the lateral component. The vertical term is associated with the vertical shear to convey momentum from the wind stress applied at the surface into the Ekman layer. The lateral term is associated with the horizontal shear to force the ocean to remain in a steady-state circulation (Pond & Pickard, 1983). The wind-driven circulation is then described by a 4th-order differential equation

$$A\nabla^4\psi - \left(\frac{\partial f}{\partial x}\frac{\partial \psi}{\partial x}\right) - \mathrm{curl}_z(\tau) = 0 \tag{2.27}$$

where A is the eddy viscosity for lateral friction and ψ the horizontal stream function. The equation describes the balance of vorticity from lateral stress, planetary vorticity and wind stress curl. Solving for ψ the horizontal mass transport is described by

$$T_x = \frac{\partial \psi}{\partial y} \quad ; \quad T_y = -\frac{\partial \psi}{\partial x} \tag{2.28}$$

The mass transport is subdivided into

$$T_x = T_{xE} + T_{xg} \quad ; \quad T_y = T_{yE} + T_{yg} \tag{2.29}$$

where the first term on the right hand side is the wind-driven Ekman transport and the second term the geostrophic mass transport, induced by the distribution of pressure. Where the density of the fluid just depends on pressure, isobaric and isopycnal (layer of specific densitiy) surfaces are parallel to each other. The transport variations are determined from pressure differences between two points (a, b) and f/H determines where the current flows (Hughes *et al.*, 1999)

$$T = \int_a^b \int_{-H}^0 u dz ds = \int_a^b H u_g ds + T_{Ek} \tag{2.30}$$

where u_g is the geostrophic velocity perpendicular to the section (a, b) and T_{Ek} is the transport in the Ekman layer. By assuming geostrophy T_{Ek} will not be taken into account due to the non-geostrophy of the flow in the Ekman layer. The transport T is

$$T = T_g = \int_a^b \frac{H}{f\rho} \frac{\partial p}{\partial s} ds \tag{2.31}$$

If both points a and b lie on the same contour f/H then T is estimated by the pressure difference

$$T = \frac{H}{f\rho}(p_b - p_a) \tag{2.32}$$

2.2.3 Vorticity

All objects rotating at the Earth's surface are affected by the planetary vorticity. It is twice as large as the local rate of the Earth rotation and is the Coriolis parameter f

$$f = 2\Omega \sin \phi \tag{2.33}$$

Mass in the oceans rotate relative to the Earth's surface in their own reference frame. This is described by the relative vorticity

$$\zeta = \mathrm{curl}_z \vec{V} = \frac{\partial v}{\partial x} + \frac{\partial u}{\partial y} \tag{2.34}$$

where $\vec{V}$ is the horizontal velocity. For most parts of the ocean, ζ is much smaller than f. The sum of planetary and relative vorticity is the absolute vorticity. By cross-differentiating the horizontal components of Eq. (2.22) for a frictionless flow, subtracting both equations to eliminate the pressure term, a differential equation for the absolute vorticity is given as

$$\frac{d}{dt}(\zeta + f) + (\zeta + f)\nabla \vec{V}_H = 0 \tag{2.35}$$

where also the "Principle of Conservation of Absolute Vorticity" is described (Stewart, 2008). This will be important for the description of the potential vorticity. If a column of fluid will expand or contract, then the rotation rate of the column will also change due to the conservation of the angular momentum in the column. This is induced by a change of the relative vorticity. When considering a barotropic and geostrophic flow in the ocean with a depth H and the flow exists between the surface and ocean bottom, then conservation of volume for the flow is stated as

$$\frac{1}{H}\frac{dH}{dt} + \left(\frac{\partial u}{\partial x} + \frac{\partial v}{\partial y}\right) = 0 \tag{2.36}$$

Substituting this relation into Eq. (2.35) and eliminating the horizontal divergence term, then

$$\frac{d}{dt}\left(\frac{\zeta + f}{H}\right) = 0 \tag{2.37}$$

where the term in braces is the potential vorticity Π. The conservation of potential vorticity leads to different effects in the ocean, because changes in depth, latitude and relative vorticity are coupled to each other.
An effect when $f \gg \zeta$ is the zonal distribution of currents along constant contours of f/H. Barotropic flows are diverted by sub-sea mountains or troughs. This is also called "topographic steering".

A good example for the impact of vorticity changes is seen in the path of the Antarctic Circumpolar Current which is mainly driven by surface winds but modified regionally by topographic steering and stratification (see Ch. 7.1).

2.2.4 Taylor-Proudman theorem

Geostrophic flows of fluids with homogeneous density, which are rotating, slowly-varying and frictionless, are two-dimensional and do not vary in the direction of the rotation vector. This is stated by the Taylor-Proudman theorem (Stewart, 2008). Taking the curl of the horizontal component of eq. (2.22), neglecting friction and assuming a barotropic flow (so $\rho = \rho(p)$) then the Taylor-Proudman theorem reads as

$$(\Omega \cdot \nabla)\vec{v} = 0 \qquad \text{or} \qquad \frac{\partial \vec{v}}{\partial z} = 0 \tag{2.38}$$

Building up so called "Taylor columns", a steady-state motion exists and is not allowed to vary along the rotation axis of the Earth. Due to the incompressibility of the column (the height h must be constant), just a zonal motion along a latitude-circle is possible. This allows for the

development of large nearly zonal currents, especially in regions where continental boundaries are absent as, e.g. in the ACC on the southern hemisphere.

2.2.5 Variability of ocean bottom pressure and sea level

The fundamentals of temporal variability in the ocean have been summarized by Gill & Niiler (1973) by assuming an ocean with geostrophic and Sverdrup dynamics in the interior ocean and Ekman dynamics near the surface. Ocean bottom pressure p_b has been defined as the sum of atmospheric pressure p_a and the weight per unit area of the water column,

$$p_b = p_a + g \int_{-H}^{0} \rho dz + g\rho_0 \eta \tag{2.39}$$

where η is the sea level height at the ocean surface. Changes in Eq. (2.39) are due to density changes, changes in total sea level $\Delta\eta$ and atmospheric pressure p_a. Variations of barometrically corrected sea level $(\Delta\eta - \Delta\eta_a)$ are due to fluctuations in wind stress and variations of the surface density and mass flux. Ponte (1999) expressed seasonal changes in p_b according to Gill & Niiler (1973) as

$$\frac{\partial(H \csc\phi)}{\partial\phi}\frac{\partial p_b}{\partial\lambda} - \frac{\partial(H \csc\phi)}{\partial\lambda}\frac{\partial p_b}{\partial\phi} = \csc\phi \cot\phi \frac{\partial P}{\partial\lambda} - 2\Omega a^2 \rho_0 \cos\phi w_E \tag{2.40}$$

with the potential energy P

$$P = \int_{H}^{0} g\rho z dz \tag{2.41}$$

and the Ekman pumping velocity w_e. For barotropic processes the potential energy P is set to zero and variations are only due to wind stress curl variations (2nd term on right hand side of eq. (2.40)). Elsewhere, baroclinic processes are needed to take into account due to density stratification of the water column. Seasonal OBP fields (winter, spring, summer, fall) show large scale divergence and convergence of mass due to the varying flow field (Ponte, 1999), where only small divergence processes in the horizontal oceanic motions are involved leading to changes in ocean bottom pressure. For a better understanding of these processes, Ponte (1999) rewrote Eq. (2.40) to

$$\frac{p_{b_t}}{g} + J\left(p_b, H/f\right) - \frac{f_y}{f^2}P_x = \left(\frac{\tau^y}{f}\right)_x - \left(\frac{\tau^x}{f}\right)_y - \rho_0 Q + O\left[\frac{w}{f}\right] \text{terms} \tag{2.42}$$

The local mass divergence $\left(\frac{p_{b_t}}{g}\right)$ is, with the divergence of the geostrophic transport $\left(J\left(p_b, H/f\right) - \frac{f_y}{f^2}P_x\right)$, balanced by the divergence of the Ekman transport $\left(\left(\frac{\tau^y}{f}\right)_x - \left(\frac{\tau^x}{f}\right)_y\right)$,

the mass flux of fresh water at the surface ($\rho_0 Q$) and the ageostrophic effects relative to the geostrophic term ($O[w/f]$). The mass flux term is almost negligible to the Ekman terms.

Chapter 3

The Gravity Recovery and Climate Experiment - GRACE

The Gravity Recovery and Climate Experiment (GRACE) satellite mission has been launched in March 2002 and is an innovative mission to monitor the Earth's gravity field with an unprecedented accuracy (Tapley, 2004). The twin-satellites were launched in an orbital height of around 500 km, with a distance of around 220km and an inclination of 89.5° and planned for a mission lifetime of five years. Currently, after 12 years of operation, the orbital height has been reduced (∼410 km) and the satellites will continue monitoring hopefully until 2018 (Tapley *et al.*, 2014), but persistent problems with the batteries might cause a sudden end of the mission at any time.

Recording of gravity changes with GRACE are based on the low-low satellite-to-satellite tracking principle. The relative velocity between both satellites is determined by a dual-frequency phase measurement of the K-band microwave ranging system with a nominal accuracy of 1μm/s. The phase measurements of both satellites are combined to ionosphere-free one-way solutions. To estimate the position of the satellites in a geocentric reference system, each satellite carries a GPS receiver wich also enables precise time-tagging of the measurements. Attitude sensors (star cameras) provide precise estimates of the inertial orientations of the satellites. Accelerometers deliver information of the surface force accelerations on the spacecrafts to quantify non-gravitational forces.

3.1 Processing centers and data

GRACE data are calculated by the Science Data System (SDS). The three main SDS centers, the Centre of Space Research at the University of Texas (CSR), the German Research Centre for Geosciences in Potsdam (GFZ) and the Jet Propulsion Laboratory in Pasadena (JPL) provide monthly and long-term mean Level-2 sets of spherical harmonic coefficients of the global gravity potential for public use in the scientific community.
The recovery of the gravity potential utilizes the dynamical approach. There, the satellite's equations of motion in an inertial frame are based on the Newtonian formulation. The non-linear problem is solved for orbital, instrumental, geometric, kinematic and dynamical parameters by minimizing the observational residuals according to the Gaussian least-square principle.
During orbit integration, contributions from the static gravity field and known time-variable components are already removed by background models (Dahle *et al.*, 2012), including

- third-body acceleration on the satellites due to gravitational pull from Earth, Sun, Moon and other planets;
- luni-solar tides of the Solid Earth, oceans and the atmosphere;
- non-tidal mass redistributions in atmosphere and ocean (Flechtner & Dobslaw, 2013); and
- pole-tide effects on the Solid Earth and oceans caused by Earth rotation variations.

The GRACE data are stored in databases of the ISDC[1] and PO.DAAC[2] and consist of both Level-1B and Level-2 data.
The Level-1B data products are the processed raw-data from both satellites. In the Raw Data Centre (RDC) at DLR in Neustrelitz the data are collected and stored in the rolling archive of the RDC. Then the data are converted from binary encoded measurements to engineering units, they were correctly time-taged and the sample rate of the high rate data is reduced.
The Level-2 data products are the monthly mean spherical harmonic coefficients of the Earth's gravity field (GSM) and corresponding monthly means of the Level-1B 6-hourly non-tidal atmospheric and oceanic de-aliasing models (AOD1B). There are four Level-2 AOD1B components:

GAA: non-tidal contributions of the atmosphere

GAB: non-tidal contributions of the ocean

GAC: sum of GAA and GAB

[1] Information System and Data Center, http://isdc.gfz-potsdam.de
[2] Physical Oceanography Distributed Active Archive Center, http://grace.jpl.nasa.gov/

GAD: sum of GAA and GAB but the continents were set to zero, and surface pressure instead of the 3D integration of atmospheric masses is applied over the oceans.

Whereas the GSM coefficients are determined according to the Centre of Mass (CM) of the Earth and therefore coefficients of degree 0 and 1 are set to zero and one respectively, these are included in the AOD1B-products which are given in the Centre of Figure (CF) frame. The monthly GRACE coefficients are available up to d/o = 90 for JPL and GFZ and to d/o = 60 for CSR. The current release 05 consists of 137 monthly data (04/2002-06/2014) where 12 months are missing due to a 4-day repeat orbit (06/2002, 07/2007, 01/2003, 07/2003) and for later solutions due to the battery status of the satellites and according to switch-offs of the K-band device (01/2011, 06/2011, 05/2012, 10/2012, 03/2012, 08/2013, 09/2013, 02/2014). Besides the conventional monthly spherical harmonic coefficients, datasets with other temporal and spatial resolution are available. GFZ also distributes weekly sampled coefficients up to d/o = 30 which are aligned to the GPS weeks and processed with the same models as the monthly solutions. The french Centre National d'Etudes Spatiales distributes 10-day sampled coefficients up to d/o = 50 (Bruinsma *et al.*, 2010) and the University of Bonn provides even 1-day sampled coefficients up to d/o = 40. A detailed description of these alternative products are given in Chapter 7.1.
The Astronomical Institute of the University of Bern developed a processing strategy to determine monthly gravity fields with the Celestial Mechanics Approach (Beutler *et al.*, 2010). The coefficients are computed up to degree 60 and order 45 due to large noise in the higher order coefficients (Meyer *et al.*, 2012).
Mass concentration (mascons) solutions are processed with a temporal and spatial resolution of 10 days and 4°×4° (Rowlands *et al.*, 2010). The mascon solution represents the surface mass distribution as a uniform layer in a regularly shaped cell as spatial and temporal step functions. The mascon parameter describes the change in the gravity potential caused by a small layer of mass over a region. They are given as differential potential coefficients which have to be added to the a priori mean field. The differential potential coefficients are determined by integration over the restricted region.

3.2 Postprocessing methods

3.2.1 Glacial Isostatic Adjustment

During the Last Glacial Maximum the Earth was covered with large ice shields on the northern and southern hemisphere. Today, these ice shields have been collapsed to the two big

ice shields of Greenland and Antarctica, parts of Alaska and other glacier regions, e.g. Himalayan. The growing and melting of such huge ice shields have an impact on the underlying Solid Earth, especially the lithosphere and the upper mantle.
Due to the surface load of the ice masses, the lithosphere which behaves like an elastic body, is deformed and . The underlying mantle partly compensates the deformation by viscous flow. With the retreat of the ice masses, the surface load disappeared and the lithosphere reacts to the new loading situation by rebounding. On long timescales (centuries), mantle material also flows back beneath the lithosphere to drive the resulting isostatic response of the lithosphere. This response is still in place and is observable by measurements (e.g. GPS permanent stations). The surface upload results in variations of the gravity potential and is therefore also included in observations from GRACE. Even today's melting of ice caps and glaciers affects the process of the Glacial Isostatic Adjustment (GIA). The GIA signal is included in the secular gravity signal. Observations by GRACE are not able to separate processes on the surface (due to mass redistributions) and the Earth's interior (solid Earth processes). Therefore the data must be corrected for GIA trends, when surface mass redistribution processes are analyzed. For the corrections, output from GIA models are necessary.
Geophysical studies from seismic tomography lead to a better understanding of the deep Earth and were providing the basis for the Preliminary Reference Earth Model (PREM, Dziewonski & Anderson (1981)) and the current GIA models. PREM is used to determine the Earth's radial elastic and density structure to model the behaviour of the lithosphere due to surface loads. The viscosity values for the mantle were determined by inversion of observations of independent geophysical studies. Global GIA models use ice histories of the last glacial cycle. The accuracy of these models depends on the accuracy of the ice model. The usually used models are ICE-3G (Tushingham & Peltier, 1991) and ICE-5G (Peltier, 2004). There are also regional models for the northern hemisphere (Zweck & Huybrechts, 2005) or Greenland and Antarctica (Huybrechts, 2002; Ivins & James, 2005).
For all studies in this work, the GIA model of Paulson *et al.* (2007) has been used. It is based on the model of Zhong *et al.* (2003), which was designed to study purely viscous mantle convection problems, and has been updated to account for the motion of the Earth's centre of mass and the influence of the polar wander. It includes the ICE-3G loading history and a 3D-viscosity structure has been implemented.

3.2.2 Low degree Spherical Harmonics

The lower spherical harmonics include the coefficients of degree 0 and 1 and also ΔC_{20}, which have a geophysical meaning.
The $l = 0$ term is proportional to the mass of the whole Earth including the surface (atmosphere, ocean, hydrology) and the Solid Earth contribution. Due to the mass conservation, there will be no change in time for ΔC_{00}. When excluding one component, e.g. ocean, there will be temporal changes in the total mass and the $l = 0$ term will not vanish. But there will not be any contribution to the $l = 0$ term of the Solid Earth response. There is neither a contribution to the displacement nor the gravitational potential displacement and the Load Love Numbers of k_0 and h_0 are zero.
The $l = 1$ terms are related to the position of the Earth's Center of Mass (CM) relative to the centre of the chosen coordinate system (Wahr *et al.*, 1998). The GRACE mission is referenced to the CM and therefore, ΔC_{10}, ΔC_{11} and ΔS_{11} are zero. Again, when separating an individual mass component, the terms do not vanish but there will not be any response to the change in the CM of the Solid Earth. This leads to a Load Love Number of $k_1 = -1$. If a different reference system is chosen, then the $l = 1$ terms cannot be neglected and are different from zero. A detailed description of estimating the $l = 1$ terms is given in Chapter 6.1.
The ΔC_{20} coefficient needs special attention when working with GRACE data. It is related to the Earth's dynamic oblateness J_2. Previous studies have shown, that there exist a steady increase in J_2 since 1979 (Cox & Chao, 2002; Dickey *et al.*, 2002) due to GIA processes. The secular signal has been determined accurately from Satellite Laser Ranging observations to 0.116×10^{-10} per year (Cheng *et al.*, 1997).
Due to the orbital geometry of the GRACE mission and the short distance of around 200km between both satellites, ΔC_{20} is not well determined. Comparison studies with SLR-measurements have shown that for RL04 the time series is still affected by the S2-tide signal, which has an aliasing period of 161 days and an amplitude (1.12×10^{-10}) nearly as large as the annual signal (1.43×10^{-10}) of ΔC_{20} (Chen & Wilson, 2008). Whereas the new RL05 data from GFZ have shown good correspondence to SLR-observations (Bonin & Chambers, 2011), but a lately update to RL05a makes it necessary to replace the ΔC_{20} time series by SLR-data again (Dahle, 2014).

3.2.3 Filter and de-striping methods

The GRACE solutions cannot be used up to their full spectral content since correlation noise dominates the higher harmonics. This results from the mission geometry, the sensor

error characteristics, limitations in the dealiasing strategies and the used background models (Kusche, 2007). In the GRACE error budget there are on the one hand random errors increasing as a function of spatial degree (Wahr *et al.*, 2006) and on the other hand systematic errors, which are correlated within a particular spectral order (Swenson & Wahr, 2006). This results in increasingly correlated noise at higher degrees which appear as stripes in the results of the spatial domain. To reduce these artifacts, spatial smoothing operators (or filters) are needed which consist of a kernel with gradually decreasing power. A simple truncation in the lower degrees will however dismiss a large part of the signal and is therefore no option when focussing on regional applications.

The GRACE data centers also provide regularized and constrained solutions. For a few months, the GRACE satellites were in a 61/4 resonance orbit which leads to a lower spatial coverage. The solutions are then constrained to a priori estimates. The normal equations are stabilized by application of a regularization method based on Kaula's power law.

In the most general case, the GRACE solutions, expanded in fully normalized spherical harmonics (Stokes Coefficients), are convolved against a two-point kernel function W:

$$F_W(\theta,\lambda) = \sum_{l=0}^{\infty}\sum_{m=0}^{n} \bar{f}_{lm}^{W}\bar{Y}(\theta,\lambda) \tag{3.1}$$

where $\bar{f}_{lm}^{W}$ are the convolved coefficients with:

$$\bar{f}_{lm}^{W} = \sum_{l'=0}^{\infty}\sum_{m'=0}^{n} \bar{w}_{lm}^{l'm'}\bar{f}_{l'm'} \tag{3.2}$$

In the spectral domain the two point kernel is designed as:

$$\bar{w}_{lm}^{l'm'} = \frac{1}{(4\pi)^2}\int_{\Omega}\int_{\Omega'} W(\theta,\lambda,\theta',\lambda')\bar{Y}_{lm}(\theta,\lambda)\bar{Y}_{l'm'}(\theta',\lambda')d\omega d\omega' \tag{3.3}$$

3.2.3.1 Isotropic filters

If the kernel function only depends on one parameter (i.e. the spherical distance Ψ between two points, degree l of coefficients) then an isotropic filter is constructed.

The spherical harmonic coefficients are reduced to Legendre coefficients of a zonal function w_l:

$$F_W(\theta,\lambda) = \sum_{l=0}^{\infty}\sum_{m=0}^{l} w_l\bar{f}_{lm}\bar{Y}(\theta,\lambda) \tag{3.4}$$

A typically used isotropic filter is the Gaussian Filter. It is based on the normalized Gaussian mean-function which is determined from the Gaussian probability density function. This is

bell shaped with its maximum weight in the center and approximately zero with increasing distance from the center point. The Legendre coefficients are determined from a recursion relation (Jekeli, 1981; Wahr *et al.*, 1998):

$$w_0^d = \frac{1}{2\pi} \tag{3.5}$$

$$w_1^d = \frac{1}{2\pi}\left[\frac{1+e^{-2b}}{1-e^{-2b}} - \frac{1}{b}\right] \tag{3.6}$$

$$w_{l+1}^d = -\frac{2l+1}{b} w_l^d - w_{l-1}^d \tag{3.7}$$

with

$$b = \frac{\ln 2}{1-\cos d/R} \tag{3.8}$$

The parameter d describes the 'half-width'-radius and therefore the degree of smoothing. It is given as the distance from the center where the filter kernel has decreased to the half of its power. For GRACE processing, d has usually been chosen around 200 km to 400 km for continental and 500 km to 1000 km for oceanographic applications.

3.2.3.2 Non-isotropic filters

If more parameters are taken into account (i.e. degree l and order m), then a non-isotropic filter is constructed. The filter kernel is symmetric to the diagonal or non-symmetric. An example for this case is the DDK-filter developed by Kusche (2007). It consists of a fully populated filter matrix.

The filter kernel is based on the regularization of a characteristic normal equation system which involves a priori information of the signal variance and the observation system. Estimating a realistically signal covariance matrix, requires the accumulation of a large number of geophysical models and their error budgets. The normal equation matrix of the GRACE coefficients is needed for set up the covariance matrix of the observations which is available only on request. Due to these facts, approximations for the a priori signal covariance function M and the GRACE error covariance matrix N are used to define the filter function:

$$W(\alpha) = L_\alpha N = (N + \alpha M)^{-1} N \tag{3.9}$$

The filter kernel is defined in the spectral domain as:

$$w_{lm}^{l'm'} = \sum_{l=0}^{\infty} \sum_{m=0}^{l} L_{lm}^{l''m''(\alpha)} N_{l''m''}^{l'm'} \tag{3.10}$$

The parameter α defines the damping parameter and therefore the smoothing. Kusche *et al.* (2009) have shown, that the kernel $W(\alpha)$ can be replaced by a block-diagonal version of the matrix to speed up the filtering process. This version has been used for the anisotropic filtering of the GRACE coefficients in this work.

3.2.4 Leakage reduction of continental signals

When focussing on oceanographic applications of GRACE data problems arise near the coast lines of the continents. The continental signals from hydrology and cryosphere are larger than the bottom pressure signal off the coast. Due to filtering of the GRACE data to reduce noise and striping artifacts the continental signal is attenuated and will leak into the ocean where it is then interpreted as an oceanic signal. Therefore a reduction of these leakage effect is necessary.
Chambers (2009) proposed to leave out a region of 300 km around the coast to avoid the leakage signal. When focussing on global scales or large basin averages, like global ocean mass variations, this is generally feasible. But when focussing on regional studies and validations with coastal (tide gauges) or near costal measurements (ocean bottom pressure recorders; OBPR) a substantial fraction of the area of interest is left out.
A typically followed strategy proposed by Wahr *et al.* (1998) is to first solve for the continental mass distribution, remove these effects from the original GRACE data and use the residual coefficients to solve for the ocean component. Therefore a region function is introduced with:

$$C(\theta, \lambda) = \begin{cases} 1 & \text{over land} \\ 0 & \text{over ocean} \end{cases} \tag{3.11}$$

Additionally the continental signal is smoothed with a Gaussian filter with $d = 300$ km. The residual coefficients represent the oceanic signal and are given by:

$$\begin{Bmatrix} \Delta C_{lm}^{ocn} \\ \Delta S_{lm}^{ocn} \end{Bmatrix} = \begin{Bmatrix} \Delta C_{lm} - \Delta C_{lm}^{cont} \\ \Delta S_{lm} - \Delta S_{lm}^{cont} \end{Bmatrix} \tag{3.12}$$

3.2.5 Pattern filtering of ocean bottom pressure fields

Before space geodetic measurements were available mostly pointwise observations were made in oceanography. Today, these measurements are still continued and available through different data centers (e.g. Permanent Service for Mean Sea Level, NOAA National Geophysical Data Center or British Oceanographic Data Center). A direct validation of these in situ data with GRACE results is inadvisable because GRACE solutions represent data with scales of several hundreds of kilometers.

A model study of Böning *et al.* (2008) has shown that the ocean bottom pressure (OBP) anomalies are coherent over large areas and show a complex geometry which is strongly correlated to the bottom topography. This coherency pattern can be used for weighted filtering of the GRACE data to improve the validation with pointwise observations.

Therefore, in the first step, the coherency pattern are determined from OBP model time series. The cross-correlations $r(\vec{x}, \vec{x}_0)$ were computed between a fixed position $\vec{x}_0$, representing the OBP station, and all points $\vec{x}$ of the model domain within a radius of 20°. The pattern is used in the area were the cross-correlation is higher than 0.7:

$$r^*(\vec{x}, \vec{x}_0) = \begin{cases} r(\vec{x}, \vec{x}_0) & \text{for } r(\vec{x}, \vec{x}_0) \geq 0.7 \\ 0 & \text{for } r(\vec{x}, \vec{x}_0) < 0.7 \end{cases} \tag{3.13}$$

To achieve a smooth transition at the boundaries where the cross-correlation is still 0.7 a monotonically decreasing cut-off function is set at a distance of 18° with:

$$\zeta(\vec{x}, \vec{x}_0) = \frac{1 - \tanh\left(\frac{\Delta(\vec{x}, \vec{x}_0) - 18^\circ}{2^\circ}\right)}{2} \tag{3.14}$$

where Δ is the distance between the points $\vec{x}$ and $\vec{x}_0$. Finally, the filtered GRACE solution at the position $\vec{x}_0$ is given by:

$$p_G^*(\vec{x}_0) = \frac{\int\limits_C p_G \cdot r^*(\vec{x}, \vec{x}_0) \cdot \zeta(\vec{x}, \vec{x}_0) dA}{\int\limits_C r^*(\vec{x}, \vec{x}_0) \cdot \zeta(\vec{x}, \vec{x}_0) dA} \tag{3.15}$$

The integral is computed over a circle of 20° radius around $\vec{x}_0$.

Böning *et al.* (2008) achieved with these filtering strategy higher correlations with time series of OBP recorders globally distributed. Also, the characteristics of the OBP time series could be better reproduced compared to the typically applied Gaussian filter. Additionally, the RMS of the pattern-filtered grid reveals more small scale features especially for the western boundary currents like the Kuroshio, the Gulf Stream or the Agulhas Return Current. Also

the reduced variabilities around the coast lines show the ability of the pattern-filter to reduce leakage effects from continental signals.

Chapter 4

Oceanic in situ observations of OBP and sea level

Oceanographic in situ measurements are important for the validation and error assessment of space based data. Therefore, quality checked data of sea level and ocean bottom pressure observations are required.
The Permanent Service for Mean Sea Level (PSMSL) holds long term data of tide gauges and ocean bottom pressure recorders. It collects the available data, is doing analyses and interpretation of the sea level observations which are published giving information about the long term change in sea level variations. PSMSL receives most of its data from the Global Sea Level Observing System (GLOSS) network. It consists of 289 sea level stations (Fig. 4.1). Ocean bottom pressure data were collected from national institutions, like the British Oceanographic Data Centre (BODC). Alternatively, ocean bottom pressure data can be procured from the National Data Buoy Centre (NDBC) of the National Oceanic and Atmospheric Administration (NOAA).

In this chapter, information about tide gauges and ocean bottom pressure recorders will be given. A short description of the data processing concerning tides and time series analysis follows. The final processed in situ data will be subsequently used for validation in the chapters 5 and 7.1.

4.1 Tide gauges

Monitoring of water level heights of rivers, lakes and at the sea has been made historically by tide poles and staffs. Already in the ancient Egyptian culture the water level of the Nile

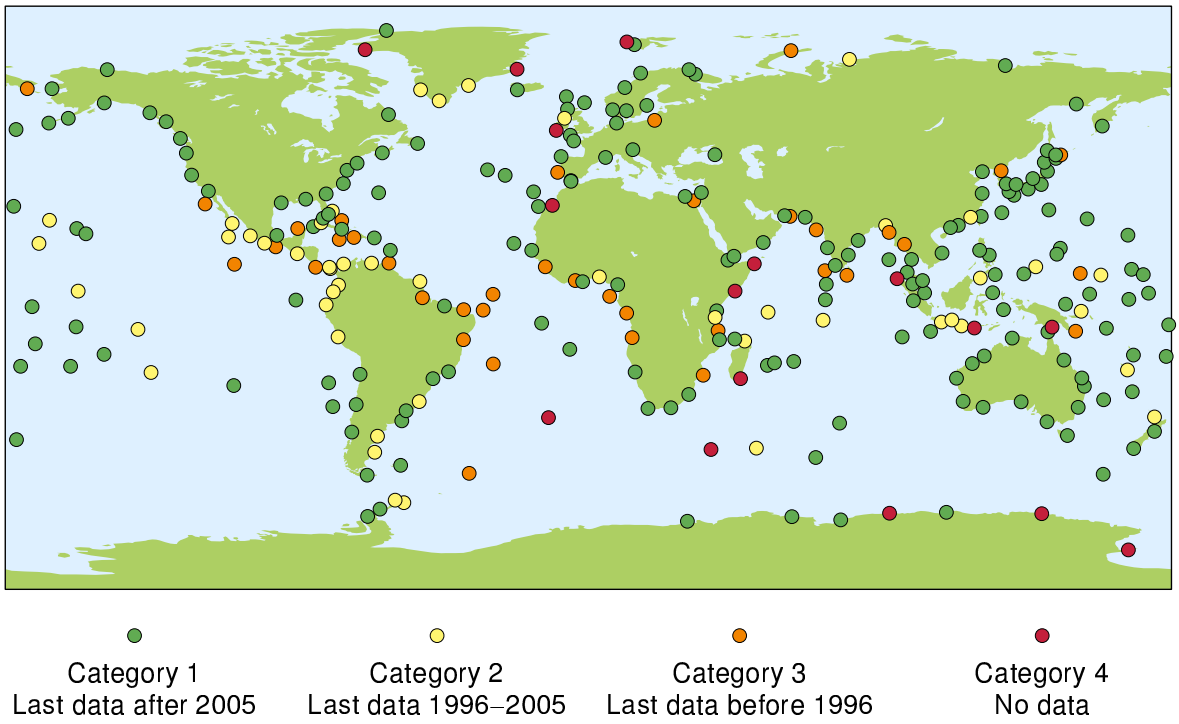

Figure 4.1: Stations and current status of the GLOSS network for December 2010 (http://www.gloss-sealevel.org)

has been observed by this method to predict the flooding time, which was important for the agriculture and the economic wealth of the civilization. This primitive observation method is still in use as co-located monitoring system for modern-day tide gauge stations for the cross-checking of the sea level data.
Modern tide gauge stations consist of mechanical floats and stilling-wells connected to a potentiometer which transforms the mechanical input to electronic readouts, or of fully electronic measurement systems like pressure, acoustic and radar gauges.
All sea level observations have been made relative to a nearby geodetic benchmark (Fig 4.2). Therefore, a precise datum control is necessary to guarantee a long-term stability of the tide gauge station. Continued surveying of the geodetic benchmark reveals vertically movements of the stations due to ongoing GIA processes, tectonic uplifts or crustal subsidence.
Additionally, meteorological factors, like barometric pressure, temperature and wind speed, were also monitored for correcting the sea level data.

The tide gauge stations used in Chapter 7.1 are equipped with pressure gauges. Only at the station Vernadsky/Faraday a mechanical float and stilling well gauge is installed with an analog paper chart recorder. Thereby, a long-time monitoring of this station of around 50 years (1959-2009) is available. The temporal resolution of the tide gauge stations varies between

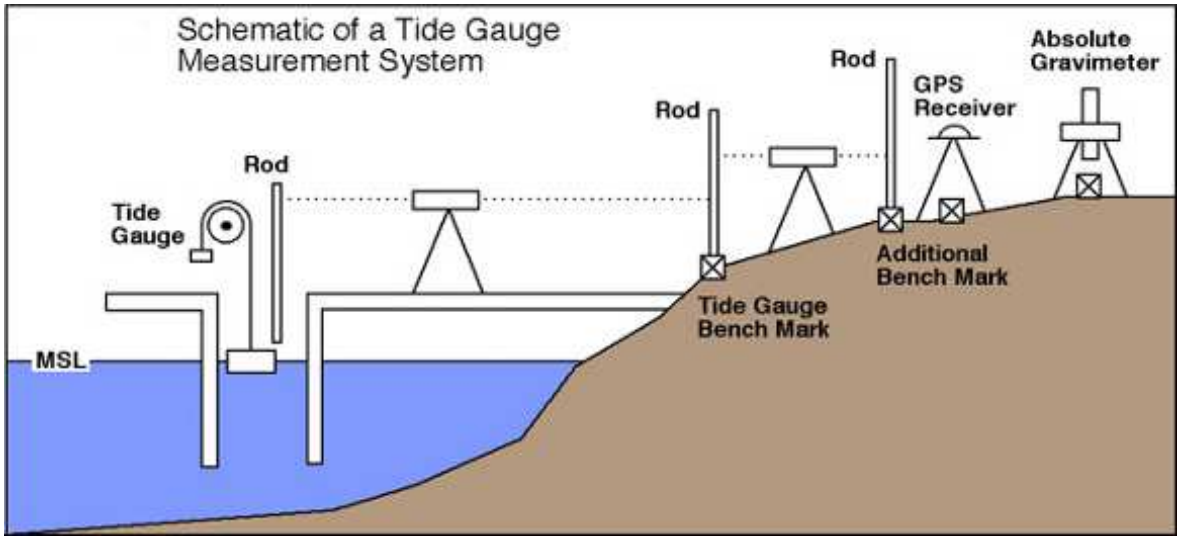

Figure 4.2: Schematic of a tide gauge measurement system (http://sealevel.colorado.edu/content/tide-gauge-sea-level)

10 minutes (pressure recorders) and 1 hour (chart recorder) samples. Water temperature and atmospheric pressure are measured locally at the pressure gauges for internal calibration.

4.2 Ocean Bottom Pressure Recorders

Ocean Bottom Pressure Recorders (OBPR) provide valuable data for researches in oceanography and climate disciplines. They measure the absolute pressure of the water column and the above atmosphere. Variations in the time series are induced by mass redistributions in the ocean and atmosphere. The point-wise observations deliver an independent in situ data set for validating space- or model-based time series. Due to the sparse temporal and spatial resolution of OBPR-data (see Fig. A.1), only large-scale features (e.g. tides) are worth for investigation with global data sets which consist of long-term (trend to inter-annual) but also short-term (seasonal to sub-monthly) signals. An example will be given in Chapter 5.
Present-day OBPRs are equipped with Paroscientific Digiquartz sensors where the resonance frequency of a piezoelectric crystal deformed by the ambient pressure is measured. The sensor is located in Bellows or Bourdon tubes and deployed at the sea floor. Due to the temperature dependence of the oscillator, additional temperature measurements are made inside of the cavity. Both, pressure and temperature are recorded at 15 second intervals while achieving a pressure sensor accuracy of 0.1 hPa. Therefore, short-term pressure anomalies are detectable.

4.3 Processing of in situ observations

An important step when using in situ observations from tide gauges and OBP recorders is the quality control of the data sets. Whereas tide gauges are mainly affected by the tides, OBPRs show also signs of sensor drifts (Fig. 4.3a). Especially during the deployment and the first months, the drift signal is largest and reduce to slower drift during the monitoring period.
In the following sections, different options for tide reduction and further time series analysis handling drift and temporal resolution are discussed.

4.3.1 Ocean tides

Due to gravitational forces of the Sun and the Moon, temporal variations in the Earth's gravity field are induced which are known as tides. For a solid Earth the tidal potential is described by Newtons law of gravitation and law of motion (Torge, 1991). In an inertial system a point mass M_A will induce a potential of

$$V_A = \frac{GM_A}{r_A} \tag{4.1}$$

where G is the gravitational constant and r_A the distance between the Moon/Sun and the point mass. The tidal potential is referenced to the geocenter and is scaled to zero at the Earth's centre of mass. Any point at the Earths surface will experience a tidal potential of

$$V_A(X_P) = \frac{GM_A}{r_A} = \frac{GM_A}{d} \sum_{l=2}^{\infty} \left(\frac{R}{d}\right)^l P_l \cos\psi \tag{4.2}$$

where R is the Earth Radius and d the distance between the mass centre of the Earth and the Moon/Sun. The terms of $l = 0, 1$ are omitted. The tidal potential is dominated by the term of $l = 2$. Terms of higher degrees are smaller by a factor of $(R/d)^l \simeq 0.016^l$. Changing to an earth-fixed coordinate system, a system that rotates with the Earth, the spherical distance to the Moon or Sun is described as

$$\cos\psi = \sin\bar{\varphi}\sin\delta_A + \cos\bar{\varphi}\cos\delta_A\cos t_A \tag{4.3}$$

where $\bar{\varphi}$ is the geocentric latitude of the surface point, δ_A the declination and t_A the hour angle of the Moon or Sun. The hour angle depends on the geographical longitude of the surface point (λ) and the right ascension of the Moon (α_M) or the Sun (α_S)

$$t_A = \lambda + \mathrm{GAST} - \alpha_A \tag{4.4}$$

where GAST is the Greenwich Apparent Siderial Time. Finally, the tidal potential is described by Laplace's tidal equation

$$V_A = \frac{3}{4} G M_A \frac{r^2}{R^2} \Bigg(\left(\frac{1}{3} - \sin^2 \bar{\varphi} \right) (1 - 3 \sin^2 \delta_A) + \sin 2\bar{\varphi} \sin 2\delta_A \cos t_A + \cos^2 \bar{\varphi} \cos^2 \delta_A \cos 2t_A \Bigg) \tag{4.5}$$

The first term is independent of the Earth's rotation and describes the long periodic tides of Moon and Sun. The second and third term describe the diurnal and semidiurnal tides.

4.3.2 Harmonic analysis

The tidal potential can also be modeled as the sum of a finite set of sinusoids at specific frequencies. These frequencies are given as a combination of sums and differences of integer multiples of the 6 fundamental frequencies from planetary motions (Godin, 1972). Each partial tide and the frequency is identified by its Doodson number.
The traditional approach for describing the tidal time series $x(t)$ is given as

$$x(t) = b_0 + b_1 t + \sum_{k=1}^{N} (A_k \cos \sigma_k t + B_k \sin \sigma_k t) \tag{4.6}$$

where

N	number of constituents
σ_k	frequency constituents given by Doodson number
b_0, b_1	mean and trend of the time series
A_k, B_k	relative amplitudes of the constituents

By solving a least squares fit for the unknown relative amplitude and phase of the tidal frequencies, the tide signal $x(t)$ is modeled.
To solve for all listed tidal frequencies a time series length of 18.6 years is needed to reduce the effect of the Moons' ascending node. Mostly, observation periods are one year and shorter.

This results in an amplitude and phase response of the sinusoids with similar frequencies. Displaying the estimated tides in a periodogram shows nodal modulations (smaller peaks) near the main peak of the tide. For really short time series even dissimilar constituents are unresolvable which is a typical problem of the classical adjustment method. A careful handling of the modeled tidal signal is necessary because also non-tidal signals are co-determined by this method and will interfere with the results.

4.3.3 Doodson filter

The Doodson filter is a low pass filter designed to reduce the tidal energy of diurnal and higher frequencies (IOC, 1985). The filter is symmetric about the central value for $t = 0$ and reduce the hourly time series to a daily resolution (Fig. 4.3c). The filter is defined as

$$F(d) = [2, 1, 1, 2, 0, 1, 1, 0, 2, 0, 1, 1, 0, 1, 0, 0, 1, 0, 1] \qquad 1 \leq d \leq 19 \tag{4.7}$$

where d is the index of the filter kernel. The filtered time series $x(t)$ is given as

$$x(t) = \frac{1}{30} \sum_{d=-19}^{19} F(d) \cdot X(t+d) \qquad d \neq 0 \text{and} F(-d) = F(d) \tag{4.8}$$

The filtered data are referred to 12:00 noon.

4.3.4 Drift correction

Time series of OBPR typically show nonlinear drift in the first few days after the deployment. This is due to the pressure sensors which have to achieve a temporal equilibrium with the water at the ocean bottom. Also the recorder subsides. Therefore, the first 24 hours of data are not used for time series analysis. Afterwards, the drift rate decreases and is modeled by a logarithmic or exponential power lay (Watts & Kontoyiannis, 1990). By calculating least-square-fits of the three approaches, the drift is determined and reduced (Fig. 4.3d and e). Watts & Kontoyiannis (1990) studied 17 OBPR in the Golf stream region focussing on drift behavior and found out that the linear-exponential drift curve show smaller RMS-values to the residual time series than the power-law or logarithmic approach. Therefore, the whole data set provided by Macrander *et al.* (2010) is drift corrected by the linear-exponential approach with

$$P_{drift} = P_1[1 - \exp P_2 t] + P_3 + P_4 t \tag{4.9}$$

For solving the nonlinear equation system, routines like the Levenberg-Marquardt algorithm (Fletcher, 1971) are used.
Due to co-estimation of the linear term in the reduction strategy, reliable information about secular changes are not available from OBPR data sets.

4.3.5 Butterworth filter

The Butterworth filter is designed as an analog filter where the frequency response is as flat as possible in the passband (Butterworth, 1930). It is based on a low pass filter design where the cut-off frequency is normalized to 1 radiant per second. The frequency response is maximally flat in the passband. This means, there are no ripples like in other filter designs. The response fades out to approximately 0 in the stop band.
The prototype for the gain function is based on the low pass filter as

$$G(\omega) = \sqrt{\frac{1}{1+\omega^{2n}}} \tag{4.10}$$

where ω is the angular frequency and n the number of poles. The transfer function $H(\omega)$ is designed as

$$G^2(\omega) = \mid H(j\omega) \mid^2 = \frac{G_0^2}{1+\left(\frac{\omega}{\omega_c}\right)^{2n}} \tag{4.11}$$

where ω_c is the cut-off frequency, G_0 the gain at zero frequency and n-poles give the order of the filter. The poles are equally spaced points on a circle with the radius ω_c symmetric to the imaginary axis. the transfer function contains only the poles on the negative real-halfplane of the circle. The Butterworth filter can be adapted to provide high-pass, band-pass and band-stop functionality (see Fig. 4.4).

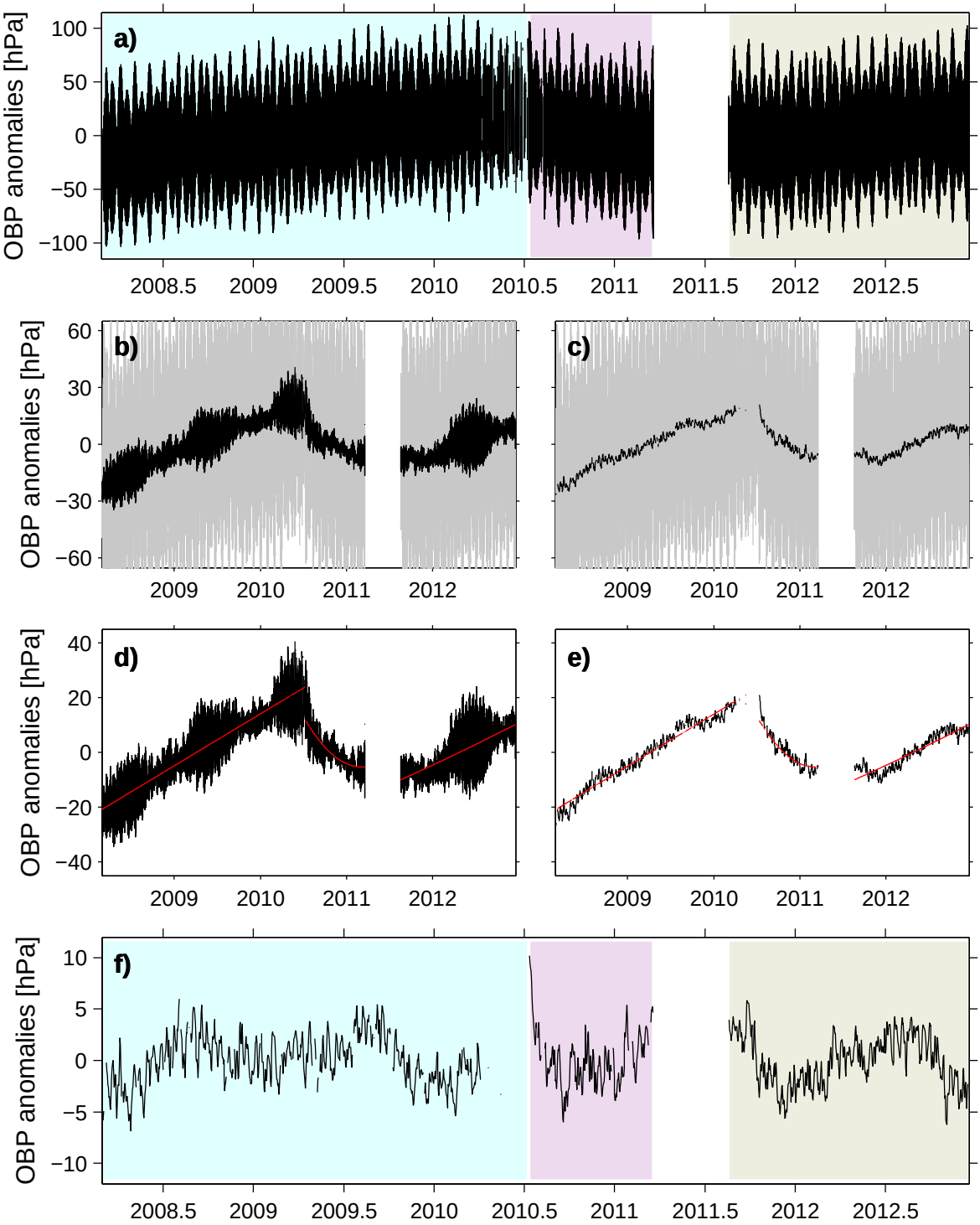

Figure 4.3: Ocean bottom pressure variations for a station in the tropical Pacific and the processing steps: a) the raw time series, consisting of three deployments (indicated with different colors); tide reduction by (b) harmonic analysis and c) Doodson filter, (d) and (e) estimated drift signal for each deployment; f) finally detided and drift reduced time series

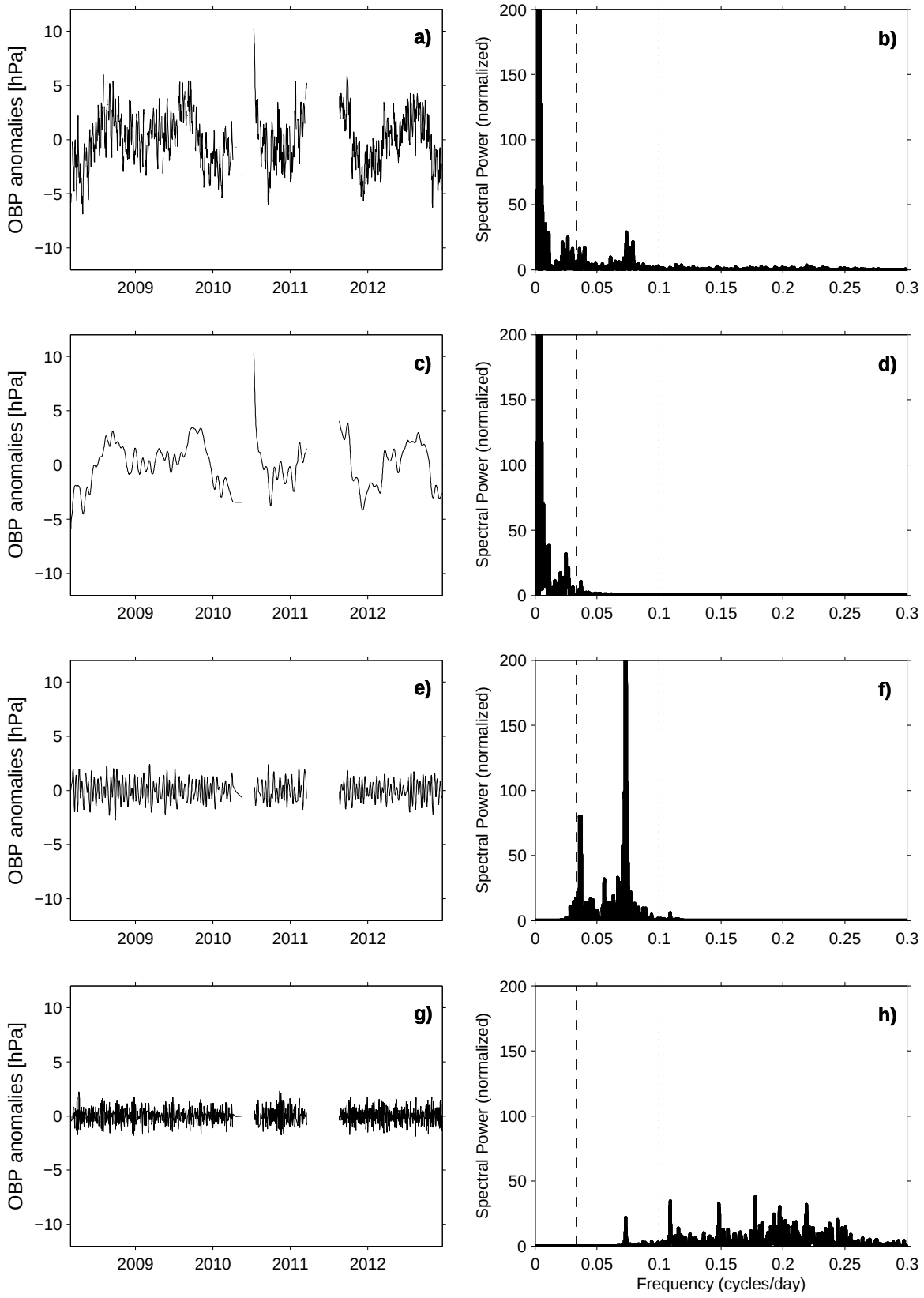

Figure 4.4: OBP time series and associated spectrum of a)/b) whole signal, c)/d) 30 days low pass, e)/f) 10-30 days band pass and g)/h) 10 days high pass Butterworth filter. Frequency: dashed line = 30 days, dotted line = 10 days

Chapter 5

Model data for GRACE applications

Geophysical models aim to represent the main phenomena and known physical processes of the different Earth systems, e.g. atmosphere, ocean or hydrosphere. The implementation of model setups is always a two-way process between determining physical processes from observation data and understanding the signal content of observation data for its introduction in geophysical models. Most space-based geodetic observation methods depend on model data. They are used for different purposes, e.g. correcting for non-observed processes (serving as background models) which affect the main signal content of the observation system, data validation and interpretation or building the base for simulation studies of future satellite missions.

In the processing steps of the GRACE data (see Chapter 3) background models are needed to reduce short-term gravitational signals which will lead to aliasing effects in the monthly solutions. Non-tidal variations are reduced by the AOD1B product (Flechtner & Dobslaw, 2013). It is made of atmospheric pressure, temperature and moisture fields from the ECMWF database and ocean bottom pressure grids simulated by the Ocean Model for Circulation and Tides (OMCT, Thomas *et al.*, 2001). Improvements in the GRACE data come along inter alia with further developments in AOD1B. Especially the latest RL05 of the GRACE data and the associated updated OMCT version show large improvements in the ocean regions compared to the previous RL04 solutions (Chambers & Bonin, 2012).

The ability to model more and more small-scale features with better accuracy provides the opportunity to use these models for end-to-end satellite simulation studies. With the foreseeable end of the GRACE mission, new satellite missions are designed to continue the global gravity field monitoring. To assess the feasibility of the new mission designs for detecting

small-scale mass variabilities, geophysical with their error estimates included, summarized in an Earth System Model (ESM), are needed.

5.1 Ocean Model for Circulation and Tides for AOD1B

5.1.1 RL04 OMCT

The Ocean Model for Circulation and Tides (OMCT; Thomas *et al.*, 2001), based on the Hamburg Ocean Primitive Equation Model (HOPE) (Wolff *et al.*, 1996; Drijfhout *et al.*, 1996), is adjusted to the weather timescale and coupled with an ephemeral tidal model. It is discretized on an Arakawa-C grid with a horizontal resolution of 1.875° and covers the global ocean from 77°S to 90°N. Vertically, 13 layers are realized. The temporal resolution is 30 minutes. The bathymetry is based on the ETOPO5 data set.

Implemented are the physics of the continuity equation and a conservation equation for heat and salt. For the non-linear balance equations for momentum the Boussinesq approximation has been applied. The internal distribution of pressure obeys the hydrostatic equation. Vertical velocities are estimated diagnostically from the incompressibility condition. Water elevations, three dimensional horizontal velocities, the potential temperature and salinity are calculated prognostically. A dynamical, thermodynamic sea-ice model is coupled for the prognostic determination of ice-thickness, compactness and drift (Hibler, 1979). The model is forced with 6 hourly atmospheric data of wind stress, atmospheric surface pressure, 2m-temperature and freshwater fluxes from ERA-40 data of the European Centre for Medium-Range Weather Forecast (ECMWF). First, a spin-up of 265 years is initialized with cyclic boundary conditions to estimate a quasi steady-state circulation. Then, a real-time simulation with ECMWF reanalysis data is done for 1956-2001 and with operational ECMWF data from 2001 onwards.

5.1.2 RL05 OMCT

The described OMCT model configuration has been used for de-aliasing of short-term non-tidal ocean mass variations in the GRACE processing in the AOD1B RL04 data product. When assessing sub-monthly GRACE solutions (i.e. ITG-GRACE2010, Kurtenbach *et al.* (2009)), some weaknesses of OMCT to model sub-monthly variability, has been exposed (Bonin & Chambers, 2011). Therefore, a new configuration for OMCT has been implemented and used for the AOD1B RL05 product published in 2013 (Dobslaw *et al.*, 2013).

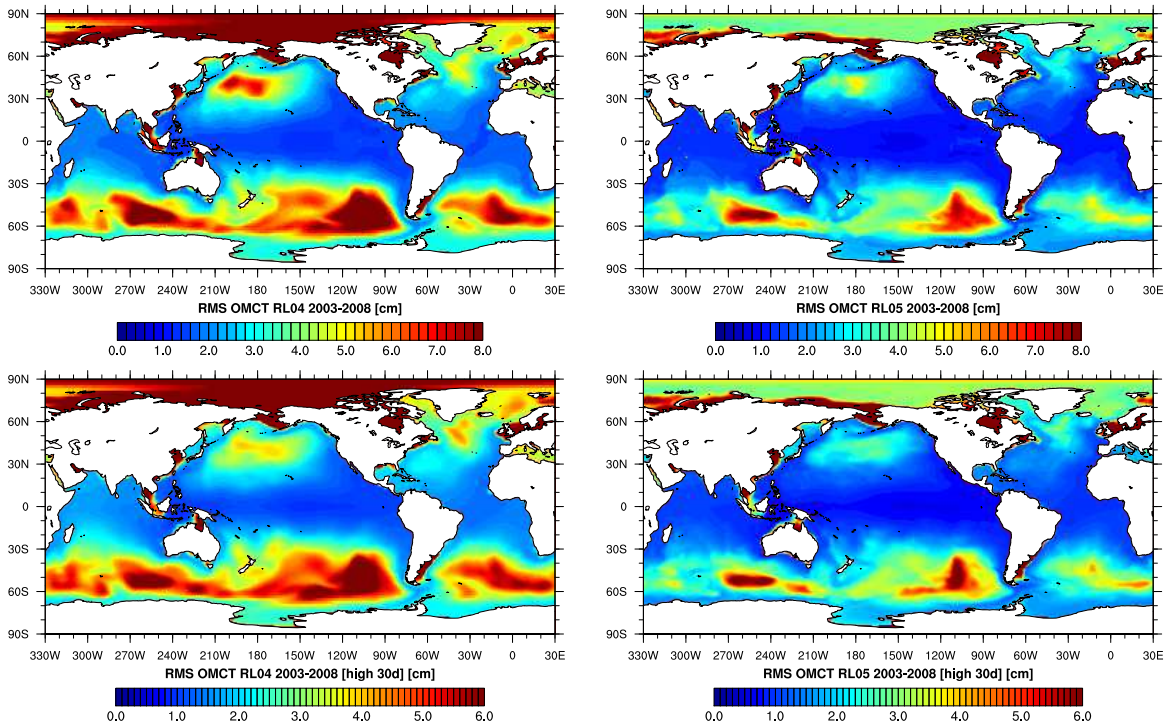

Figure 5.1: Standard deviation of unfiltered (top) and high pass filtered (bottom) ocean bottom pressure variability from OMCT RL04 (left) and RL05 (right) expressed in equivalent sea-water height for the period 2003-2008

The horizontal resolution has been increased to 1°, 20 vertical layers are discretized and the time step has been augmented to 20 minutes due to stability criterions. There is no implementation of river runoff and dynamical effects due to self attraction and loading of the water column are also not taken into account. The horizontal eddy viscosity and vertical momentum transfer parameters have been adjusted to be comparable with observations of bottom pressure and sea level variability. The real-time simulation is done with the new ERA Interim forcing (1979-2001) and the operational ECMWF forcing from 2001 onwards.
Due to sub-diurnal variability in the atmospheric forcing data related to atmospheric tides, the signal has been reduced in the ocean bottom pressure data by a harmonic fit over the years 2001-2002. The semidiurnal tide S_2(p) is already included in the tidal correction in the GRACE processing and else would be corrected twice if not removed from the OMCT grids. Finally, ocean bottom pressure variations are calculated relative to the mean field of 2001-2002.

5.1.3 Validation of the new RL05 OMCT model run

By reducing mean, trend, annual and semi-annual signals, the variability of the residual OBP fields expressed in cm of equivalent water height of RL05 is smaller compared to RL04 (see Fig. 5.1). Especially, the signal in the Arctic Ocean has been decreased by 4 cm. The Arctic Ocean is connected to the Pacific and North Atlantic Ocean by small narrow straits (Bering Strait and Fram Strait). The higher spatial resolution of RL05 leads to a better representation of these straits and therefore also to a better inverse barometric adjustment of the Arctic basin. Strong variability occurs in the Southern Ocean and in the midlatitudes of the North Pacific and the Nordic Sea. In RL05, the maximum amplitudes are located in the region south-westward of South America and southern of Australia whereas in RL04 larger pattern of strong variability in the Southern Ocean can be observed. This results from higher spatial resolution in RL05. In the tropical region the variability is nearly zero. There is really small wind-driven bottom pressure variations in this region due to baroclinic processes in the highly stratified upper ocean which compensate a large amount of wind-effects affecting ocean bottom pressure variations (Gill & Niiler, 1973). To analyze the improvement of RL05 to model reliable sub-monthly ocean bottom pressure variations, high pass filtering with a 30-days Butterworth filter has been applied (see Fig. 5.1), where most of the variability is preserved in the sub-monthly frequency domain.

In the next step, the new model configuration has been validated against in situ ocean bottom pressure observations from ocean bottom pressure recorders (OBPR) and sea level height variations from altimeter observations (Jason1, ENVISAT). To assess the information content in the sub-monthly frequency domain, a 30-days high pass Butterworth filter has been applied to all data sets.
Totally, 83 OBPR stations (see Appendix A) from the database of Macrander *et al.* (2010) are used for comparison of the RL04 and RL05 model data. With RL04, for 60 stations, the variability, assessed by calculations of absolute and relative explained variances according to von Storch & Zwiers (2003) (see Fig. 5.2), cannot be achieved with the modeled pressure data. 17 Stations explain up to 20% and only 5 stations up to 40% of the pressure variability in the different regions. Just for one station in the north Pacific (station 48) 70% variability is explained by the RL04 model data. OBP variability for this station is increased up to 83% in RL05. Up to 60% variability is explained by 68 stations where the average is around 20% to 40%.

As proposed by Bonin & Chambers (2011) satellite altimetry data from Jason-1 and ENVISAT for the period 2003–2008 have been used for further validation. The along-track ellipsoidal sea surface heights have been processed as described in Dobslaw *et al.* (2013).

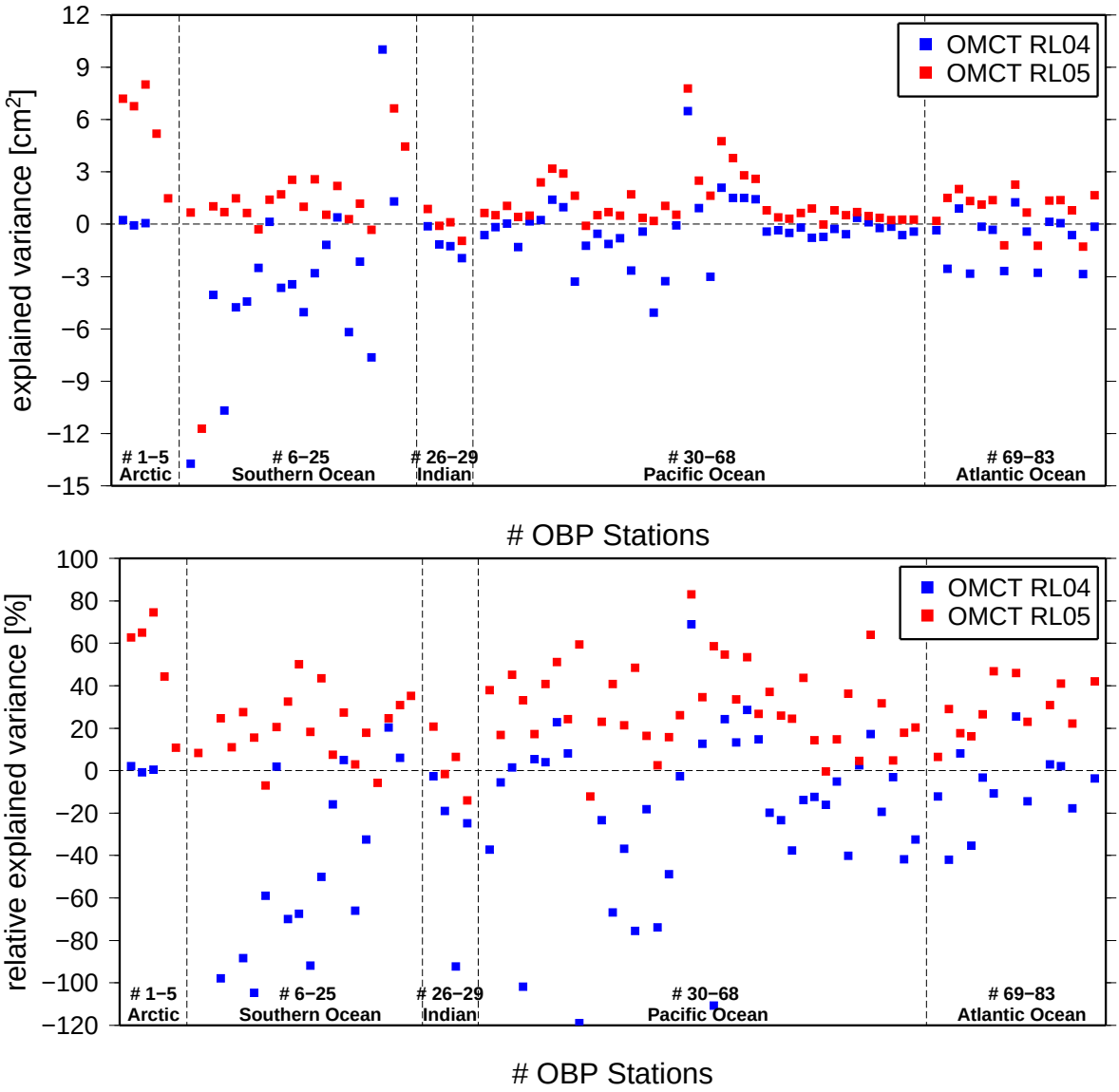

Figure 5.2: Absolute (top) and relative (bottom) explained variances of high pass filtered ocean bottom pressure at OBPR stations and OMCT RL04 (blue) and RL05 (red)

AOD1B RL04 and RL05 have been optionally applied as a correction model for the sea level anomalies. The along-track data have been interpolated to a 1° grid with daily resolution. In Fig. 5.3 the temporal variability of both data sets, solely corrected for variations in SSH induced by atmospheric pressure variations (also known as inverse-barometric (IB) correction), is shown.

High variability in sea level anomalies is shown in the western parts of the Pacific and Atlantic on the northern and southern hemisphere and in the region of the Antarctic Circumpolar Current (ACC). These are also preserved in the high pass filtered data. In these regions mesoscale

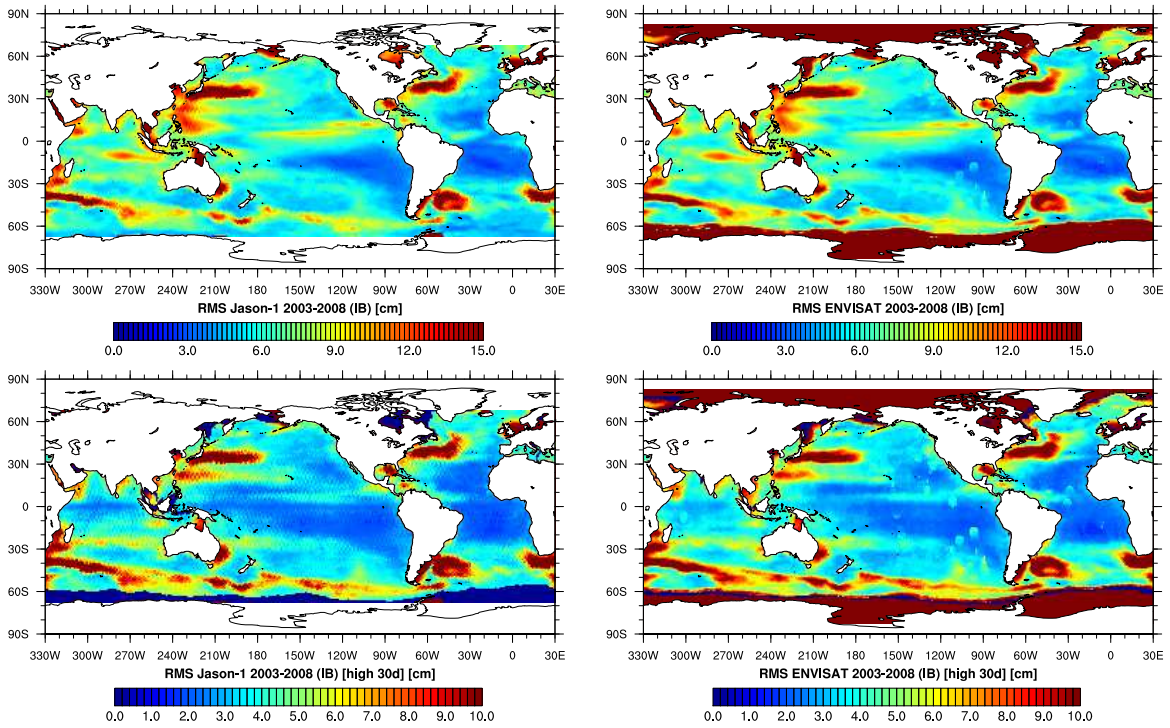

Figure 5.3: Standard deviation of unfiltered (top) and high pass filtered (bottom) sea level variability from inverse barometric corrected Jason-1 (left) and ENVISAT (right) observations for the period 2003-2008

variability is induced due to western boundary currents. In the upper ocean-layers density anomalies are induced which cannot be seen in the bottom pressure data. Apart from the western boundary, weather patterns cause sea level variability of 1 to 3 cm which are inherently barotropic and are observable in ocean bottom pressure observations. According to Gill & Niiler (1973) the response of sea level due to the upper wind field is a combination of barotropic and baroclinic signal in the mid-latitudes where the higher latitudes are more barotropic and becomes baroclinic towards the equator. This suggests, that a fraction of the sub-monthly variability of sea level is captured by altimetry observations of Jason-1 and ENVISAT.

In the next step, the AOD1B RL04 and RL05 data are used as an additional geophysical correction model for the along-track data. To asses the reduction of the variability the absolute and relative explained variances (von Storch & Zwiers, 2003) are calculated (see Fig. 5.4 and Fig. 5.5). The results for Jason-1 and ENVISAT are quite consistent for both RL04 and RL05. Absolute explained variances of around 10 cm^2 are found in the Southern Ocean, the North Pacific and the South China Sea. RL04 shows large regions in the south Atlantic, Pacific and Indian Ocean where the explained variances are negative, whereas RL05

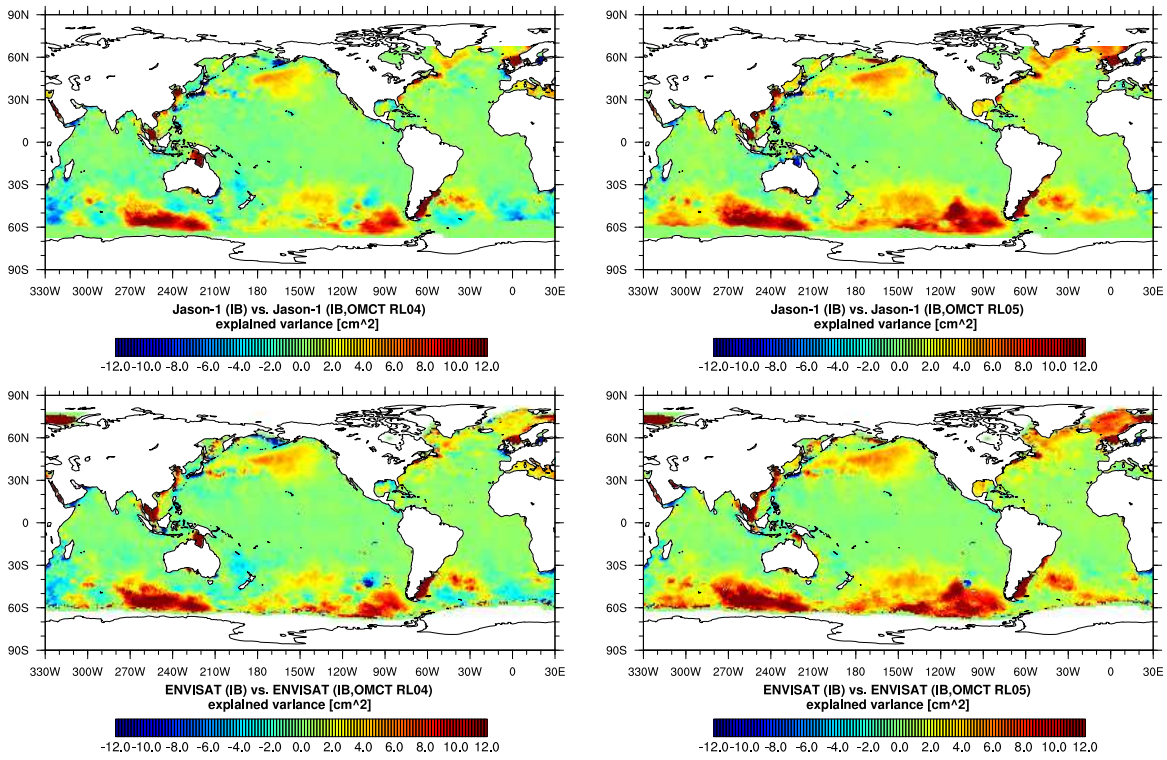

Figure 5.4: Absolute explained variances of high pass filtered sea level variability from inverse-barometrically corrected observations from Jason-1 (top) and ENVISAT (bottom) by ocean bottom pressure variations taken from OMCT RL04 (left) and OMCT RL05 (right)

shows more ability to solve for these variabilities with explained variances of around 1 to 6 cm^2. Around 40% of sea level variability is explained by the new model configuration in the Southern Ocean. Contrary to the results in the Southern Ocean, RL05 shows discrepancies in the Golf of Carpentaria (north of Australia). In this region more sea level variability is explained by RL04. This result is due to the bathymetry used for RL05. The Torres Strait is modeled too deep and too wide to achieve a realistic simulation of the free oscillation in this basin. Explained variances are low in regions, where strong mesoscale eddy activity are observed, i.e Gulf Stream, Agulhas region or the ACC. Besides the dominance of the steric component in the altimetry based sea level data, the spatial resolution of OMCT is not sufficient for resolving these features. RL05 also explains more of the altimetry residuals in the North Atlantic than RL04. Except for the Gulf Stream region, up to 15% variability is explained by the new model configuration with a maximum of around 40% in the Fram Strait and East Coastal Greenland Current.

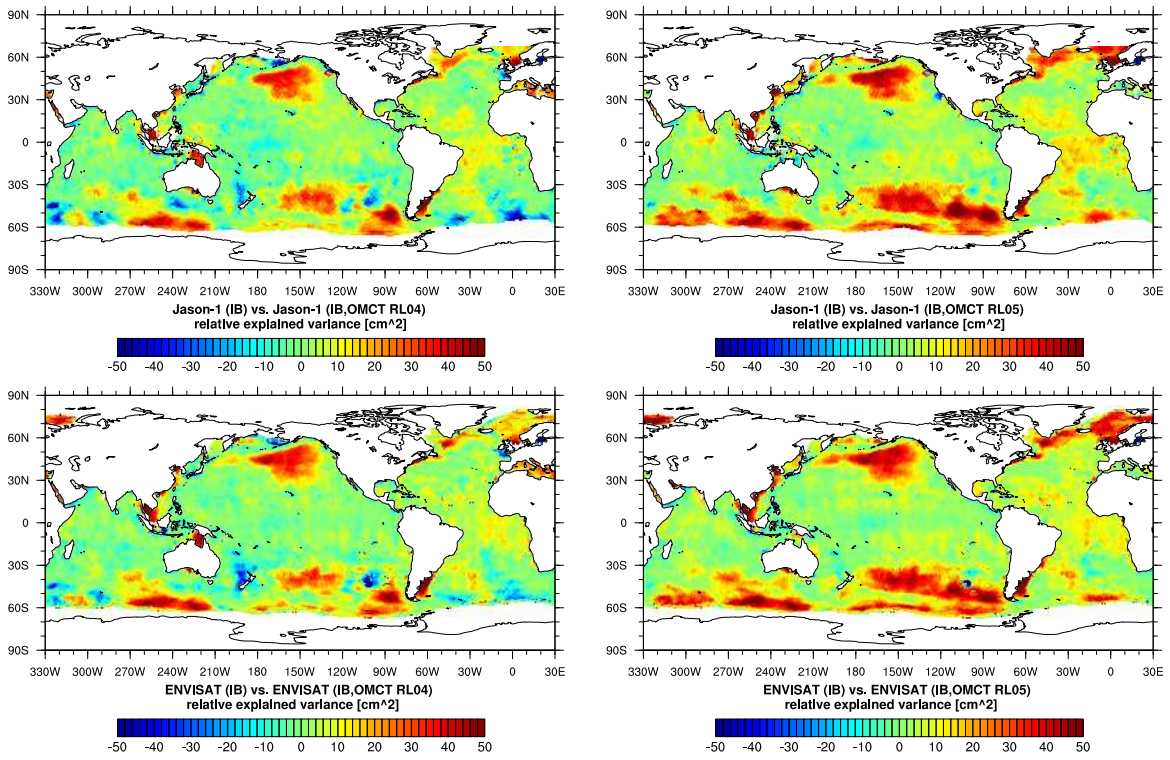

Figure 5.5: The same as Fig. 5.4 but for relative explained variances

The results of the comparison with OBPRs and altimetry based sea level data are in agreement to each other and leads to the conclusion that the new model configuration of OMCT is able to better reproduce the sub-monthly dynamical processes in the redistribution of ocean mass.

5.2 The ESA Earth System Model

The simulation of mass redistribution at the Earth's surface is a necessary step in the development of new satellite gravity missions. The modeled spatial and temporal mass variations are used as a source model for orbit computations of future satellite missions. The source model has to represent at one side high-frequency mass variations in atmosphere and ocean for realistically including the effects of temporal aliasing in the simulated gravity fields. On the other side, monthly to inter annual signals have to be modeled with realistic amplitudes, especially at small spatial scales, to assess the ability of the new satellite mission to monitor these signals. Therefore, an updated version of the Earth System Model (ESM) of Gruber *et al.* (2011) has been recently released by the GFZ (Dobslaw *et al.*, 2014; Bergmann-Wolf *et al.*, 2014).

The ESM consists of mass variability in atmosphere, ocean, terrestrial hydrology including

the ice-sheets and glaciers and due to Solid Earth processes. For each contribution, spherical harmonic coefficients are provided up to degree and order 180 with a temporal resolution of 6 hours over a period of 12 years (1995–2006).

For the atmospheric component the latest re-analysis from ECMWF, ERA-Interim, has been used. It represents the atmosphere over the last decades and models well the atmospheric part of the global water cycle. The grids of atmospheric surface pressure have a temporal and spatial resolution of 6 hours and 0.5°. The mean signal and semi-diurnal tide S_2(p) have been removed. Additionally, a modification of the classical IB correction has been applied to realize independent pressure field variations for the atmosphere and ocean. A detailed description therefore is given in Dobslaw *et al.* (2014).
The terrestrially stored water masses are taken from the Land Surface Discharge Model (LSDM; Dill, 2008) where the vertical and lateral water transport and storage on land surfaces have been modeled. LSDM is based on Hagemann & Dümenil (1997) and includes soil moisture, snow storage and water stored in rivers and lakes. Daily mass grids with a spatial resolution of 0.5° are given, where mass variability in the LSDM in the regions of Antarctica and Greenland has been masked out because they are included in the ice component. After removing the temporal mean field the grids are interpolated to 6-hourly time steps.
The ice component has been modeled with the regional climate model RACMO2 (Ettema *et al.*, 2009). The model provides high-resolution estimates of surface mass balance of glaciated regions in Greenland and Antarctica. The daily data are discretized on grids with a spatial resolution of 11 km. Additionally, ice dynamics, which mainly determine the low-frequency ice mass balance, were taken from the re-synthesized ESM of Gruber *et al.* (2011). The ice mass balance for four groups of glaciers in Alaska, the Alps, the Himalayan and the Karakoram Mountain Range where included by means of linear trends. These have been calculated from data from the World Glacier Inventory.
The Solid Earth component consists of three different signals: (1) linear trends of Glacial Isostatic Adjustments, (2) co-seismic deformations due to the Sumatra-Andaman Earth Quake between 00:00 and 6:00 on December 26th and followed (3) by a linear increasing post-seismic deformation for one year. These signals have also been used from the original ESM model of Gruber *et al.* (2011). The data have been reprocessed to eliminate the strong Gibb's effects at the edge of the earth quake which has been patched in the GIA trends not very well. Due to the realization of the solid Earth component in the Centre of Figure frame (see Chapter 6.1), additional degree-1 terms are needed. These were calculated as given in Klemann & Martinec (2011).
A more detailed description of the ocean component will be given in the next section.

5.2.1 A combined ocean model

The ocean component of ESA ESM consists of two models: (1) the Ocean Model of Circulation and Tides and (2) the STORM experiment from the MPIOM model.
The latest RL05 of OMCT has been used with the same settings except the atmospheric forcing has been done with ERA-Interim. The area-averaged atmospheric surface pressure has been subtracted because it is already included in the atmospheric component. Also small variations in total ocean mass resulting from the Boussinesq approximation were reduced, and the response to the atmospheric semi-diurnal S_2(p) tide is reduced. Local trends for the whole time period were removed because they are not reliable (Dobslaw *et al.*, 2013). The time-mean for 12 years has been removed to arrive at 6 hourly grids of ocean bottom pressure anomalies.
Due to the spatial resolution of OMCT of 1° information of mesoscale variability cannot be resolved. Therefore, an experiment of the MPIOM ocean model has been taken into account which provides data with a spatial resolution of 0.1° on a tripolar curvilinear grid (Storch *et al.*, 2012). Even though only daily data are available, the model contains dominant small-scale ocean bottom pressure variability in regions with mesoscale upper-ocean variability (e.g. Antarctic Circumpolar Current) and steep gradients in bathymetry. These mesoscale features have auto-correlation length scales of several days and might be principally observable by future gravity missions (Kuhlmann *et al.*, 2013). As for OMCT, variations in total ocean mass and trends were reduced and the time-mean subtracted for the whole period. Finally, the residuals are interpolated to 6-hourly grids.
The small-scale variability is represented in the higher degree and order (d/o) Stokes coefficients. OMCT cannot resolve these features, so both data sets were combined in the spectral domain. OMCT has been taken for the lower spherical harmonics up to d/o = 60 whereas MPIOM contributes with the small-scale features from d=61 up to d/o = 180.

Due to the mass preservation of the Earth's system model, variations in total ocean mass have to equalize mass variations in the atmosphere, terrestrially stored and in the cryosphere. Mass inflow from land redistributes nearly homogeneously after a few days (Dobslaw & Thomas, 2007; Lorbacher *et al.*, 2012) and will lead to a homogeneous response of the ocean bottom pressure field. Therefore, total mass variations of the atmospheric, terrestrial water and ice part have been taken, summarized and added inversely to the ocean component. The global eustatic sea level variations are determined with (Dobslaw *et al.*, 2014)

$$\delta\sigma(\theta,\lambda) = -\frac{\Omega}{\Omega_{ocean}}\tilde{P}_{00}(\cos\theta)\{\Delta C_{00}^{A} + \Delta C_{00}^{H} + \Delta C_{00}^{I}\} \tag{5.1}$$

where Ω is the global area, Ω_{ocean} the area of the ocean and $\{\Delta C_{00}^{A}, \Delta C_{00}^{H}, \Delta C_{00}^{I}\}$ the total mass variations in atmosphere, terrestrial stored water and cryosphere.

Chapter 6

Assessment of global mean sea level variations from space: oceanographic contributions from the GRACE mission

According to the fifth Assessment Report (AR5) of the Intergovernmental Panel on Climate Change (IPCC), a rate for Global Mean Sea Level (GMSL) rise of 1.7±0.2 mm/yr between 1901 and 2010 has been detected, whereas for the last 17 years (1993–2010) a higher rate of 3.2±0.5 mm/yr has been determined. The main contributions to sea level rise are thermal expansion and glacier and ice-sheet melting which explain up to 87.5% of the observed total sea level rise (Church *et al.*, 2013). Especially from thermal expansion due to warming of the ocean, the mean sea level will rise continously beyond 2100.

The main non-antropogenic climate-sensitive processes which have an effect on the global and regional sea level variations are displayed in Fig. 6.1. Internal ocean processes are e.g. currents induced by changes in the ocean properties temperature and salinity in different depths. They describe the steric part of sea level variations and lead to a change in the ocean volume but not in ocean mass. Changes in atmospheric pressure and surface winds result also in sea level variations on local up to large spatial scales due to the interaction of atmosphere and ocean. Atmospheric and oceanic modes which describe the mean variability of specific features are helpful for the interpretations of short-term processes observed in both domains and their connection (see Ch. 7).

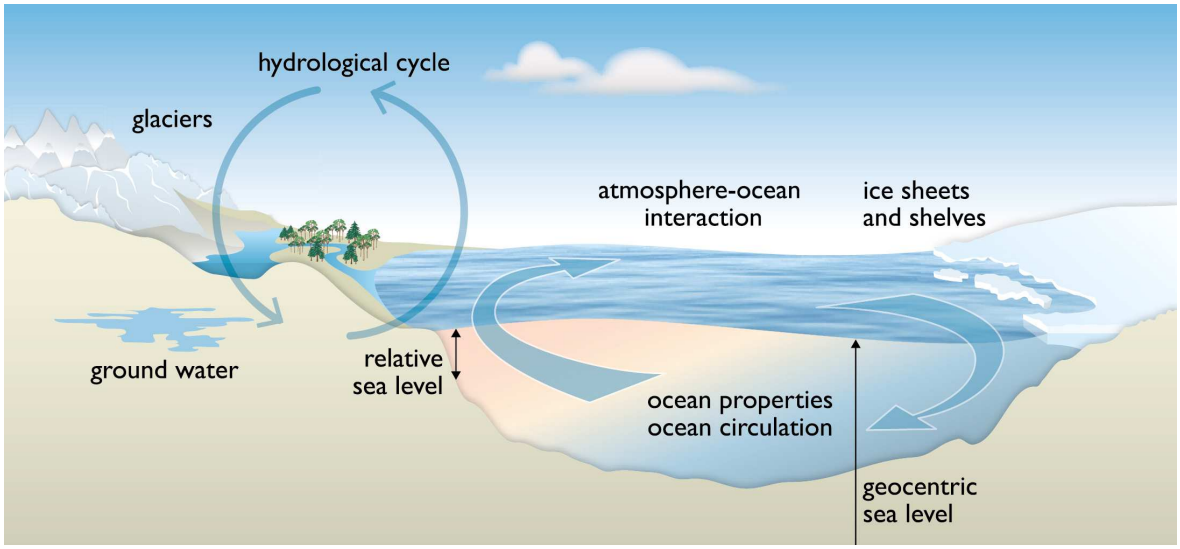

Figure 6.1: The main climate-sensitive processes affecting global and regional sea level variations (Church *et al.*, 2013)

Mass exchange of water and ice between land and ocean due to the hydrological cycle results in a change in global ocean mass. Due to the local fresh water inflow also a secondary change in the steric component is induced. Whereas added mass is distributed homogeneously after a few days, steric changes will appear on longer time scales up to several decades to distribute around the global ocean. The mass contribution from specific regions, like Greenland or Antarctica, lead to specific sea level patterns, which are also called 'sea level fingerprints', affecting also the gravity field due to effects of loading and self attraction.

Besides natural climate variability, anthropogenic effects have also an influence on sea level change. Especially ground water masses and those stored in artificial reservoirs, affect the hydrological cycle due to changes in evaporation and runoff and therefore also the sea level.

With the launch of the remote sensing missions ERS-1 in 1991 and TOPEX/Poseidon in 1992, both equipped with a radar altimeter, reliable estimates for sea level variations with nearly global coverage become available. With the follow-on satellite missions ERS-2 (1995), Jason-1 (2001), Envisat (2002) and Jason-2 (2008) the sea level rise has been estimated to 3.5±0.4 mm/yr for the previous 15 years (Mitchum *et al.*, 2010). Satellite altimetry is based on radar pulses transmitted by the space-born altimeter which are reflected at the ocean surface and received back. By recording the propagation time the height of the satellite above the current sea surface is estimated (Torge, 1991). After correcting for instrumental effects, atmospheric effects and ocean tides, the sea surface height relative to the reference ellipsoid is determined. The results include steric and mass effects which cannot be separated

from each other based on altimetry observations only. To assess the mass component, the difference between altimetry based sea surface heights and estimates of the steric component from in situ observations has to be computed.

Since the launch of the GRACE satellites direct measurements of the mass component affecting sea level change are available. First results of Chambers (2004) after 1.5 years of the mission lifetime already show a good correspondence of global ocean mass estimates from GRACE and altimetry based values reduced by the steric component. Also for the first time, the importance of the degree-1 terms in GRACE solutions for the correct determination of global ocean mass variations was identified. For the period 2002–2015, continuous studying of global ocean mass variability from GRACE data explored connections to the climate-sensitive processes as mentioned in Fig. 6.1. For the last decade (2003–2012) an average rate of 1.8±0.4 mm/yr of global ocean mass expressed in sea level change has been detected (Church *et al.*, 2013). The rate is highly affected by the chosen GIA model for correcting the GRACE data (Quinn & Ponte, 2010). By comparing the GIA model of Peltier (2004) (ICE-5G (VM2)) and Paulson *et al.* (2007) two significant errors in the first one have been found which lead to substantial differences in estimated sea level changes when applied on GRACE data. Especially, secular rates in the degree 2 order 1 coefficients of Peltier's model change the GIA correction of about 27% compared to 2% of Paulson et. al model (Chambers *et al.*, 2010).

6.1 Global eustatic sea-level variations for the approximation of geocenter motion from GRACE

Published as: Bergmann-Wolf, I., Zhang, L. and Dobslaw, H., 2014: Global eustatic sea-level variations for the approximation of geocenter motion from GRACE, Journal of Geodetic Science, 4(1) , doi:10.2478/jogs-2014-0006.

Abstract: Global degree-1 coefficients are derived by means of the method by Swenson *et al.* (2008) from a model of ocean mass variability and RL05 GRACE monthly mean gravity fields. Since an ocean model consistent with the GRACE GSM fields is required to solely include eustatic sea-level variability which can be safely assumed to be globally homogeneous, it can be empirically derived from GRACE as well, thereby allowing to approximate geocenter motion entirely out of the GRACE monthly mean gravity fields. Numerical experiments with a decade-long model time-series reveal that the methodology is generally robust both with respect to potential errors in the atmospheric part of AOD1B and assumptions on global degree-1 coefficients for the eustatic sea-level model. Good correspondence of the

GRACE RL05-based geocenter estimates with independent results let us conclude that this approximate method for the geocenter motion is well suited to be used for oceanographic and hydrological applications of regional mass variability from GRACE, where otherwise an important part of the signal would be omitted.

6.1.1 Introduction

For about twelve years now, the Gravity Recovery and Climate Experiment (GRACE) satellite mission captures the time-variations in the Earth's gravity field at very large spatial scales. By assuming that low-frequency variations - i.e., at periods ranging from about 30 days to several years - take place entirely in a thin layer close to the surface of the solid Earth, those gravity field variations are unambiguously translated into mass anomalies (Wahr *et al.*, 1998). These are primarily related to water re-distributions at and between the continents and the oceans.

Time-series of monthly mean gravity fields provided by the GRACE project are routinely calculated in a reference frame related to the center-of-mass of the Earth System (CM). The corresponding degree-1 terms of the spherical harmonic expansion are therefore zero by definition. Thus, mass anomalies for any regional average obtained from those series entirely neglect all contributions related to the offset between the center-of-mass and a center-of-figure (CF) frame, which is commonly denoted as geocenter motion (Petit & Luzum, 2010). In view of the high precision of GRACE estimates, however, geocenter motion contributions have been found non-negligible for both oceanographic (Chambers & Willis, 2009), and hydrologic applications (Chen *et al.*, 2005).

Geocenter motion is typically derived from satellite laser ranging (SLR) observations to geodetic satellites as, e.g., LAGEOS and STELLA, that relate the kinematic orbits of those satellites to stations realizing the terrestrial reference frame (Chen *et al.*, 1999; Eanes, 2000; Crétaux, 2002). Alternatively, observations of the global network of GPS permanent stations allow also for the derivation of geocenter variations (Blewitt *et al.*, 2001; Lavallée *et al.*, 2006; Fritsche *et al.*, 2010). More recently, promising results of geocenter motion estimates have been reported for joint inversions of a wide number of different observations, i.e. satellite altimetry over the oceans, GPS permanent station observations, in-situ ocean bottom observations, GRACE time-variable gravity fields (Davis, 2004; Jansen *et al.*, 2009; Rietbroek *et al.*, 2012). Partially augmented by information from geophysical models, those joint inversions provide geocenter motion estimates that are presumably more robust and less noisy than results from a single observing system alone.

Since geocenter motion estimates from all the methods mentioned above typically have latencies of several weeks to months, it would be highly beneficial to approximate the geocenter from data of the GRACE mission alone. A method allowing such an approximation has been proposed by Swenson *et al.* (2008). Their algorithm essentially assumes that from the a-priori knowledge of mass distribution at a sufficiently large fraction of the Earth's surface, the missing global degree-1 coefficients and thus the geocenter motion can be derived. The global oceans are the typical domain of choice, but other regions are in principle possible as well.

During the GRACE gravity field processing, high-frequency tidal and also non-tidal mass variability is de-aliased by means of time-variable background models (Flechtner & Dobslaw, 2013). The GRACE Level-2 monthly mean gravity fields - the so-called GSM fields - thereby do not include signals related to atmospheric mass variability. GSM fields also do not include ocean bottom pressure anomalies caused by regionally varying surface winds. They include however, signals related to the eustatic contribution to global sea-level, since this effect has been intentionally excluded from the de-aliasing model (Flechtner & Dobslaw, 2013). Note that the monthly-mean averages of both atmospheric and oceanic non-tidal variability removed during the de-aliasing process are provided as GAC products along with the GSM fields and therefore can be restored for further analysis if appropriate.

In order to approximate degree-1 coefficients consistent with the GRACE GSM fields with Swenson's method, a model of the eustatic contribution to global sea-level is required. Net-inflow of freshwater into the global ocean raises the sea-level homogeneously (Dobslaw & Thomas, 2007; Lorbacher *et al.*, 2012) as long as effects of loading and self-attraction (Tamisiea, 2011; Kuhlmann *et al.*, 2011) are not taken into account. Thus, such a model of the eustatic variation of the sea-level might be derived empirically from the GRACE gravity fields - by incorporating the assumption of a globally homogeneous response of sea-level to a net-flux of water.

The present paper is structured as follows: First, the essentials of the method of (Swenson *et al.*, 2008) are re-called in section 1. Next, we are going to test Swenson's method with the help of a numerical mass transport model developed for future satellite gravity mission simulation experiments. The model realistically includes mass re-distributions among and within atmosphere, cryosphere, continental hydrosphere and the global oceans (section 2). Subsequently, we assess different processing strategies to empirically derive a model of the global eustatic sea-level variations from GRACE (section 3), that are finally applied iteratively to Swenson's method to arrive at a refined approximation of the geocenter motion that is

finally discussed with respect to independent estimates from alternative geodetic techniques in section 4.

6.1.2 Methodology of Swenson *et al.* (2008)

The method to approximate geocenter motion introduced by Swenson *et al.* (2008) is essentially based on the fact that we can separate the surface mass signals into different components. The mass distribution at any position on a sphere is described from a (truncated) series of global spherical harmonic coefficients:

$$\Delta\sigma(\theta,\phi) = \sum_{l=0}^{\infty}\sum_{m=0}^{l} \tilde{P}_{lm}(\cos\theta)\{\Delta C_{lm}\cos m\phi + \Delta S_{lm}\sin m\phi\} \tag{6.1}$$

By setting a certain fraction of the sphere's surface - let's say all continental regions - to zero, a second series of spherical harmonic coefficients might be analyzed, that lead to identical mass distributions in the oceanic regions when re-synthesized:

$$\Delta C_{lm}^{ocean} = \frac{1}{4\pi}\int d\Omega\ \tilde{P}_{lm}(\cos\theta)\cos m\phi\ \vartheta(\theta,\phi)\ \sigma(\theta,\phi) \tag{6.2}$$

Here, ΔC_{lm}^{ocean} are called ocean coefficients in the remainder of this paper in order to distinguish them from the global coefficients ΔC_{lm}, and ϑ is a binary field separating land from ocean. By utilizing the orthogonality of the associated Legendre functions on the sphere, every single ocean coefficient might be analyzed individually:

$$\begin{aligned}\Delta C_{lm}^{ocean} = \frac{1}{4\pi}\int d\Omega\ \tilde{P}_{lm}(\cos\theta)\cos m\phi\ \vartheta(\theta,\phi)\\ \cdot\sum_{l'=0}^{\infty}\sum_{m'=0}^{l}\tilde{P}_{l'm'}(\cos\theta)\{\Delta C_{l'm'}\cos m'\phi + \Delta S_{l'm'}\sin m'\phi\}\end{aligned} \tag{6.3}$$

We now write the summation in Eq. (6.3) for the global coefficients of degree 1 explicitly:

$$\begin{aligned}\Delta C_{10}^{ocean} &= \Delta C_{10} \cdot \frac{1}{4\pi} \int d\Omega\ \tilde{P}_{10}(\cos\theta)\vartheta(\theta,\phi)\tilde{P}_{10}(\cos\theta) \\ &+ \Delta C_{11} \cdot \frac{1}{4\pi} \int d\Omega\ \tilde{P}_{10}(\cos\theta)\vartheta(\theta,\phi)\tilde{P}_{11}(\cos\theta)\cos\phi \\ &+ \Delta S_{11} \cdot \frac{1}{4\pi} \int d\Omega\ \tilde{P}_{10}(\cos\theta)\vartheta(\theta,\phi)\tilde{P}_{11}(\cos\theta)\sin\phi \\ &+ \frac{1}{4\pi} \int d\Omega\ \tilde{P}_{10}(\cos\theta)\vartheta(\theta,\phi) \\ &\cdot \sum_{l=0}^{\infty}\sum_{m=0}^{l} \tilde{P}_{lm}(\cos\theta)\{\Delta C_{lm}\cos m\phi + \Delta S_{lm}\sin m\phi\} \end{aligned} \tag{6.4}$$

where the summation in Eq. (6.4) has to be read to exclude $\Delta C10$, $\Delta C11$, and $\Delta S11$. Equation (6.4) is re-expressed once more in a more compact form

$$\Delta C_{10}^{ocean} = \Delta C_{10} \cdot I_{10C}^{10C} + \Delta C_{11} \cdot I_{11C}^{10C} + \Delta S_{11} \cdot I_{11S}^{10C} + G_{10C} \tag{6.5}$$

where we use the notation

$$I_{10C}^{10C} = \frac{1}{4\pi} \int d\Omega\ \tilde{P}_{10}(\cos\theta)\vartheta(\theta,\phi)\tilde{P}_{10}(\cos\theta) \tag{6.6}$$

with the superscript indicating the spherical harmonic to the left of ϑ and the subscript indicating the one to the right, and

$$\begin{aligned} G_{10C} &= \frac{1}{4\pi} \int d\Omega\ \tilde{P}_{10}(\cos\theta)\ \vartheta(\theta,\phi) \\ &\cdot \sum_{l=0}^{\infty}\sum_{m=0}^{l} \tilde{P}_{lm}(\cos\theta)\{\Delta C_{lm}\cos m\phi + \Delta S_{lm}\sin m\phi\} \end{aligned} \tag{6.7}$$

Setting up corresponding equations for ΔC_{11}^{ocean} and ΔS_{11}^{ocean} leads to a linear equation system

$$\begin{bmatrix} \Delta C_{10}^{ocean} \\ \Delta C_{11}^{ocean} \\ \Delta S_{11}^{ocean} \end{bmatrix} = \begin{bmatrix} I_{10C}^{10C} & I_{11C}^{10C} & I_{11S}^{10C} \\ I_{10C}^{11C} & I_{11C}^{11C} & I_{11S}^{11C} \\ I_{10C}^{11S} & I_{11C}^{11S} & I_{11S}^{11S} \end{bmatrix} \begin{bmatrix} \Delta C_{10} \\ \Delta C_{11} \\ \Delta S_{11} \end{bmatrix} + \begin{bmatrix} G_{10C} \\ G_{11C} \\ G_{11S} \end{bmatrix} \tag{6.8}$$

that might be solved for ΔC_{10}, ΔC_{11}, and ΔS_{11} by matrix inversion in case that knowledge about the corresponding ocean coefficients at the left-hand side is available from auxiliary sources. For global GSM-like coefficients as explained above, this needs to be a semi-empirical model of the eustatic global sea-level variability (see chapter 6.1.4).

6.1.3 Numerical experiments

Applying Swenson's methodology described above to obtain GSM-like global coefficients of degree-1 includes a number of potential sources of uncertainty: (i) The geometry of the fraction of the sphere where a priori information is introduced must be sufficiently large and sufficiently shaped to make the I matrix in Eq. (6.8) well conditioned and thereby numerically invertible. (ii) The GRACE GSM fields are obtained by reducing atmospheric and oceanic mass variability with the potentially erroneous time-variable background model AOD1B, thereby contributing to errors in the global coefficients contained in the G vector of Eq. (6.8). (iii) The empirical model of the eustatic sea-level rise based on limited observations might contain errors as well that are introduced into the algorithm via the left-hand side of Eq. (6.8).

Since the consequences of those effects are difficult to assess in general, we test the algorithm with four experiments with a decade-long model time series. For this, we use a numerical mass transport model developed for simulation studies of future satellite gravity missions. The numerical model is an update of the ESA Mass Transport Model (Gruber *et al.*, 2011) and provides spherical harmonics of global mass anomalies complete to degree and order (d/o) 180 for the atmosphere based on ERA Interim (Dee *et al.*, 2011), for the oceans based on OMCT (Dobslaw *et al.*, 2013), for the continental hydrosphere based on LSDM (Dill & Dobslaw, 2013), and for the continental ice-sheets based on RACMO-2 (Ettema *et al.*, 2009), all consistently forced with ERA-Interim atmospheric data. The time-series covers twelve years from 1995 until 2006, and its temporal sampling is six hours. Since we are going to approximate the geocenter on time-scales corresponding to the nominal GRACE sampling, monthly mean averages calculated for each sub-system are used in the following experiments.

In TEST 1, we assume that the mass anomalies over the oceans are known exactly from the mass transport model. We take all coefficients of $\mathrm{d/o} = 0$ and $\mathrm{d/o} \geq 2$ from the sum of ocean, continental hydrology and ice as the global coefficients, and derive degree-1 coefficients with Swenson's method that compare well to the true ones from the mass transport model (Fig. 6.2a). Relative explained variances of more than 99% for all components (Table 6.1) indicate that the geometry of the global ocean is well suited to derive global degree-1 terms with Swenson's algorithm.

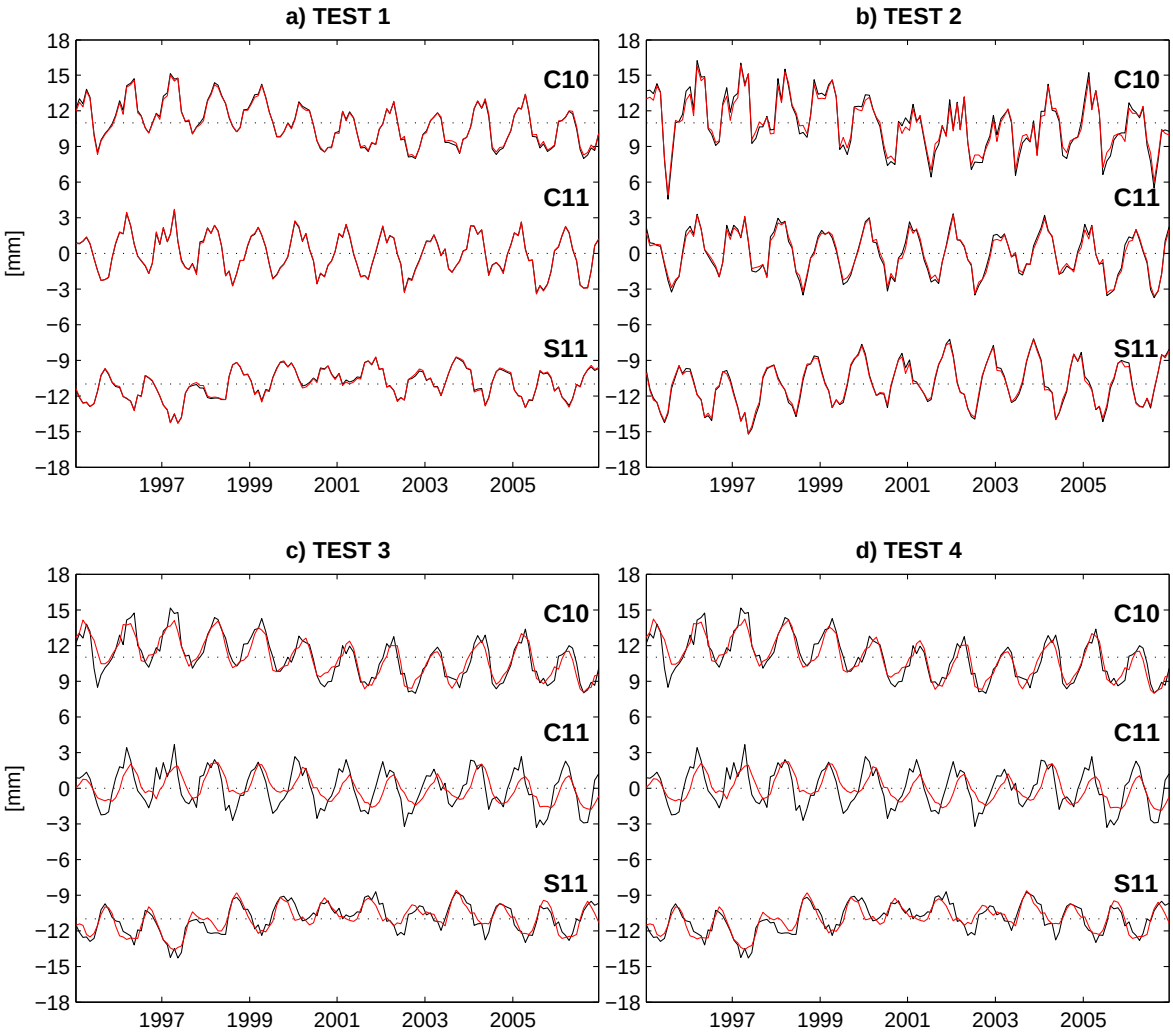

Figure 6.2: Recovery of global geocenter variations in four different test calculations with the updated ESA mass transport model: true model series [black] and estimated with the method of Swenson *et al.* (2008) [red].

For TEST 2, we take again the mass anomalies over the oceans as known, but additionally include the atmosphere into the global coefficents (Fig. 6.2b). By this, we assume that none of the monthly-mean atmospheric contributions has been removed by the time-variable background model AOD1B, which is a quite conservative assumption, since current atmospheric models are generally found to remove a substantial amount of residual variability from the GRACE data (Zenner *et al.*, 2012). Relative explained variances of more than 97% let us conclude that errors in the atmospheric component of the time-variable background model do not affect the methodology seriously, and therefore need not to be considered further in this context.

Table 6.1: Relative explained variance in [%] for the recovery of global degree-1 coefficients in four different test calculations with the updated ESA mass transport model.

	ΔC_{10}	ΔC_{11}	ΔS_{11}
TEST 1	99.48	99.90	99.62
TEST 2	97.21	98.32	99.17
TEST 3	81.79	42.29	76.74
TEST 4	82.28	42.37	76.42

During TEST 3, we take the mass anomalies over the oceans from the mass transport model and calculate a time-series of the globally averaged eustatic sea-level changes. This eustatic sea-level contribution is subsequently spread out equally over the ocean domain of the mass transport model and used together with the global coefficients of TEST 1 to calculate once more the global degree-1 coefficients (Fig. 6.2c). With this experiment, we find substantial deviations between true and recovered global degree-1 coefficients, notably in ΔC_{11}, where only 42% of the variance in the true coefficient is described by the one obtained with Swenson's algorithm and a globally homogeneous model of eustatic sea-level variability. In particular the seasonal variability is affected, with an apparent phase-shift of several weeks. Secular trends, however, are captured well even in this experiment.

Finally, for TEST 4, we repeat the previous experiment but scale the homogeneous model of eustatic sea-level variability with a factor of 1.1 in order to assess the impact of potential errors in the global sea-level model (Fig. 6.2d). By comparing derived global degree 1 coefficients from experiments 3 and 4, we find scaling coefficients of 1.031 for ΔC_{10}, 1.036 for ΔC_{11}, and 0.983 for ΔS_{11}, suggesting that in particular ΔC_{11} and ΔC_{10} are susceptible to errors in the eustatic sea-level model. We will return to those results in the remainder of this paper.

6.1.4 Global eustatic mass variations from GRACE

As outlined above, a model of eustatic sea-level variability in the global oceans is required to derive global GSM-like coefficients with Swenson's method. To obtain one, we follow the approach of Chambers (2004) that is entirely based on GRACE monthly mean gravity fields.

We take the release 05 (RL05) GRACE gravity field solutions of the Deutsches GeoForschungs-Zentrum (GFZ) (Dahle *et al.*, 2012) provided as Stokes coefficients up to degree/order 90 for the period February 2003 to September 2012. We introduce an annual sinusoid for global degree-1 coefficients taken from Eanes (2000). In order to minimize continental leakage, we use an averaging domain that excludes all ocean areas closer than 300 km to the coasts.

Averaging mass variability over the chosen domain has been performed in two different ways as proposed by Swenson (2002): (i) an isotropic Gauss filter, and (ii) the Lagrange Multiplier Method. Where the former method attempts a compromise between satellite and leakage error, the latter will fit the leakage error to satellite errors obtained from the GRACE formal error. Note that due to the large averaging area applied here, the consideration of anisotropic filter algorithms as suggested by Kusche (2007) is not necessary, since it does not notably affect the results. Signal loss, due to the filtering, however, is taken into account by applying re-scaling factors following Klees *et al.* (2007).

For both the Gauss filtering and the Lagrange Multiplier Method, we apply smoothing radii between 0 and 500 km, the corresponding re-scaling factors vary between 1.002 to 1.014, and 1.027 to 1.046, respectively. Amplitudes (Table 6.2) compare well between the two methods, and generally decrease with stronger smoothing, as expected. Formal uncertainties of the amplitudes do not decrease substantially for smoothing radii above 300 km. Differences between the time-series of both methods (Fig. 6.3) are small for 300 km, and show - apart from a slightly differing secular trend - no systematics. Since over-smoothing tends to diminish the signal and increases the chance of continental leakage, and since 300 km is also close to the theoretical spatial resolution limit of GRACE that is determined by the inter-satellite distance of 250 km, and since moreover both methodologies lead to identical amplitudes within their formal uncertainties, we decide to use the 300 km Gauss filtered results for subsequent analysis.

6.1.5 GSM-like global degree-1 coefficients from GRACE

We now introduce the empirical model of eustatic sea-level variability as a a priori information into Swenson's method for the derivation of GSM-like global degree-1 coefficients. For the G vector of Eq. (6.8) we use again GRACE RL05 gravity field solutions from GFZ (Dahle *et al.*, 2012) up to d/o= 90. No additional filtering is applied to the GRACE coefficients at this stage, but to remove the long-term signal of the Glacial Isostatic Adjustment (GIA), we subtract the model of Paulson *et al.* (2007).

We estimate global degree-1 coefficients for the empirical eustatic sea-level model with the methodology of Swenson (Fig. 6.4) and compare them to coefficients based on CSR RL05 solutions from GRACE that are readily available from the GRACE TELLUS website [1] maintained by Sean Swenson. In general, we note good agreement between both solutions, in particular with respect to secular changes and annual amplitudes. Small month-to-month

[1] http://grace.jpl.nasa.gov/data/degree1

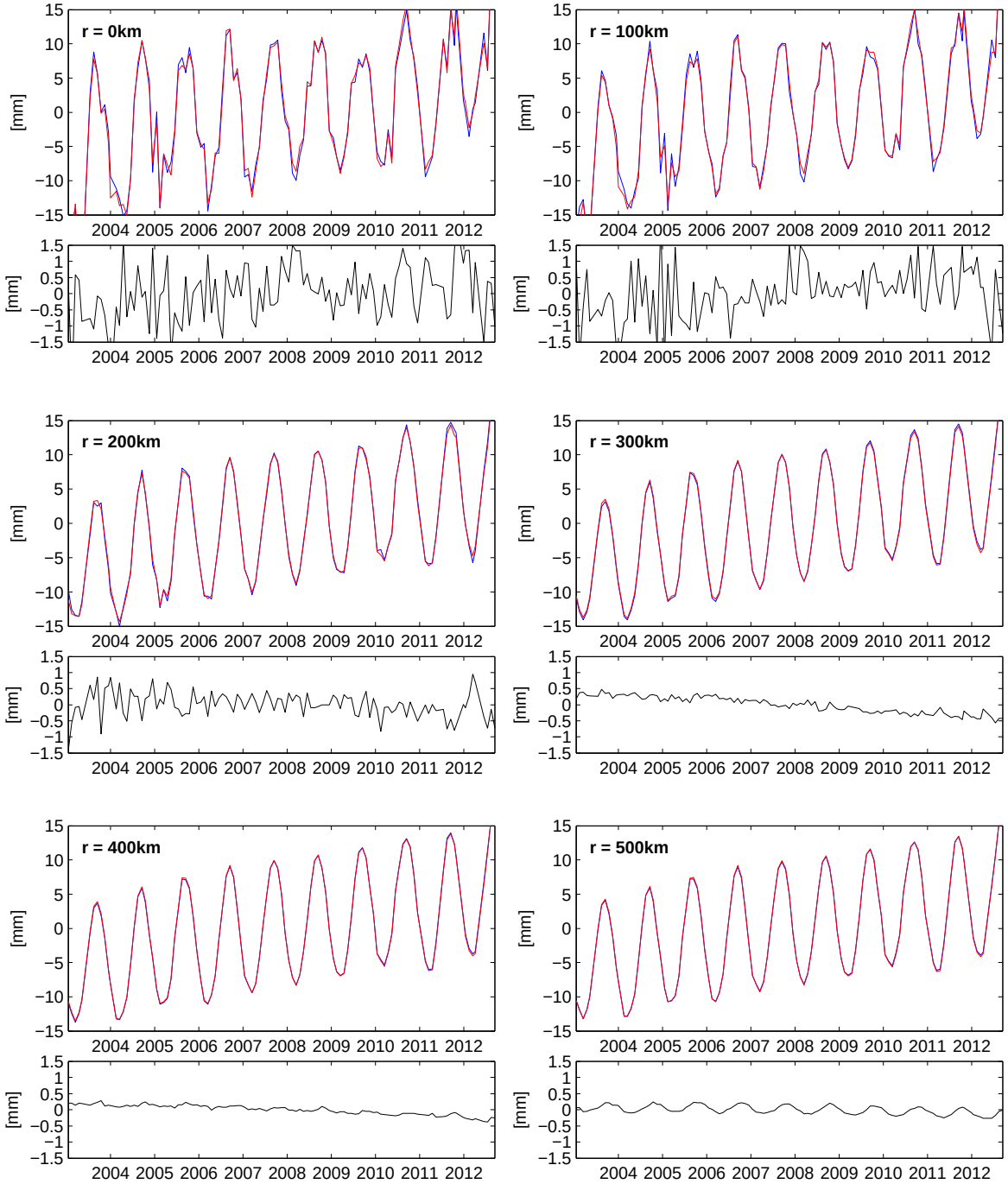

Figure 6.3: Global ocean mass variations estimated with Gauss Filter [red] and Langrange-Multiplier-Method [blue] for different filter radii (r = 0, 100, ... , 500km). The differences between both methods (red - blue) are given in the subplot below each plot.

Table 6.2: Annual amplitude and phase of global ocean mass variations determined from GRACE GFZ RL05 with a) Gauss Filter and b) Lagrange-Multiplier-Method for different filter radii.

	Amplitude [mm]	Phase [days]
a) Gauss Filter		
r = 0km	10.33±2.28	257
r = 100km	10.03±0.80	257
r = 200km	9.69±0.18	255
r = 300km	9.53±0.12	255
r = 400km	9.45±0.11	254
r = 500km	9.37±0.10	254
b) Lagrange-Multiplier-Method		
r = 0km	10.37±2.30	257
r = 100km	10.25±1.11	257
r = 200km	9.77±0.24	255
r = 300km	9.57±0.13	255
r = 400km	9.41±0.11	254
r = 500km	9.26±0.10	254

differences exist, however, which are related to the different GRACE series applied, and to the specifics of the processing of the eustatic sea-level variability model. In addition, we note stronger deviations between both solutions after 2011, when GFZ RL05 solutions were found to be overly constrained to secular trends in a time-variable low-degree background model, which eventually led to the replacement of RL05 with RL05a in autumn 2013 (see Release Note for GFZ RL05 GRACE L2 Products, C. Dahle, 2014, isdc.gfz-potsdam.de).

We now return to the fact that we introduced a priori information on the global degree-1 coefficients from (Eanes, 2000) into the eustatic sea-level variability model, which in principle can be replaced by the newly derived global degree-1 coefficients as given in Fig. 6.4. We therefore repeat the calculations for the global model of eustatic sea-level variability, re-do the degree-1 estimation with Swenson's method, and iterate five times. Decreasing increments during those iterations indicate good convergence of the method (Fig. 6.5). In addition to this reference calculation, we perform an experiment 1 by setting the global degree-1 coefficients to zero in the initial calculation of the eustatic sea-level variability model, perform the degree-1 calculation based on this model, and perform again five iterations. For another experiment 2, we start with ocean degree-1 coefficients set to zero in Swenson's method, use the derived first estimate of the global coefficients as input for the eustatic sea-level model estimation,

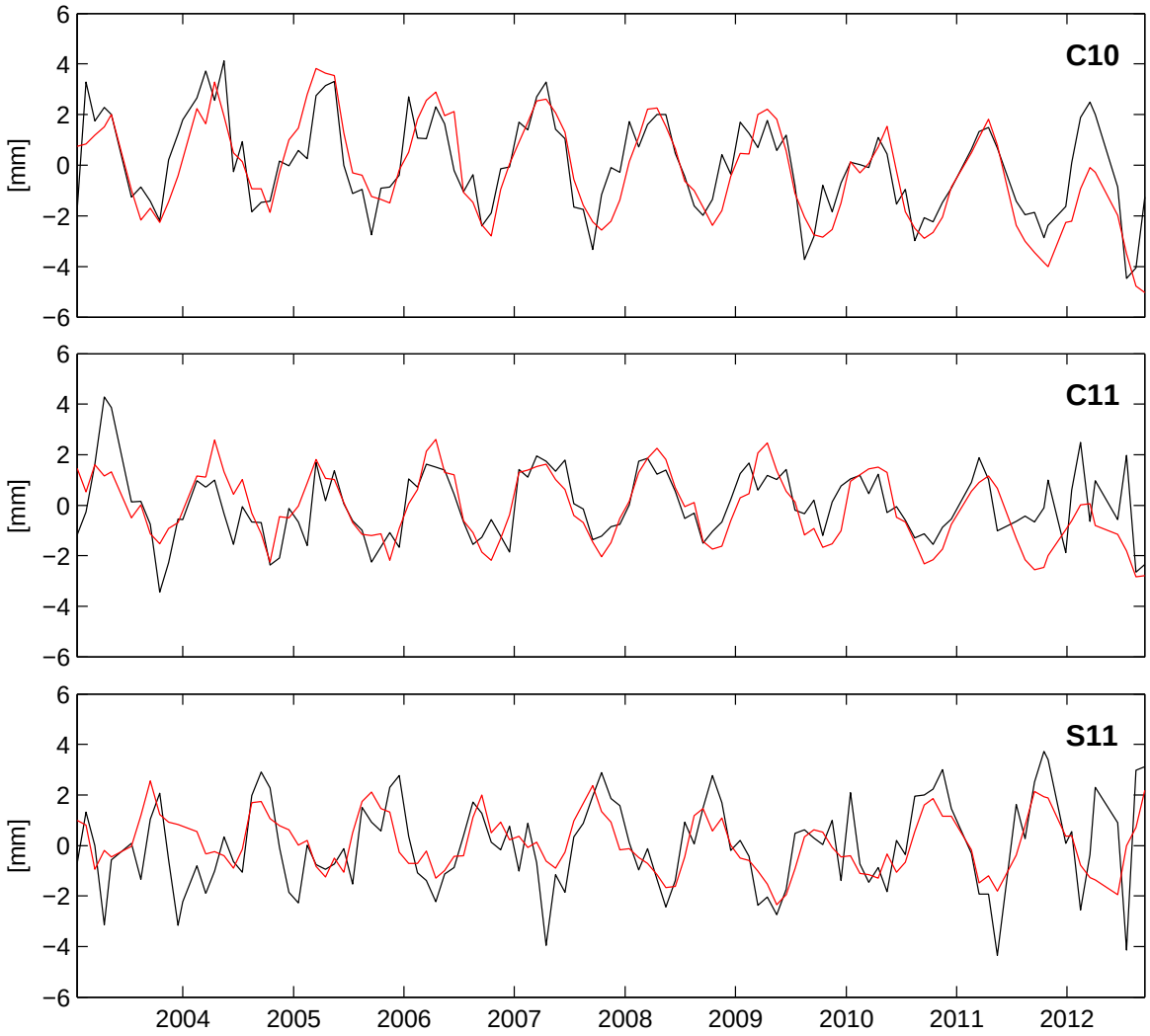

Figure 6.4: Estimated global geocenter variation time series from GFZ RL05 [black] with global ocean mass variations estimated with Gauss Filter for a filter radius of 300 km, and provided by the GRACE TELLUS webpage (http://grace.jpl.nasa.gov/data/degree1/) for the CSR RL05 solutions [red].

and iterate again for 5 times. For all three cases (reference as well as both experiments), increments decrease by approximately one order of magnitude per iteration, indicating that the initial assumption on the degree-1 terms introduced does not have a notable effect.

The final estimate of eustatic sea-level variability compares favorably with previously published results (Table 6.3). Amplitudes are slightly larger than early GRACE results from (Chambers, 2004), which might be explained by the fact that those early results have been obtained from the very first GRACE release with substantially higher error levels and therefore smoothing requirements. More recent calculations as published by (Wouters *et al.*, 2011)

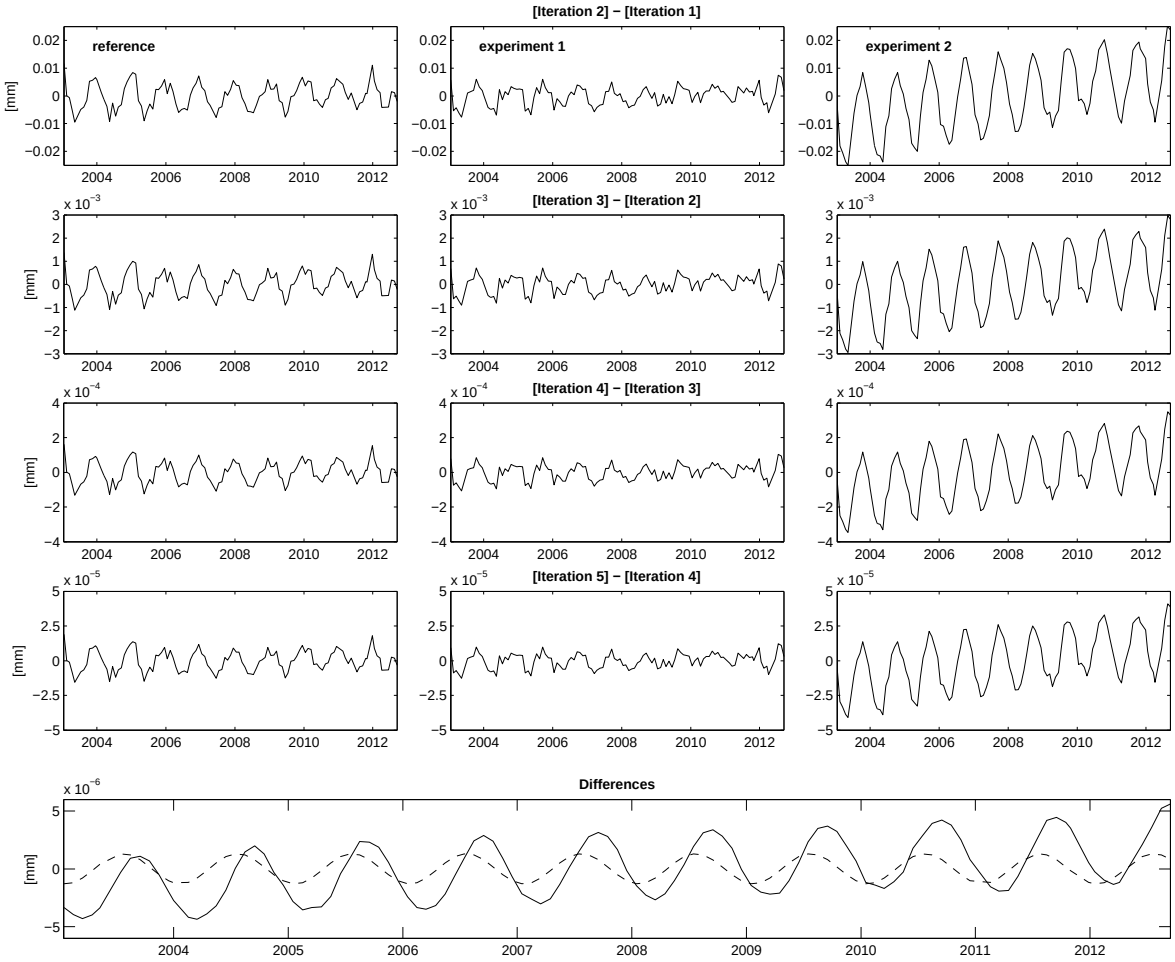

Figure 6.5: Increments in eustatic sea-level from the iterative determination of global degree-1 coefficients and a globally homogeneous eustatic sea-level variability model: starting from global degree-1 coefficients given by Eanes (2000) (reference, left column), starting from zero global degree-1 coefficients (experiment 1, middle), starting from zero eustatic sea-level anomaly (experiment 2, right). The bottom figure shows the difference of the time series after 5 iterations for reference minus experiment 1 [solid line] and reference minus experiment 2 [dashed line].

correspond quite closely to our results. Removing the seasonal cycle from the eustatic sea-level curve discloses for example the drop in sea-level in 2011 (Fig. 6.6), that has been related to record-high precipitation rates in Australia caused by La Nina teleconnections in the Central Pacific region (Fasullo *et al.*, 2013).

The obtained GSM-like degree-1 coefficients are finally compared to independent results from a joint inversion (Rietbroek *et al.*, 2012) (Fig. 6.7a). In general, we note higher short-term variability in the joint inversion, which is certainly due to the shorter time-sampling of only

Table 6.3: Annual amplitude and phase of global ocean mass variations.

	Amplitude [mm]	Phase [days]
a) final results after 5 iterations		
this study	9.78±0.54	278
b) other studies		
Chambers (2004)	8.40±1.1	266
Rietbroek *et al.* (2009)	8.70	247
Siegismund *et al.* (2011)	8.10	252
Wouters *et al.* (2011)	9.40	280
Hughes *et al.* (2012)	8.12	266

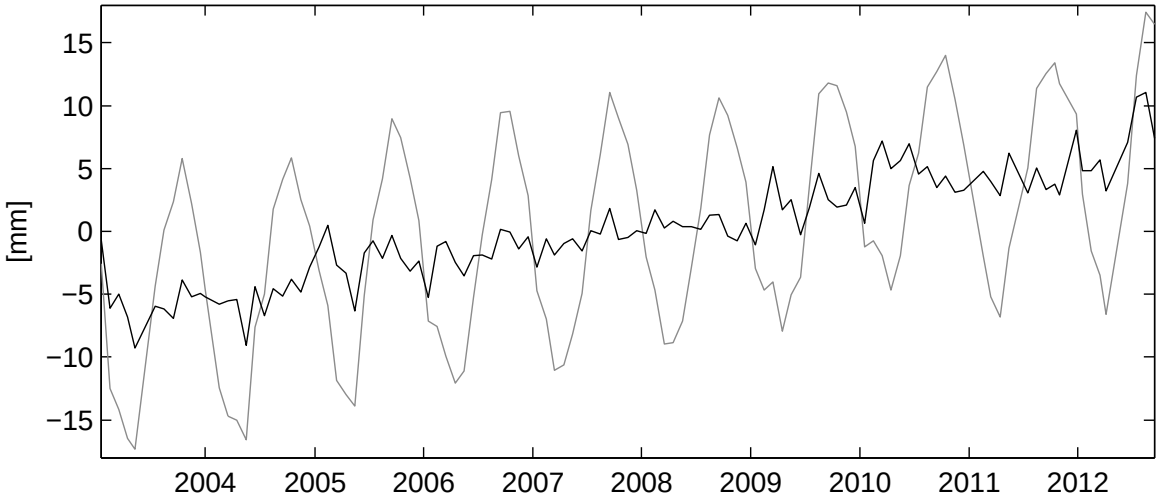

Figure 6.6: Final estimated global ocean mass variations after 5 iterations [gray], and global ocean mass variations after 5 iterations with the annual cycle removed [black].

seven days compared to the 30 day averages considered in this paper. It is however, interesting to note that the joint inversion apparently follows the AOD1B RL05 degree-1 coefficients quite closely (gray line in Fig. 6.7a), even though the product is stated to be GSM-like. For the full geocenter solutions, that are obtained in our case by adding the GSM-like solutions to AOD1B RL05 averages as provided with the GRACE gravity field by means of GAC products, this phase-shift between the two solutions is no longer visible. Here, geocenter motion as approximated by the method of Swenson corresponds well to the joint inversion, whereas a solution solely based on SLR observations deviates much stronger in particular in the ΔC_{10} and ΔC_{11} components.

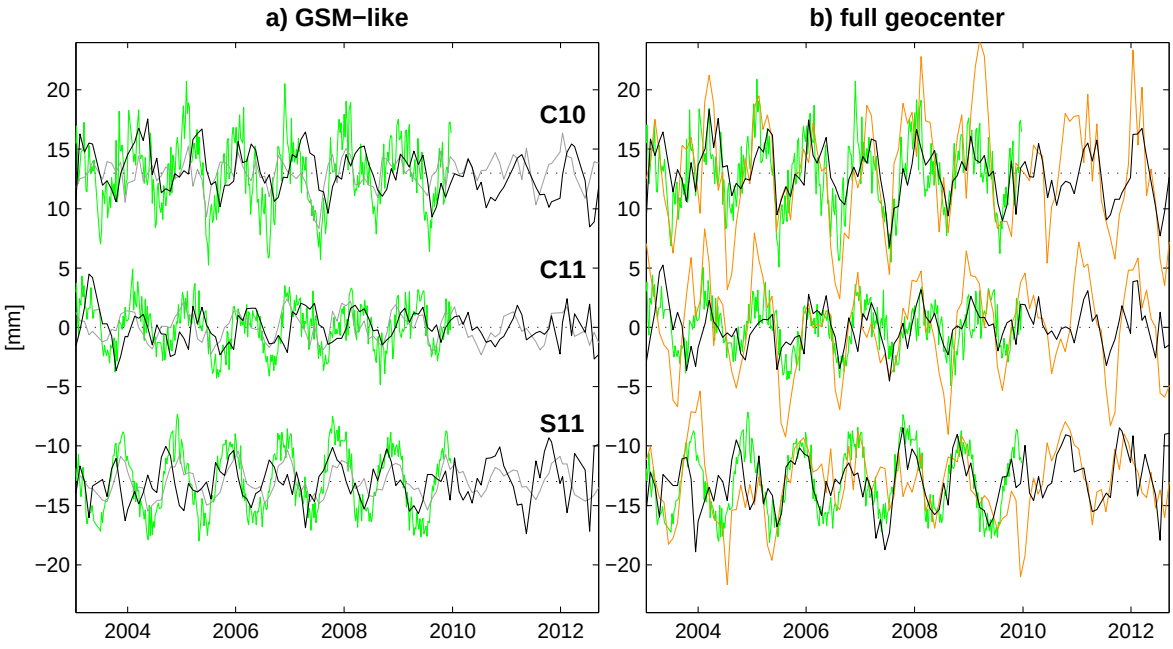

Figure 6.7: Left: GSM-like geocenter variations from GRACE with global ocean mass variations with Gauss Filter (300km, 5 iterations) [black], results from joint-inversion by Rietbroek *et al.* (2012) [green] and degree-1 terms of the RL05-GAC product [gray]. Right: full geocenter time series (RL05 GSM + GAC) from GRACE with global ocean mass variations estimated with Gauss Filter (300 km, 5 iterations) [black], geocenter variations from Satellite Laser Ranging measurements from Cheng *et al.* (2010) [orange] and results from joint-inversion by Rietbroek *et al.* (2012) [green].

6.1.6 Summary and conclusions

A methodology to approximate geocenter motion that was originally proposed by Swenson *et al.* (2008) essentially requires (i) a truncated series of global Stokes coefficients of degree two and higher, and (ii) degree-1 terms of the ocean bottom pressure variability. Since atmosphere and ocean dynamics are routinely removed from the GRACE gravity fields, global degree-1 terms consistent with the GRACE GSM fields should contain over the oceans only contributions from eustatic sea-level variability. By assuming that the eustatic sea-level change is globally homogeneous, such a model might be obtained from a truncated series of global Stokes coefficients of degree two and higher. Under those assumptions it is therefore possible to approximate GSM-like geocenter motion solely from GRACE monthly mean gravity fields.

Our implementation of the methodology of Swenson *et al.* (2008) has been thoroughly tested: experiments with a 12 year-long model series indicate that errors in the atmospheric part of the AOD1B that might potentially leak into the GSM fields can be safely neglected.

Table 6.4: Annual amplitude and phase of finally estimated GSM-like and full (GSM+GAC) geocenter variations.

	$\Delta C10$		$\Delta C11$		$\Delta S11$	
	[mm]	[days]	[mm]	[days]	[mm]	[days]
a) GSM-like coefficients						
this study	2.04±0.18	88	1.39±0.19	105	1.54±0.34	-84
Rietbroek *et al.* (2012)	3.01±0.37	20	1.94±0.14	63	3.47±0.11	-39
b) full geocenter coefficients						
this study	2.15±0.42	63	1.93±0.31	59	2.52±0.34	-45
Cheng *et al.* (2010)*	4.37±1.78	39	4.17±0.90	30	2.62±1.29	-39
Rietbroek *et al.* (2012)*	3.09±0.39	20	1.99±0.16	63	3.56±0.11	-38

*) The mean, trend and annual signal component has been fitted to the time series of Cheng *et al.* (2010) and Rietbroek *et al.* (2012) and the formal errors of the fits have been estimated.

Errors in the ocean component are potentially more severe, and affect in particular the ΔC_{11} component. Moreover, we note a sensitivity of the method to uncertainties in the eustatic sea-level model in particular for the ΔC_{10} and ΔC_{11} components. Initial assumptions on global degree-1 terms, however, are not important, since convergence is always reached after less than five iterations in every single test case considered.

The geocenter motion estimates from GRACE compare well to both GSM-like coefficients from a joint inversion and - after adding back the corresponding GAC field of monthly mean atmosphere and ocean mass variability removed during the gravity field processing by means of the AOD1B background model - to full geocenter estimates based on SLR. It is interesting to note that correspondence with SLR is generally best for ΔS_{11} (Table 6.4), the component that is less susceptible to errors in the eustatic sea-level model as shown in section 3. Also, the close correspondence of the GSM-like results of the joint inversion with the AOD1B-only geocenter estimates, especially in seasonal frequencies, might be worth to be analyzed in more detail in the future.

For regional oceanographic and hydrologic applications of GRACE satellite gravimetry fields, however, the generally good correspondence of the approximated geocenter motion estimates from GRACE with independent solutions let us conclude that this data-set is well suited to be used where otherwise an important part of the signals would be missed out. Since all information required for the algorithm is available from the GRACE archives, this would allow for another step towards a near real-time monitoring of mass distribution and transport in the Earth system by means of satellite gravimetry.

6.2 The impact of Loading and Self-Attraction on the determination of global ocean mass variations and geocenter motion

In the previous chapter, the eustatic contribution to Swenson's method has been defined as homogeneous distribution estimated from GRACE GSM-data. Therefore, effects of loading and self attraction (LSA) induced by mass redistributions at the surface have been neglected. These gravitational effects produce sea level pattern which are not homogeneously distributed throughout the globe (Clarke *et al.*, 2005; Tamisiea *et al.*, 2010). Especially, the study by Clarke *et al.* (2005) found significant changes in the annual estimates of geocenter motion when LSA-effects are taken into account. An improvement of up to 43% for the x-component (ΔC_{11}) has been achieved.
The explained variances of the test cases with the model data in the previous chapter showed an insufficient representation of the x-component when only the homogenous eustatic signal has been included in the method of Swenson *et al.* (2008). In the following, LSA effects will be included in the determination strategy.

6.2.1 Inclusion of Loading and Self-Attraction in the processing strategy of Swenson *et al.* (2008)

LSA-effects originate from the mass redistribution in the atmosphere, ocean and water stored on land. For the last component, the water is stored in rivers and soil and also as ice masses in glaciers and ice shields. The melting and mass input of glaciers and ice shields induce significant fingerprints in the sea level variations (Riva *et al.*, 2010; Wouters *et al.*, 2011; Jensen *et al.*, 2013). For the secular signal, Riva *et al.* (2010) found a global sea level rise of 1.0±0.4 mm/yr. Due to the increased melting of the Greenland and Antarctic ice shields, regions in the lower latitudes will experience a sea level increase of up to 20% more than the global mean which will be intensified by the seasonal relative sea level (RSL) changes in these regions due to hydrological variations. All continental stored water masses would lead to a global annual RSL amplitude of 9.4±0.6 mm/yr (Wouters *et al.*, 2011).

All masses which will be taken into account for the estimation of the LSA impact have to conserve the global mass. So the mass load of all known loads have to be balanced by the ocean (Tamisiea *et al.*, 2010). Therefore, the global average for each time step has been reduced from the fields. The atmospheric field is separated into two components. The first one is the loading impact over the continents. The second one, is the loading impact over

the oceans, which will react as an inverted barometer due to the above atmospheric pressure changes.
The final total mass load (ΔAL_{lm}) expressed in spherical harmonic coefficients will be:

$$\Delta AL_{lm} = \Delta H_{lm}(t_j) + \Delta ATM_{lm}(t_j) + \Delta OBP_{lm}(t_j) \tag{6.9}$$

whereas $\Delta H_{lm}(t_j)$, $\Delta ATM_{lm}(t_j)$ and $\Delta OBP_{lm}(t_j)$ describe the mass change in the continental water storage, in the atmosphere and the dynamical part of the ocean. The global averaged mass change ($\Delta S_{00}(t_j)$) is expressed by:

$$\Delta S_{00}(t_j) = -\Delta AL_{00}(t_j) = -(\Delta H_{lm}(t_j) + \Delta ATM_{lm}(t_j)). \tag{6.10}$$

The RSL-variations are estimated by solving the Sea-Level-Equation as given in chapter 2.1.2. The estimated fields are then analyzed in spherical harmonic coefficients. The degree-1 terms $[\Delta C_{10}^{RSL}, \Delta C_{11}^{RSL}, \Delta S_{11}^{RSL}]$ are used for the eustatic signal in Eq. (6.8):

$$\begin{bmatrix} \Delta C_{10}^{RSL} \\ \Delta C_{11}^{RSL} \\ \Delta S_{11}^{RSL} \end{bmatrix} = \begin{bmatrix} I_{10C}^{10C} & I_{11C}^{10C} & I_{11S}^{10C} \\ I_{10C}^{11C} & I_{11C}^{11C} & I_{11S}^{11C} \\ I_{10C}^{11S} & I_{11C}^{11S} & I_{11S}^{11S} \end{bmatrix} \begin{bmatrix} \Delta C_{10} \\ \Delta C_{11} \\ \Delta S_{11} \end{bmatrix} + \begin{bmatrix} G_{10C} \\ G_{11C} \\ G_{11S} \end{bmatrix} \tag{6.11}$$

6.2.2 Impact on ESA ESM data

In chapter 6.1, data of the updated ESA Earth System Model have been used to investigate the method of Swenson *et al.* (2008). As described in Chapter 5, the ocean mass variations are defined as inversely added mass variations of the atmosphere, hydrology and ice component. Therefore, the model has no information about the regional distribution of the global ocean mass variations and needs an adjustment. Firstly, the C_{00} coefficients of the ocean component have been set to zero. Afterwards, the SLE has been solved for the atmosphere, hydrology and ice component. The estimated relative sea level patterns were added in the spherical harmonic domain to the ocean coefficients. These data are used for the computation of the LSA-effects on the global ocean. The monthly annual amplitude and phase of the RSL-fields are shown in Fig. 6.8. The global average annual amplitude is 10.68 mm with a phase of 250°. This is more than 1 mm larger than previous estimates by i.e. Tamisiea *et al.* (2010). Amplitudes higher than the global average are found in the lower latitudes, e.g. at the west and east coast of Africa and the southern coast of Asia adjacent to the Indian ocean. The phase of the mean annual RSL pattern is mainly affected by the ocean model component.
The new degree-1 terms including the RSL-pattern are shown in Fig. 6.9 together with the

Table 6.5: Relative explained variance in [%] for the recovery of global degree-1 coefficients from TEST3 for the case of homogeneous distributed eustatic signal and estimated as RSL variations.

	ΔC_{10}	ΔC_{11}	ΔS_{11}
homog. eustatic SL	73.47	45.12	79.75
RSL (0km)	96.28	84.69	96.07
RSL (300km)	94.94	87.20	86.94

Table 6.6: Annual amplitude and phase of estimated geocenter variations from AOHI coefficients.

	$\Delta C10$		$\Delta C11$		$\Delta S11$	
	[mm]	[days]	[mm]	[days]	[mm]	[days]
orig. AOHI + LSA (AHI)	3.31±0.44	48	3.09±0.12	47	2.86±0.14	-34
homog. eustatic SL	1.70±0.10	44	1.06±0.05	80	1.76±0.05	-42
RSL (0km)	2.86±0.37	54	2.36±0.11	66	2.88±0.15	-42
RSL (300km)	3.28±0.54	53	2.69±0.14	65	3.43±0.22	-46

original degree-1 terms for the AOHI product (atmosphere (A), ocean (O), continental water storage (H) and ice masses (I)) and the estimated coefficients from TEST 3 (see chapter 6.1.3) but this time with the atmospheric component included. Significant differences are observable for all three components whereas the largest improvements have been made for ΔC_{11}. The relative explained variance has been improved up to 84.69 %. An improvement has also been achieved for ΔC_{10} (96.28 %) and ΔS_{11} (96.07 %) (Table 6.5). The phase shift in ΔC_{11} has been reduced by 14 days (Table 6.6). The annual amplitudes of all three coefficients are closer to the original time series.

Additionally, the degree 1 terms were estimated with a land water mask excluding the coastal zone of 300 km. This has been done to assess the impact of the coastal area in the processing strategy when using GRACE data, where these signals are omitted due to land leakage effects. Introduction of the buffer zone leads to an improvement of the ΔC_{11} coefficient. The relative explained variances for the other two components are slightly lower than without the buffer zone but still around 90%. The phase shift in ΔC_{11} has been reduced by 15 days. So the phase difference to the original model time series is now smaller than a month compared to the results with the homogeneous distribution of the eustatic signal.

By application of the coastal buffer, large annual amplitudes of RLS variations in the Indian Ocean (20 mm) and small RSL variations (1-4 mm) in postglacial regions, like Hudson Bay,

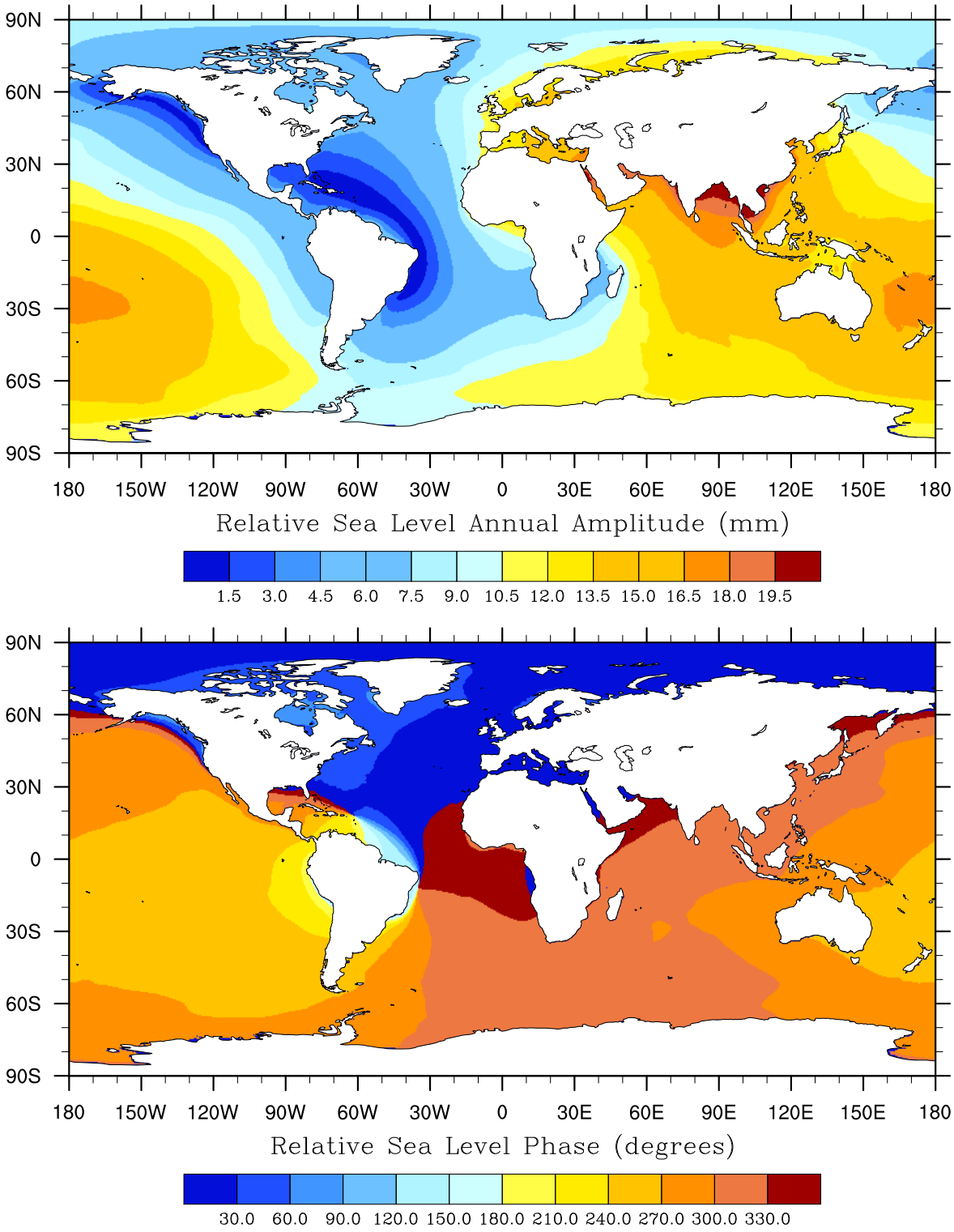

Figure 6.8: Annual amplitude [top] and phase [bottom] of the relative sea level caused by loading of atmosphere, hydrology, ice and dynamical ocean variations.

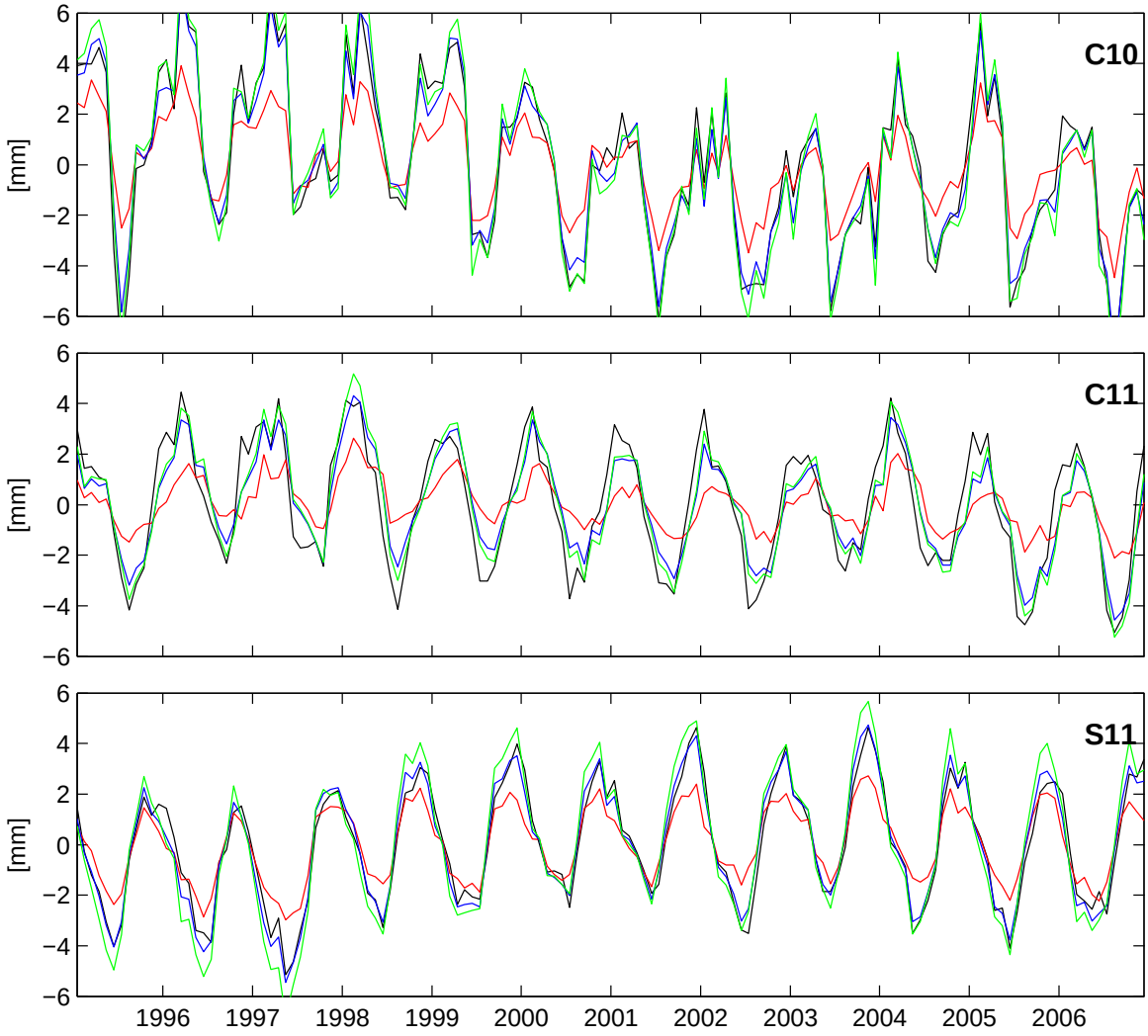

Figure 6.9: Recovery of global geocenter variations from TEST 3 in Sec. 6.1.3: true model time series of AOHI + LSA (A,H,I) [black], estimated with homogeneous sea level assumption [red], with RSL variations [blue] and with RSL variations and coastal buffer zone of 300km [green].

are omitted in the determination process. The test with the model data shows that ΔC_{11} is sensitive to the coastal signals in RSL variations.

6.2.3 Impact on GRACE RL05 data

In the next step, the degree-1 terms have been re-estimated from the GRACE coefficients. The load signal is composed of the GAA product for the atmospheric part, the GSM coefficients filtered with the DDK3 filter and synthesized for the continental parts for the hydrological component and the GSM+GAD coefficients filtered with the DDK1 filter and synthesized for the ocean region for the oceanic component. Additionally, each component has been reprocessed as described in Section 6.2.1. The determination process starts without information of the global degree-1 coefficients (see experiment 1 in Section 6.1). The RSL pattern have been determined from the GRACE data and included in the determination process according to Eq. (6.11). The processing has been iterated for 5 times. The hydrologic and oceanic components were recomputed for each iteration step including the newly determined degree-1 coefficients.
The annual amplitude and phase of the RSL field for no degree-1 terms included and after five iterations are shown in Fig. 6.10. Significant differences in the annual amplitude pattern are observed along the coasts of middle America, in the Indian Ocean and the Pacific Ocean at the southern hemisphere. Including degree-1 terms lead to a decrease in RSL change in the former region of the Laurentide ice sheet. This also causes a significant change in the annual phase of 270 days. Contrary, an increase in annual RSL is observed in the complete Indian Ocean, the adjacent Southern Ocean and nearly 80% of the Pacific Ocean on the southern hemisphere. The phase shift in this region is not larger than +/-15 days.

The new estimates of global ocean mass variations including LSA effects are shown in Fig. 6.11 together with the results of the previous chapter after 5 iterations. Both time series are close to each other. The annual amplitude of the new results has been decreased by 0.52 mm to 9.26±0.62 mm whereas the annual phase remains nearly stable at 276 days. This leads to the conclusion, that the main feature of global ocean mass variations is given when using degree-1 coefficients estimated with a homogeneous distribution of the eustatic signal whereas the annual signal is affected by the regional pattern of the RSL field due to LSA effects.

The final degree-1 coefficients are shown together with the results from experiment 1 without LSA in Figure 6.12, which are very similar. Including the LSA signal leads to more temporal variability of the estimated geocenter variations. Largest differences are observed for ΔS_{11}. In Table 6.7 the annual amplitude and phase of the GSM-like and full geocenter variations

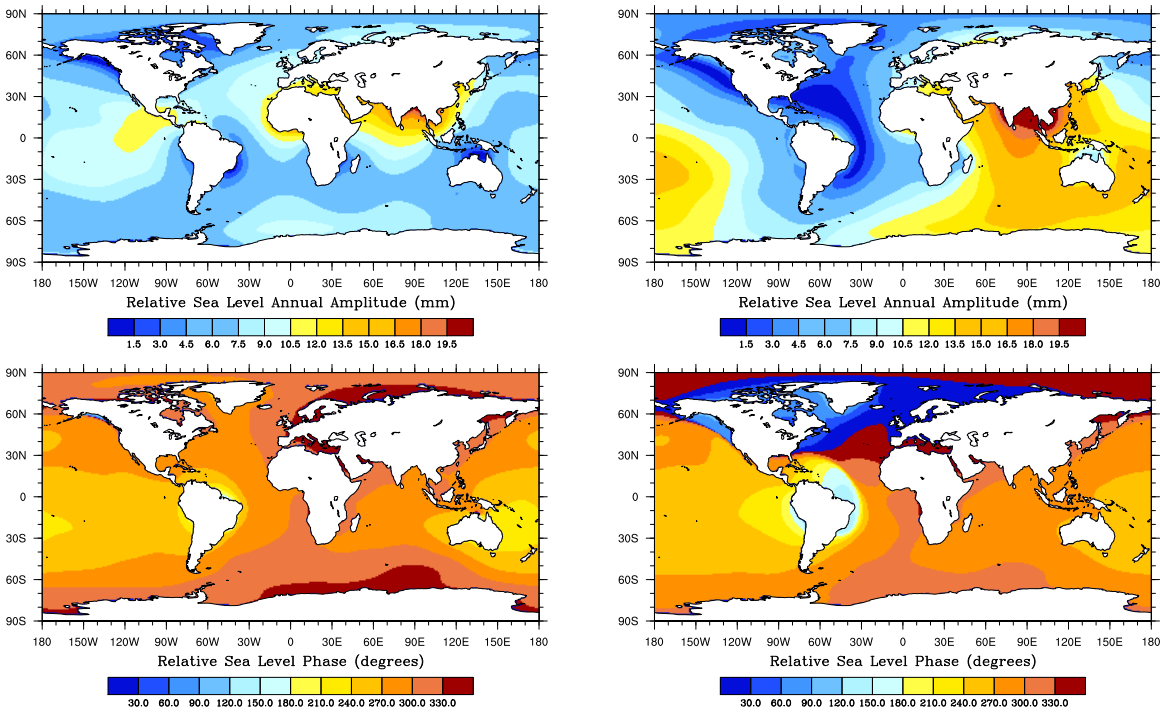

Figure 6.10: Annual amplitude [top] and phase [bottom] of the relative sea level caused by loading of atmosphere, hydrology, ice and dynamical ocean variations from GSM data without d1-terms [left column] and with estimated d1-terms after 5 iterations [right column].

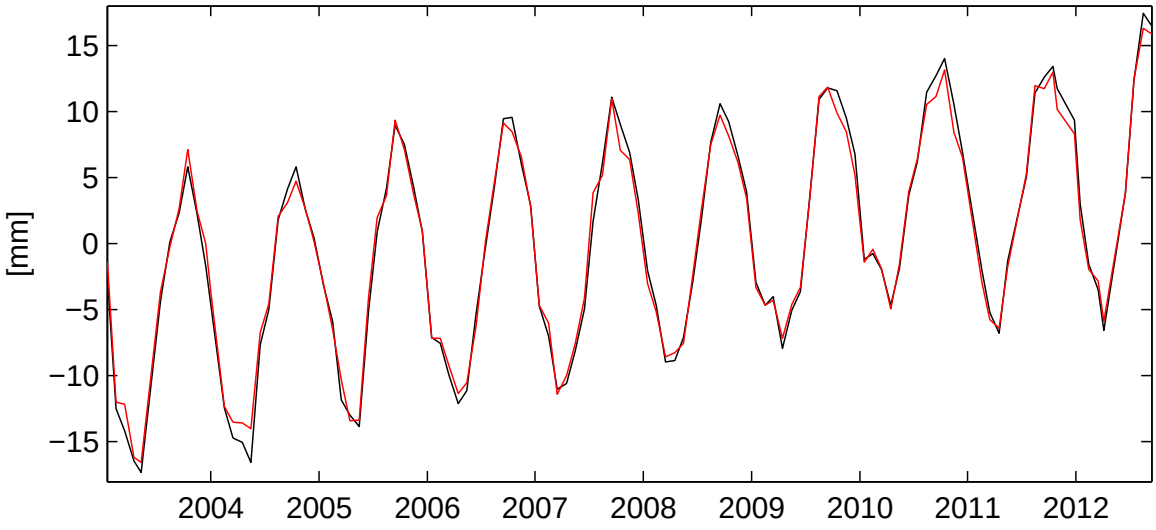

Figure 6.11: Final estimated global ocean mass variations after 5 iterations [black] and estimated with RSL-variations [red].

Table 6.7: Annual amplitude and phase of finally estimated GSM-like and full (GSM+GAC) geocenter variations with and without LSA effects.

	$\Delta C10$		$\Delta C11$		$\Delta S11$	
	[mm]	[days]	[mm]	[days]	[mm]	[days]
a) GSM-like coefficients						
homog. eust. signal	2.04±0.18	88	1.39±0.19	105	1.54±0.34	-84
RSL (300km)	1.86±0.28	90	1.24±0.28	98	2.06±0.46	-76
Rietbroek *et al.* (2012)	3.01±0.37	20	1.94±0.14	63	3.47±0.11	-39
b) full geocenter coefficients						
homog. eust. signal	2.15±0.42	63	1.93±0.31	59	2.52±0.34	-45
RSL (300km)	2.00±0.64	62	1.96±0.44	53	3.10±0.48	-48
Rietbroek *et al.* (2012)	3.09±0.39	20	1.99±0.16	63	3.56±0.11	-38

are given together with the results of section 6.1.5 and estimates of Rietbroek *et al.* (2012) because best temporal agreement were seen with these results. The annual amplitude of the GSM-like ΔC_{10} and ΔC_{11} are decreased by 0.18 mm and 0.15 mm whereas for ΔS_{11} an increase of 0.52 mm is observed. Also the largest phase shift is shown for ΔS_{11} of 8 days. For the fully geocenter variations ΔC_{11} and ΔS_{11} are now closer to the joint inversion results. The formal error budget of the degree-1 coefficients estimated with LSA effects is larger than with the homogeneous distribution of global ocean mass variations due to the regional variations of the global ocean mass signal.

6.2.4 Final conclusions

The extension of the described processing strategy in Chapter 6.1 by taking effects of Loading and Self-Attraction into account lead to slightly different results of degree-1 terms as when just approximating a homogeneous distribution of global ocean mass. The test with the model data has shown, that the ΔC_{11} term is definitely improved when using RSL pattern for the ocean signal in the processing and that the coastal signals influence the results, too. Unfortunately, this large differences could not be observed when using the GRACE data and larger changes were seen for ΔS_{11} than for ΔC_{11}. Nevertheless, the annual phase of ΔC_{11} and ΔS_{11} has been shifted by -8 days and is closer to the results of Rietbroek *et al.* (2012). This phase shift is a result of including LSA effects into the computation of the degree-1 coefficients by the method of Swenson *et al.* (2008) as the test with the ESA ESM model data have shown and therefore indicating an improvement in the geocenter results determined solely from GRACE data.

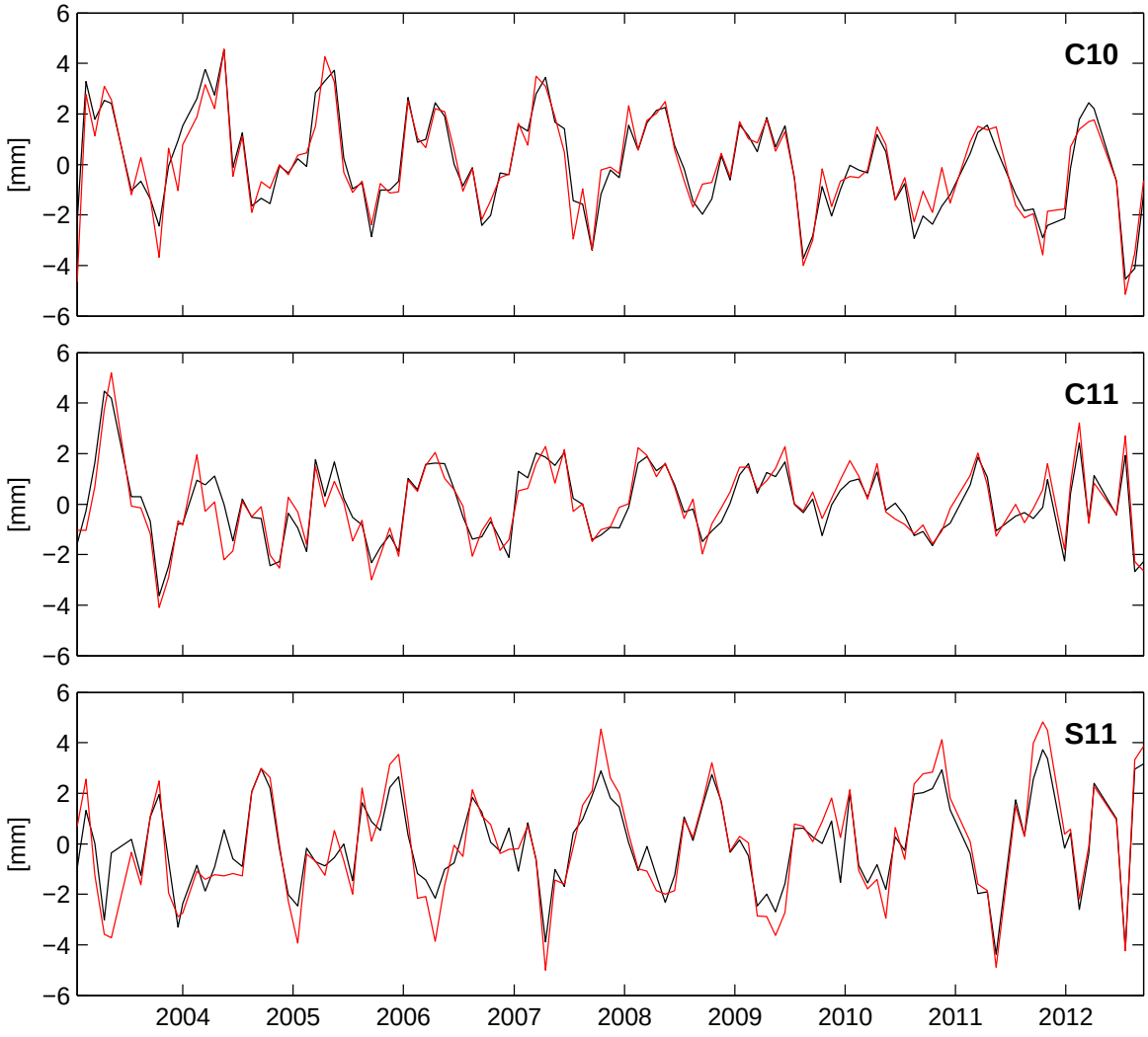

Figure 6.12: GSM-like geocenter variations from GRACE with global ocean mass variations with Gauss Filter (300km, 5 iterations) [black] and additionally added with RSL-variations [red].

Chapter 7

Regional ocean bottom pressure variability in response to atmospheric forces

The sea level is regionally different and shows complex patterns which are substantially different from the global average. Regional variations arise from ocean dynamics, movement of the sea floor and gravity variations due to mass redistributions (Church *et al.*, 2013). For the latter one, in Chapter 6.2 relative sea level variations due to LSA effects have been shown. Natural and anthropogenic climate modes have an influence on the spatial patterns and include processes like the dynamical redistribution of water masses and change in temperature or salinity due to changes in wind, air pressure, air-sea heat, freshwater fluxes and ocean currents. Climate modes describe the climate variability in a specific region by means of spatial patterns and temporal variability, which define the main features of the phenomena (Christensen *et al.*, 2013). In Tab. 7.1, some modes for the Northern and Southern Hemisphere which have a large impact on the hemispherical climate are given.

Regional sea level trends estimated from altimetry data[1] and ocean mass variations as OBP from GRACE (CSR RL05[2]) show large values up to 12 mm/yr in the western Pacific region (see Fig. 7.1). These are caused by the intensification of the trade winds and are most likely related to the Pacific Decadal Oscillation (PDO) (Merrifield *et al.*, 2012). The decrease in

[1] MSL from TPOPEX/Poseidon, Jason-1 and Jason-2 for the Period 01/1993-07/2014, available at www.aviso.altimetry.fr/en/data/products/ocean-indicators-produtcs/mean-sea-level/products-images.html

[2] Gridded data available at ftp://podaac-ftp.jpl.nasa.gov/allData/tellus/L3/ocean_mass/RL05/netcdf/

Table 7.1: Climate Modes and their regional impact (excerpt from Box 14.1 Table 1 in Christensen *et al.* (2013))

Mode	Full Name	Regional Climate Impacts
ENSO	El Niño-Southern Oscillation	global impact on interannual variability in global mean temperature; present different teleconnection patterns that induce large impacts in numerous regions from polar to tropical latitudes
AMO	Atlantic Multi-Decadal Oscillation	influences air temperature and rainfall over Northern Hemisphere
NAO	North Atlantic Oscillation	influences North Atlantic jet stream, storm track and blocking, affects winter climate over North Atlantic
PDO	Pacific Decadal Oscillation	influences surface air temperature and precipitation over the entire North American continent and extratropical North Pacific; modulates ENSO rainfall teleconnections
NAM	Northern Annular Mode	modulates intensity of mid-latitude storms throughout Northern Hemisphere, influences North America and Eurasien climate, influence sea ice distribution across Arctic Sea
SAM	Southern Annular Mode	influences temperature over Antarctica, Australia, Argentina, Tasmania and south of New Zealand; affects precipitation over southern South America, New Zealand, Tasmania, Australia and South Africa

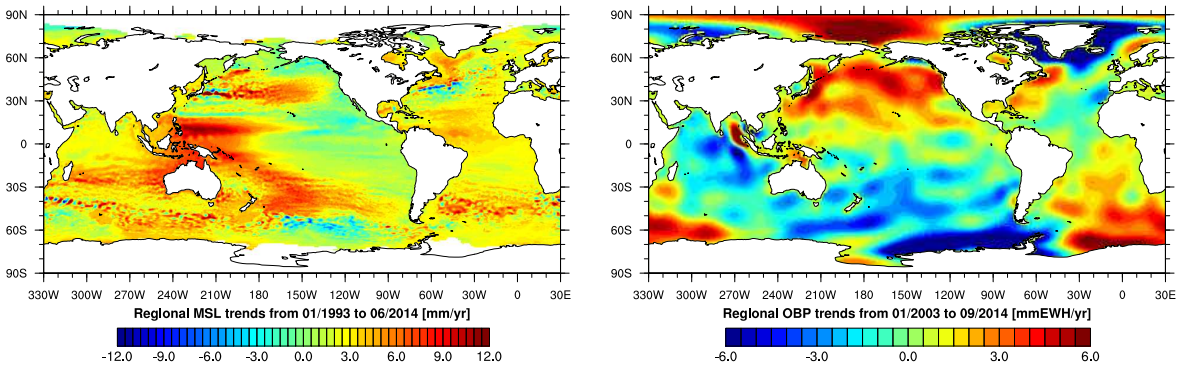

Figure 7.1: Regional trend field of (left) MSL from altimetry data (TOPEX/Poseidon, Jason-1, Jason-2) and (right) ocean bottom pressure from CSR RL05.

MSL at the west coast of the USA and increase in North Pacific are also associated with changes in the wind stress curl over the subpolar and subtropical gyres which can be related also to the PDO but also to other climate phenomena like the El Niño Southern Oscillation (ENSO) or the Northern Annular Mode (NAM) (Chambers, 2011; Petrick *et al.*, 2014). The positive trend in the North Pacific is also seen in the trend of ocean bottom pressure anomalies estimated from GRACE. A relation of OBP variations to the overlying changes in wind stress curl has been found by Bingham & Hughes (2006) whereas Song & Zlotnicki (2008) and Chambers & Willis (2008) showed the relation to the El Niño phenomena by comparison of modeled and GRACE based OBP time series with steric corrected altimetry data and the Multivariate ENSO index. The OBP anomalies in a region in the North Pacific (40-45°N, 200-180°W) were lower after a peak in El Niño warming and higher before a peak in El Niño warming relatively to the other years.

According to Ch. 2.2.1, geostrophic currents are induced by the approximative balance of horizontal pressure gradients and Coriolis force. For nearly barotropic geostrophic currents OBP variations are only induced by changes in the sea level height. From gradients of OBP observations barotropic mass transport variations are determined. On the southern hemisphere a huge amount of water masses are transported by the Antarctic Circumpolar Current (ACC) which is mainly forced by the wind. Due to strengthening of the southern hemisphere westerlies and the multi-decadal warming in the Southern Ocean, a poleward displacement of the ACC of 1° in 40 years has been detected (Gille, 2008). This will bring warmer water closer to the Antarctic ice shelf and will potentially contribute to melting of the ice shelf and induce local sea level rise.

7.1 Short-term transport variability of the Antarctic Circumpolar Current from satellite gravity observations

Published as: Bergmann, I. and Dobslaw, H., 2012: Short-term transport variability of the Antarctic Circumplar Current from satellite gravity observations, Journal of Geophysical Research, 117 (C05044) , doi:10.1029/2012JC007872.

Abstract: Ocean bottom pressure gradients deduced from the satellite gravity mission GRACE were previously shown to provide barotropic transport variations of the Antarctic Circumpolar Current (ACC) with up to monthly resolution. Here, bottom pressure distributions from GRACE with monthly (GFZ RL04) and higher temporal resolution (CNES/GRGS with 10 days, ITG-GRACE2010 with daily resolution) are evaluated over the ACC area. Even on time-scales shorter than 10 days, correlations with in-situ bottom pressure records frequently exceed 0.6 with positive explained variances, giving evidence that high frequency non-tidal ocean mass variability is captured by the daily ITG-GRACE2010 solutions which was not already included in the applied background models.

Bottom pressure is subsequently taken to calculate the barotropic component of the ACC transport variability across Drake Passage. For periods longer than 30 days, transport shows high correlations between 0.4 and 0.5 with several tide gauge records along the coast of Antarctica. Still significant correlations around 0.25 are obtained even for variability with periods shorter than 10 days.

Since transport variations are predominantly affected by time-variable surface winds, GRACE-based transports are contrasted against an atmospheric index of the Southern Annular Mode (SAM), which represents the southern hemispherically wind variability. Correlations between the SAM and GRACE-based transports are consistently higher than correlations with any of the available sea-level records in all frequency bands considered, indicating that GRACE is indeed able to accurately observe a hemispherically consistent pattern of bottom pressure (and hence ACC transport) variability, that is otherwise at least partially masked in tide gauge records due to local weather effects, sea-ice presence and steric signals.

7.1.1 Introduction

Strong westerly winds and the absence of land barriers in the middle latitudes of the Southern Hemisphere allow for the establishment of the Antarctic Circumpolar Current (ACC). Being the dominant feature of global ocean dynamics in terms of transport, it carries in average 136±11 Sv (Cunningham *et al.*, 2003) through Drake Passage into the South Atlantic. By

connecting all major ocean basins, the ACC permits the existence of a global overturning circulation allowing for the global exchange of freshwater, heat, nutrients, and other oceanic tracers that affect the evolution of the climate on our planet.

While the time-mean ACC transport is related to the interplay of various dynamic processes including topographic and eddy-induced stresses as well as stratification (see, e.g., Rintoul *et al.*, 2001; Olbers *et al.*, 2004, for a review), fluctuations in the southern hemispheric wind field are primarily responsible for variations of the transport in time. Based on theoretical argumentation and numerical experiments, Hughes *et al.* (1999) explain that topographically modified barotropic Rossby waves, resonantly excited by the varying winds, mediate the response along f/H-contours passing through the Drake Passage and encircling the continent, and lead to coherent variations in meridional bottom pressure gradients all around Antarctica. For reasons of geostrophy, pressure changes are more pronounced along the southern rim of the current, implying that bottom pressure sensors and sea-level gauges close to the Antarctic coast are suitable to monitor the barotropic component of the ACC transport variations (e.g., Woodworth *et al.*, 2006). In addition, numerical model experiments by Olbers & Lettmann (2007) indicate that correlations between bottom pressure changes and ACC transport remain strong for synoptic and annual time-scales, with baroclinic processes gradually gaining importance on decadal periods and longer. Thus, measurements of bottom pressure gradients around Antarctica are a valuable observable to monitor the transient variations of ACC mass transports, particularly on time-scales beyond a few years.

The ACC is driven by the surface winds. Whether its forcing is dominated by the wind stress via an Ekman-type mechanism, or the wind stress curl by means of a time-variable Sverdrup-type vorticity balance still remains controversial (e.g., Hughes *et al.*, 1999; Gille *et al.*, 2001). However, the ACC transports may be assumed to vary in response to changes in the Southern Annular Mode (SAM; Thompson & Wallace, 2000). This mode, excited internally within the mid-latitude's troposphere, is characterized by zonally symmetric atmospheric mass-shifts between polar and moderate latitudes and associated vacillations in the surface wind fields. The mode explains up to 30% of the de-seasonalized variability in both geopotential and winds. Antarctic sea-level variations, and thus ACC transport, were found to be correlated to the SAM down to seasonal time-scales (Meredith, 2004), although Cunningham & Pavic (2007) concluded that SAM-related modes cannot be detected in surface currents derived from repeated hydrographic sections and 12 years of satellite altimeter observations. Moreover, SAM variability can be characterized by a normally distributed red-noise process with an e-folding time-scale of 10 days, implying that substantial variability of the SAM is found even on a week-to-week basis, which might potentially be related to short-term variability

present in both bottom pressure and current meter observations in the Southern Ocean (see, e.g., Whitworth III & Peterson, 1985).

By mapping temporal variations of the Earth's gravity field, the Gravity Recovery and Climate Experiment (GRACE; Tapley, 2004) satellite mission provides for the first time an opportunity to observe changes in the global ocean bottom pressure distribution covering synoptic to inter-annual time-scales. Seasonal variations in regional bottom pressure from GRACE have been shown to be consistent with prevailing winds in the North Pacific (Bingham & Hughes, 2006), in-situ observations from deep-sea ocean bottom pressure sensors (Rietbroek *et al.*, 2006; Park *et al.*, 2008) as well as sterically corrected satellite altimetry and predictions from ocean general circulation models (Dobslaw & Thomas, 2007). By utilizing the relation between bottom pressure gradients and ACC transport variations, Zlotnicki *et al.* (2007) derived seasonal variations in ACC transport variability from early GRACE data-sets, and compared them to predictions from numerical ocean models. While Böning *et al.* (2010) confirmed their general conclusions based on reprocessed GRACE data, their results were as well restricted to a temporal resolution of 30 days.

Besides improvements in the overall accuracy of the GRACE gravity fields, progress has been also made in achieving a higher temporal resolution. In this paper, two alternative GRACE products with daily and 10 day sampling will be therefore tested for their ability to accurately represent ocean bottom pressure gradients and therefore transport in the Southern Ocean. Data sets and necessarily applied post-processing procedures are described in section 7.1.2. Bottom pressure variability as seen by these GRACE products is validated with respect to in-situ bottom pressure observations. Analysis is separated into three different intraseasonal frequency bands in order to allow an inter-comparison of these differently sampled GRACE time-series (section 7.1.3). The relation of bottom pressure gradients in the southern Pacific with transport variations in Drake Passage and sea-level variability around Antarctica is demonstrated by means of an ocean model simulation (section 7.1.4) in order to discuss the suitability of those variables to predict ACC transports on different timescales. Transport variations as derived from different GRACE products are subsequently evaluated by means of sea-level variability from coastal tide gauge observations around Antarctica (section 7.1.5) and an index for the Southern Annular Mode (section 7.1.6), followed by some concluding remarks in the final section.

7.1.2 Estimating ocean bottom pressure variations from GRACE gravity fields

The twin-satellite mission GRACE has been specifically designed to map spatio-temporal variations of the Earth's gravity field. The mission aims at a nominal accuracy of ∼1 mm geoid height on regional scales of around 500 km and a temporal resolution of one month (Tapley, 2004). Primary observables are highly accurate distances and relative velocities between the two spacecrafts obtained from a microwave ranging system, accompanied by accelerometer data to separate non-gravitational forces, as well as GPS and star camera observations for position and attitude control of the satellites.

The standard methodology of the main processing institutions Center for Space Research at the University of Texas (CSR), Jet Propulsion Laboratory (JPL) and Deutsches GeoForschungsZentrum (GFZ) uses data for a period of about 30 days to determine monthly solutions. To reduce non-tidal variations in atmosphere and ocean, the AOD1B RL04 products (Flechtner, 2007) are applied. These background models consist of atmospheric mass anomalies from the ECMWF operational data and mass anomalies from the global ocean circulation model OMCT (Thomas *et al.*, 2001), driven by corresponding ECMWF atmospheric fields. Stokes coefficients (Wahr *et al.*, 1998) are provided up to spherical harmonic degree/order (d/o) 120. In this paper, we use monthly gravity field solutions of the latest release 04 from GFZ (Schmidt *et al.*, 2008) covering the time period of 02/2003 to 08/2009.

Other scientific institutions use different processing strategies to calculate global gravity fields with higher temporal resolution. CNES/GRGS (Centre National d'Etudes Spatiales/Groupe de Recherches de Géodésie Spatiale) determines 10-day gravity field solutions up to d/o 50 (Bruinsma *et al.*, 2010). CNES/GRGS solves stacked 10-day normal equations with additional constraints based on the formal covariances of the coefficients. Due to a degree and order dependent stabilization matrix, each coefficient's noise is reduced individually between d/o 16-36 which leads to a greater signal contribution in the higher degrees. Instead of OMCT, the barotropic MOG2D ocean model (Carrere & Lyard, 2003) is applied at CNES/GRGS to reduce non-tidal ocean variability. Seven years of 10-day gravity field solutions of the most recent release 02 for a time period of 08/2002 to 08/2009 are used in our study.

Improving the temporal resolution by reducing the time-span of observations that enter into a single solution necessarily decreases the spatial resolution, since a smaller number of gravity field parameters can be solved for in a least-squares adjustment process. To overcome this problem, the University of Bonn introduced a new approach to estimate daily gravity

field solutions, ITG-GRACE2010 (Institute for Theoretical Geodesy), by means of a Kalman Smoother (Kurtenbach *et al.*, 2009). Assuming that the gravity field parameters of the current day are correlated to (and thus predictable from) the previous one's, a first order Markov process can be described. Empirical signal covariances characterizing the expected changes of the fields have been derived from multi-year time-series of geophysical models describing variability in atmosphere, ocean and continental hydrosphere. AOD1B RL04 has been applied to reduce the short-term non-tidal variations of the gravity field as well (Kurtenbach, 2011). The daily gravity field solutions are estimated up to d/o 40.

Changes in ocean bottom pressure represent the summarized effect of mass changes within the above-lying ocean and atmosphere. Since these signals have been at best fully removed during processing by applying the de-aliasing product as background model, its time averaged field (i.e., the GAC product for the combined effect of atmosphere and ocean in GRACE terminology) must be added back to restore the signal. Additionally, degree 1 terms, which represent variations of the center-of-mass with respect to a terrestrial reference frame, are required from auxiliary sources. A mean annual sinusoid determined from Satellite Laser Ranging and DORIS observations (Eanes, 2000) has been applied here.

Since we are interested in changes of oceanic mass, spectral leakage of continental signals is minimized following Wahr *et al.* (1998). In addition, meridional striations occur in the solutions due to inherent properties of the GRACE observation geometry. These effects can be reduced by d/o-dependent spatial filtering of the Stokes coefficients with a non-isotropic two-point kernel function (Kusche, 2007), which works in the same way as a Tikhonov-type regularization of the normal equation system. By taking an approximation of the error covariance matrix from GRACE and an a priori signal covariance matrix into account, the north-south correlations of the field are removed. This anisotropic decorrelation filter was only applied to the monthly GFZ gravity field solutions. Due to additional constraints applied during processing of both the CNES/GRGS (regularization) and the ITG-GRACE2010 solutions (Kalman smoother), an additional filtering of these products is not appropriate.

Stokes coefficients $\Delta C_{lm}, \Delta S_{lm}$ from GRACE for a given time epoch t are finally transformed into bottom pressure anomalies according to Wahr *et al.* (1998)

$$\Delta p_{bot}(\phi, \lambda, t) = \frac{a_E g \rho_E}{3} \sum_{l=1}^{N} \sum_{m=0}^{l} \frac{2l+1}{1+k_l} P_{lm}(\sin\phi) \times \{\Delta C_{lm} \cos m\lambda + \Delta S_{lm} \sin m\lambda\} \qquad (7.1)$$

with a_E the semi major axis, ρ_E the Earth's mean density, g the mean gravitational acceleration, k_l are the Love numbers of degree l, P_{lm} the normalized associated Legendre functions of degree l and order m, ϕ is the geographical latitude, λ the geographical longitude.

7.1.3 In-situ ocean bottom pressure

In order to validate bottom pressure variability as seen by GRACE, we use in-situ observations from a number of ocean bottom pressure (OBP) recorders. Globally distributed data-sets obtained by various institutions were made available by Macrander *et al.* (2010). The provided data is quality controlled (i.e., elimination of outliers), instrumental drift was removed by a quadratic fit, and tides have been separated by means of the FES2004 tide model (Lyard *et al.*, 2006). Time-series from 21 stations in the Southern Ocean are used in this study (Fig. 7.2). Regional bottom pressure averages from GRACE comparable to these time-series have been obtained by applying a pattern filter (Böning *et al.*, 2008). For this, correlations between ocean bottom pressure anomalies in a maximum radius of 20° have been estimated with model time-series from OMCT. Afterwards, GRACE data have been filtered by weighting points within the 20° circle with their correlations higher than 0.7 and an additional cut-off function starting at a distance of 18°.

To analyse signals in different frequency bands, filtering of in-situ and GRACE bottom pressure time-series is required. While smaller gaps have been interpolated for the filtering and flagged as missing values again afterwards, gaps of more than 30 days effectively split the record into sub-samples that have been treated individually in terms of estimating and removing trends as well as annual and semi-annual components. While the GFZ RL04 time-series with its monthly sampling was not filtered further, all daily time-series have been filtered with a Butterworth filter of order 3, with cut-off periods of 10 and 30 days. Signals are therefore separated into three different frequency bands: (a) periods longer than 30 days (30-days low pass filter), (b) periods between 10 and 30 days (10-to-30-days band pass filter), and (c) shorter than 10 days (10-days high pass filter). The 10-day CNES/GRGS RL02 solutions have only been filtered with the 30-days low pass filter and afterwards separated into the first two frequency bands, (a) and (b). All subsequent analyses in this paper will refer to a separation of the signals into these three frequency bands.

For periods above 30 days, correlations are generally strong for all GRACE solutions considered (Fig. 7.3). Coherence is in particular high in the South Atlantic and Indian Ocean, where correlations of up to 0.8 and explained variances of 3 hPa^2 are obtained for GFZ. Correlations with bottom pressure records from the Crozet-Kerguelen region in the Indian Ocean are on the order of 0.7, in line with previous findings in the region based on early GRACE

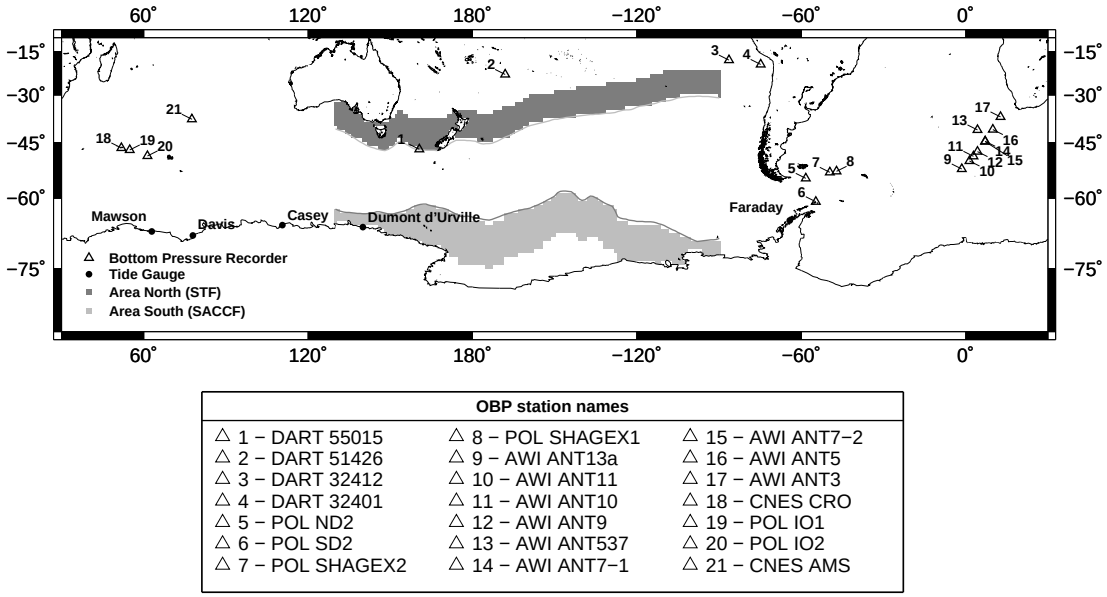

Figure 7.2: Location of in situ records available for this study: time-series of sea-level variations from coastal tide gauges in Antarctica (solid dots), and time-series from off-shore bottom pressure recorders in the Southern Ocean (triangles). Shaded areas indicate averaging areas for GRACE bottom pressure differences following the path of the Subtropical Front (STF) in the north (dark grey), and the Southern ACC Front (SACCF) in the south (light grey) given by Orsi *et al.* (2001).

releases (Rietbroek *et al.*, 2006). Correspondence is substantially smaller for stations in the Southern Pacific, with significant correlations obtained only for the ITG-GRACE2010 data, while GFZ and CNES/GRGS show insignificant correlations and zero or even negative explained variances here. However, in-situ time-series available from the area are rather short and mostly located in sub-tropical latitudes, where bottom pressure variability is expected to be weak and thus more difficult to observe by GRACE. Note that statistics based on monthly mean averages instead of low-pass filtered series do not reveal significant differences in correlations and explained variances.

Band pass filtered signals with periods between 10 and 30 days generally correlate better with ITG-GRACE2010 than CNES/GRGS. Explained variances frequently approach 2 hPa^2 for ITG-GRACE2010 in the South Atlantic, while the french solution typically remains below 1 hPa^2. Results are in particular promising in the South Atlantic region, where several multi-year in-situ time-series collected by the Alfred-Wegener-Institute (AWI) are available.

Variability beyond 10 days is solely accessible from the ITG-GRACE2010 solutions. High correlations together with generally positive explained variances suggest that ITG-GRACE2010

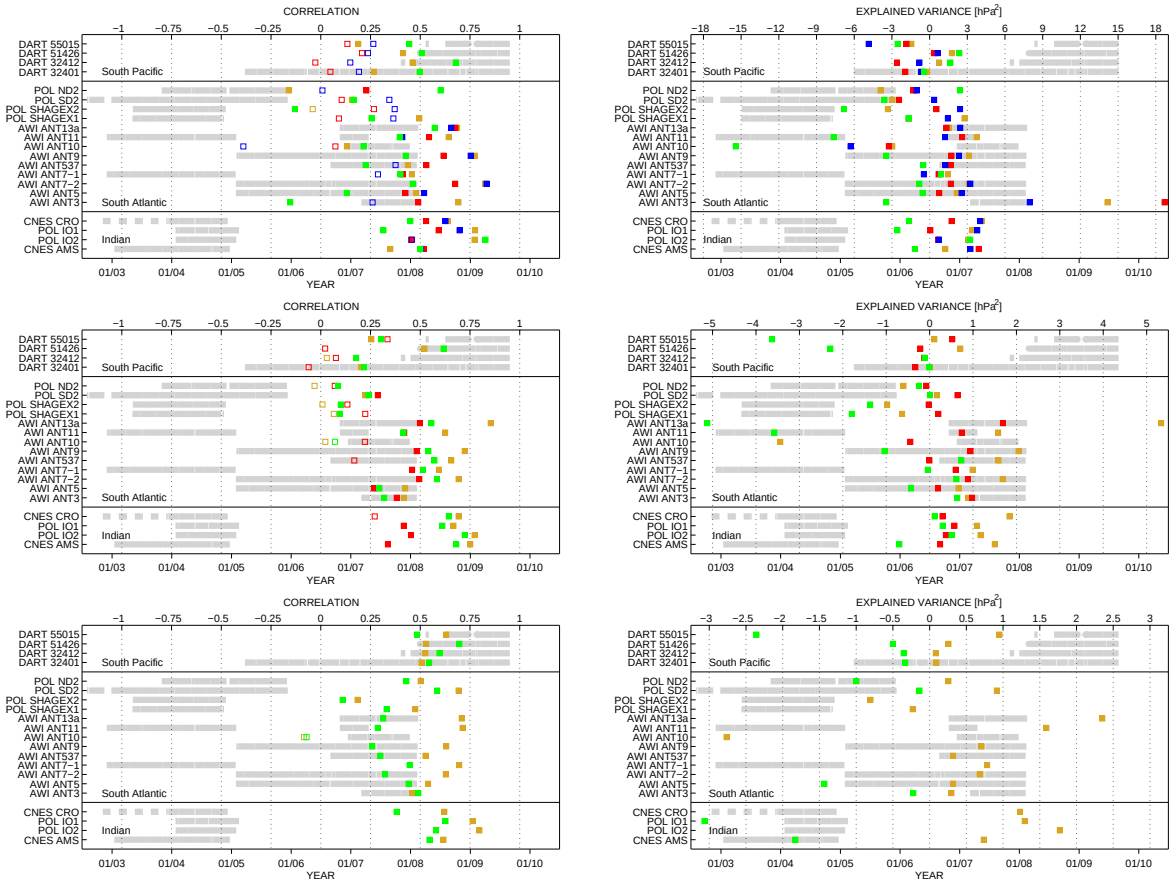

Figure 7.3: Correlations (left column) and explained variances (right column) of ocean bottom pressure from ITG-GRACE2010 (yellow), CNES/GRGS (red), GFZ (blue) and as simulated with OMCT (green) with all available time-series from off-shore bottom pressure recorders in the Southern Ocean. Filled squares indicate significant correlation at a confidence interval of 95%, open squares are found not significant. Signals have been separated into three different frequency bands containing signals with periods longer than 30 days (upper panels), periods shorter than 10 day (lower panels), and band-bass filtered variability between 10 and 30 days (middle panels). The grey bars indicate the time-span of bottom pressure recordings available.

does contain information on high-frequency ocean dynamics. Power spectra of bottom pressure from ITG-GRACE2010 and in-situ observations (not shown) are comparable for both data sets in that band. It can be inferred that modes between 9 and 7 days dominate most stations in the Southern Ocean. This is consistent with the results of Weijer & Gille (2005), who found modes with such frequencies in the transport from a constant-density, multilevel model of the Southern Ocean. In particular, a mode with a period of 8.3 d is apparent in the bottom pressure data. This topographically trapped mode is excited by the local bathymetry in the area of the East-Pacific Rise south west of Africa. Due to the fact that the flow of the

ACC goes through this region, the mode affects the ACC directly and therefore leads to a change in meridional ocean bottom pressure, which can be tracked by the OBP stations near the current.

In addition to the different GRACE solutions, simulated bottom pressure variations from OMCT are included into Fig. 7.3. OMCT is routinely applied as a background model to remove non-tidal ocean variability in the GRACE processing and can be thus assumed to represent the a-priori knowledge already available without flying a satellite gravity mission. Therefore, results from the various GRACE releases assessed in this paper are expected to provide additional information that goes beyond the predictions of OMCT. Here, results from OMCT simulations included in the release 04 of GRACE de-aliasing product (Flechtner, 2007) are shown. Apart from the stations in the South Atlantic, the different GRACE releases are generally able to explain more of the variability contained in the in-situ observations than the model. This is particularly true for the high-frequency band, indicating the ITG-GRACE2010 indeed provides information on non-tidal mass variability on synoptic time-scales that have not been introduced by the applied background model but originate instead from the processing approach developed at the University of Bonn.

7.1.4 Bottom pressure gradients, sea-level variations, and transports through Drake Passage from OMCT

Following the theoretical arguments of Hughes *et al.* (1999), we assume that (a) bottom pressure gradients averaged over the circumpolar flow path of the ACC are representative for its transport across Drake Passage, and (b) sea-level variability along the Antarctic coast might serve as a proxy for the bottom pressure gradient. We re-assess those relationships on sub-seasonal time-scales focussed on in this paper by means of model data from OMCT.

The zonal geostrophic component of the anomalous transport is obtained from the meridional bottom pressure gradient (Hughes *et al.*, 1999):

$$T_g = \frac{H}{f\rho_0}\left(p_b - p_a\right), \tag{7.2}$$

where H is the mean water depth, f the Coriolis parameter, $\rho_0 = 1030.93\mathrm{kg/m}^3$ a mean density of sea water and p_a, p_b the pressure anomaly at the southern and northern rim of the current, respectively. Bottom pressure and sea-surface height fields as well as total transports across Drake Passage at daily resolution have again been obtained from the OMCT simulation that was utilized for the AOD1B RL04 de-aliasing product.

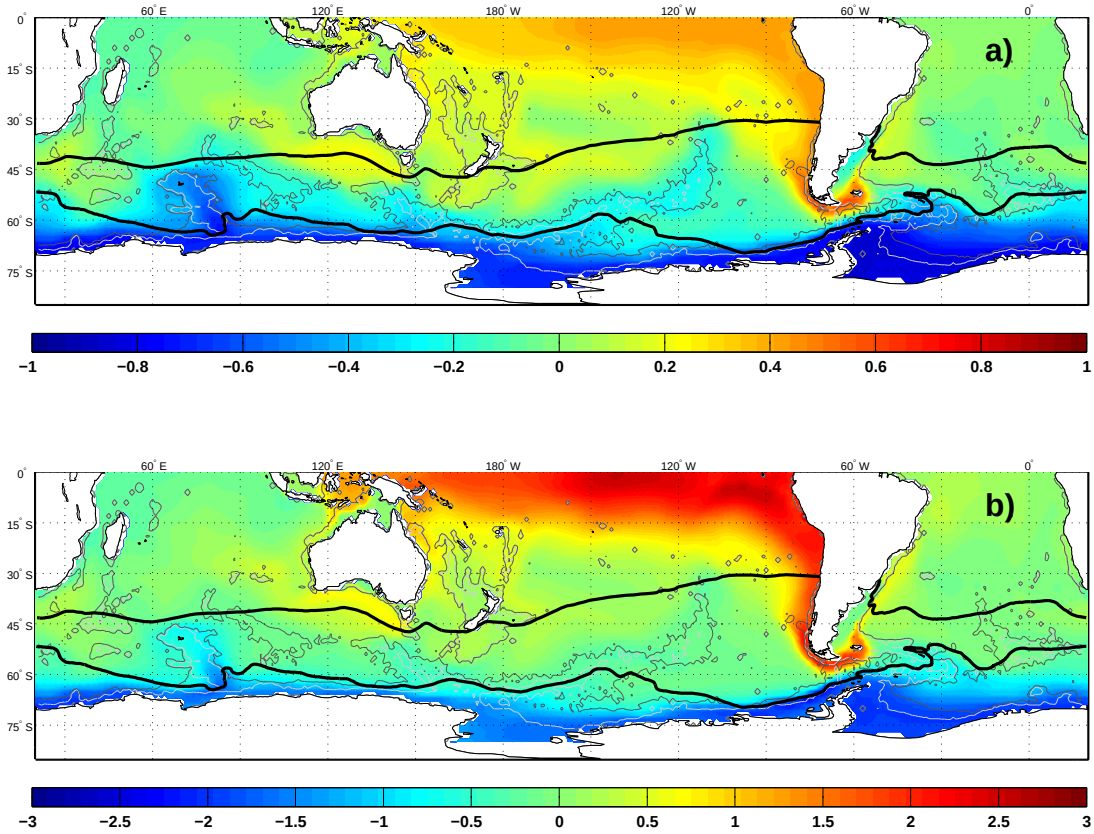

Figure 7.4: a) correlation and b) regression in Sv/hPa of ocean bottom pressure and transport variations in Drake Passage from OMCT; path of the Subtropical Front (STF, upper black line) and Southern ACC Front (SACCF, lower black line); contours show f/H-quotients, corresponding to depths of 3000 m (light grey) and 4000 m (dark grey).

7.1.4.1 ACC fronts in the Southern Pacific

The meridional extent of the ACC is usually defined to be bounded by the Subtropical Front (STF) in the north, that separates warm, salty subtropical waters from the fresher and cooler subpolar waters, and the Southern ACC Front, in the south, that is indicated by the first appearance of upwelling abyssal waters. In the South Pacific the current is located between 15° and 70° South. In order to describe the ACC transport variability by means of bottom pressure changes, Hughes *et al.* (1999) argues that ocean bottom pressure south to the main ACC flow path is useful proxy of transport variations. In contrast, Zlotnicki *et al.* (2007) suggested that bottom pressure differences between the Subtropical Front (STF) and the Southern ACC Front (SACCF) should be a better representative for the transport variability, in particular when satellite gravity observations are be considered.

To assess the sensitivity of ocean bottom pressure in the Southern Ocean to simulated baroclinic transport in OMCT at Drake Passage, correlation and regression maps between simulated transport and local bottom pressure variability are computed. Positive correlation and regression coefficients are found in lower latitudes (north of -20°), ranging from 0.2 to 0.4 and 1.0 to 3.5 Sv/hPa, where however, the simulated OBP signal is rather weak. At the same time, negative correlations and regression coefficients are obtained south of -60° from -0.2 to -0.7 and -1.0 to -3.0 Sv/hPa close to the Antarctic coast (see Fig. 7.4).

Comparing those model results with various estimates of the different ACC fronts (Orsi *et al.*, 1995; Sallée *et al.*, 2008; Sokolov & Rintoul, 2009), we choose to select 500 km wide averaging regions north of the STF and south of the SACCF, which essentially follow the suggestions by Zlotnicki *et al.* (2007). Positions of the those fronts have been obtained from Orsi *et al.* (2001).

7.1.4.2 Sea level variations from OMCT

Sea surface height fields from OMCT are corrected for the effect of atmospheric loading by assuming an ideal inverse barometer (Wunsch & Stammer, 1997). From those fields, two time-series have been derived: (1) mean sea-level variability around Antarctica, by averaging all coastal cells as defined by the OMCT bathymetry, and (2) sea-level variability at the position of the Faraday tide gauge at the Antarctic Peninsula. This position has been selected since at Faraday base (operated since 1996 by Ukraine under the name Vernadsky) a multi-year record of high-quality sea-level observations exists that has been previously shown to be an ideal proxy data-set for ACC transport variability (e.g., Hughes, 2003).

7.1.4.3 Analysis of simulated time-series from OMCT

From all OMCT data-sets, i.e., the full transports through Drake Passage (multi-year mean transport for 01/2002 - 12/2009 is 118±9 Sv), bottom pressure and sea-level time-series, we estimate and remove linear trends as well as annual and semi-annual sinusoids (Fig. 7.5). The anomalies are subsequently separated into three different frequency bands as defined above. We calculate bottom pressure gradients from two paths defined by the STF and SACCF (hereafter referred to as bottom pressure gradients) and bottom pressure from the region south of the SACCF (hereafter referred to as the SACCF region bottom pressure), both averaged over the width of the South Pacific as indicated in Fig. 7.2.

Highest correlations for the low pass filtered time-series are obtained between Drake Passage transports and the mean sea-level variability all around Antarctica (-0.94, see Table 7.2).

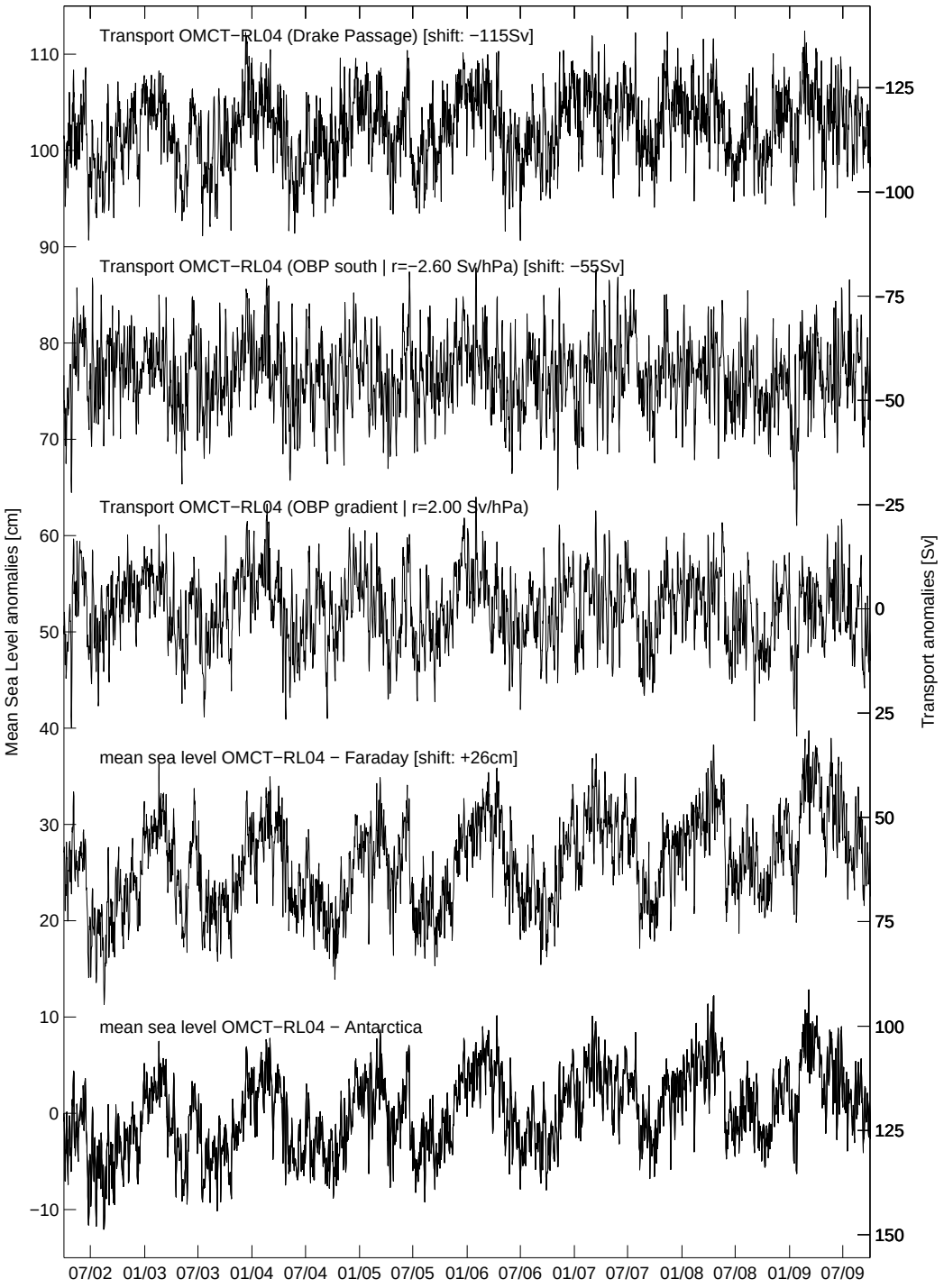

Figure 7.5: Simulated OMCT time-series (unfiltered daily resolution) of the full ACC transport across Drake Passage, the geostrophic component of the transport as derived from bottom pressure gradients (STF-SACCF) and bottom pressure variations south of the SACCF across the Pacific, as well as sea-level variations averaged along the coast of Antarctica and at the position of Faraday gauge. Note that transports refer to scale on the left-hand side, which has been inverted for ease of comparison.

Table 7.2: Correlations between time-series simulated by OMCT[1]

	Transport (DP)	SAM	MSL Antarctica	OBP Antarctica	MSL Faraday
A) 30 days low pass filter					
STF - SACCF	0.79	0.62	-0.84	-0.83	-0.77
SACCF	-0.86	-0.67	0.88	0.87	0.79
Transport (DP)		0.61	-0.94	-0.94	-0.88
MSL Antarctica					0.94
B) 10 - 30 days band pass filter					
STF - SACCF	0.55	0.56	-0.62	-0.59	-0.57
SACCF	-0.60	-0.53	0.61	0.61	0.54
Transport (DP)		0.41	-0.84	-0.85	-0.78
MSL Antarctica					0.95
C) 10 days high pass filter					
STF - SACCF	0.29	0.41	-0.65	-0.65	-0.47
SACCF	-0.19	-0.37	0.57	0.59	0.37
Transport (DP)		0.17	-0.51	-0.51	-0.50
MSL Antarctica					0.81

[1] index for the Southern Annular Mode (SAM), full ACC-transport across Drake Passage (DP), geostrophic component of the ACC transport as derived from bottom pressure gradients from Subtropical Front and Southern ACC Front defined by Orsi *et al.* (1995), mean sea-level (MSL) and ocean bottom pressure (OBP) averaged along the coastline of Antarctica and mean sea-level at the position of Faraday tide gauge.

Correlation with sea-level at Faraday is only slightly weaker (-0.88), supporting the notion that the station is indeed well placed to monitor transport variability at Drake Passage. Geostrophic contributions to the flow obtained from bottom pressure gradients and SACCF region bottom pressure are correlated with Drake Passage transport with 0.79 and -0.86, indicating that a large part of the flow can be tracked by both pressure gradients as well as by bottom pressure variations in the SACCF region. When the coastal bottom pressure variability all along the Antarctic coastline is considered, correlations are not significantly different, i.e -0.83 with bottom pressure gradients. This results partly from the hydrostatic approximation in OMCT modeling, inducing a linear connection between sea-level and ocean bottom pressure variations, and the limited spatial resolution of OMCT. At 1.875° spatial resolution, the model does not reproduce mesoscale eddies, suggesting that the correspondence between sea-level and bottom pressure is certainly exaggerated in OMCT.

For higher frequencies, correlations between transport and both bottom pressure gradients and SACCF region bottom pressure are still significant at the 95% confidence level, indicating that transport variability can be indeed explained by ocean bottom pressure observations

even on time-scales of a few days. However, bottom pressure gradients show slightly higher correlations with both Drake Passage transport and sea-level variations when compared to SACCF region bottom pressure, indicating that bottom pressure gradients averaged over the South Pacific might be more appropriate to monitor the flow variability at shorter periods.

In addition, potential error sources in the GRACE estimates, which include leakage of terrestrial water storage and ice mass variations into the ocean domain, remaining systematic errors that are primarily correlated in meridional direction, as well as less well constrained low degree Stokes coefficients, are expected to affect more strongly estimates of SACCF region bottom pressure close to the Antarctic coast than bottom pressure gradients. In the remainder of this study, we therefore primarily rely on GRACE results obtained from bottom pressure gradients between STF and SACCF, while SACCF region estimates are only occasionally included for comparison.

7.1.4.4 Estimation of optimal regression factor between ocean bottom pressure and transport variations

For eq. (7.2) to be valid, the current is required to flow along H/f contours that encircle the Antarctic continent. This path of the current is assumed to be constant in time. Transport and pressure gradient simulated with an ocean model can therefore be used to estimate an effective value for H/f (Hughes *et al.*, 1999). Using OMCT model time-series from transport variations in Drake Passage that were filtered with a 30-days low pass filter, a regression coefficient of 1.4 Sv/hPa for bottom pressure gradients between STF and SACCF, and -2.1 Sv/hPa for ocean bottom pressure variations south of the SACCF is estimated. These regression factors explain the model transport variance with ocean bottom pressure gradient to 62% and with SACCF region bottom pressure to 73%.

Those regression values are lower than in previous studies. Meredith *et al.* (1996) obtained values of 2.70 Sv/hPa and 2.26 Sv/hPa between two bottom pressure gauges situated north and south of the main current by assuming the transport variability is entirely barotropic. Similar arguments were applied by Zlotnicki *et al.* (2007), who derived a value of 3.1 Sv/hPa for the pressure gradient across the current with an average depth H and geographical latitude ϕ. Although up to 3.7 Sv/hPa were obtained for subsurface pressure along the coast of Antarctica based on FRAM model simulations (Hughes *et al.*, 1999). More recent analyses of OCCAM model output indicated a relation of only 1.2 Sv/hPa with bottom pressure observations at station SD2 south of Drake Passage (Hughes, 2003), suggesting that assuming entirely barotropic conditions is certainly not justified by observations. These lower regression coefficients are also supported by Whitworth III & Peterson (1985), who used in-situ data of

transport moorings and bottom pressure recorders at each side of Drake Passage to obtain a regression value of 1.9 Sv/hPa.

In order to justify our scaling coefficient more tightly, additional simulations with a new OMCT model version at 1° resolution have been evaluated. From this simulation, we get regression values of 2.2 Sv/hPa and -3.1 Sv/hPa for pressure gradients and SACCF region bottom pressure, respectively. In view of the apparent dependence from the model configuration employed, we decide to rely on approximate values of 2.0 Sv/hPa and -2.6 Sv/hPa to subsequently translate bottom pressure gradients and SACCF region bottom pressure from GRACE into ACC transport variations in the next section.

7.1.5 ACC transports from GRACE and Antarctic sea-level observations

Following eq. 7.2, ACC transports are derived from the three different GRACE bottom pressure distributions from GFZ, CNES/GRGS and ITG-GRACE2010 by averaging over the bottom pressure gradients indicated in Fig. 7.2, and contrasted against tide gauge observations from the Antarctic continent. Hourly tide gauge data covering the study period were available at four stations in the Australian Sector (Casey, Mawson, Davis and Dumont d'Urville) as well as at Faraday on the Antarctic Peninsula (Tilo Schöne, pers. comm.). Hourly tide gauge data have been transformed to daily values by applying a Doodson filter in order to damp out the main tidal frequencies (IOC, 1985). Subsequently, daily atmospheric data from ECMWF were used to correct the sea-level series for inverse barometric effects. As for the transports, a long-term mean, trend, as well as annual and semi-annual periodic terms have been removed from the sea-level anomalies prior to comparison.

Transport anomalies derived from the three different GRACE solutions are broadly consistent with each other (Fig. 7.6). RMS variabilities for 30-day lowpass filtered solutions are 3.6 Sv for GFZ, 3.3 Sv for CNES/GRGS and 2.8 Sv for ITG-GRACE2010. ITG-GRACE2010 daily solution exhibits substantial high frequency variability which cannot be reflected by the other two series, but which is also apparent in the tide gauge data. While concentrating on signal periods longer than 30 days, highest correlations of more than 0.6 are obtained between GFZ- and CNES/GRGS-based transports and sea-level variations at Mawson (Tab. 7.3). Correlations are approximately two tenth lower with respect to the synthetic OMCT data, indicating both the impact of observation errors and the contribution of meso-scale near-surface variability as discussed above.

For variability between 10 and 30 days, correlations drop to around 0.3 for most tide gauges, while CNES/GRGS and ITG-GRACE2010 are still showing good agreement to each other.

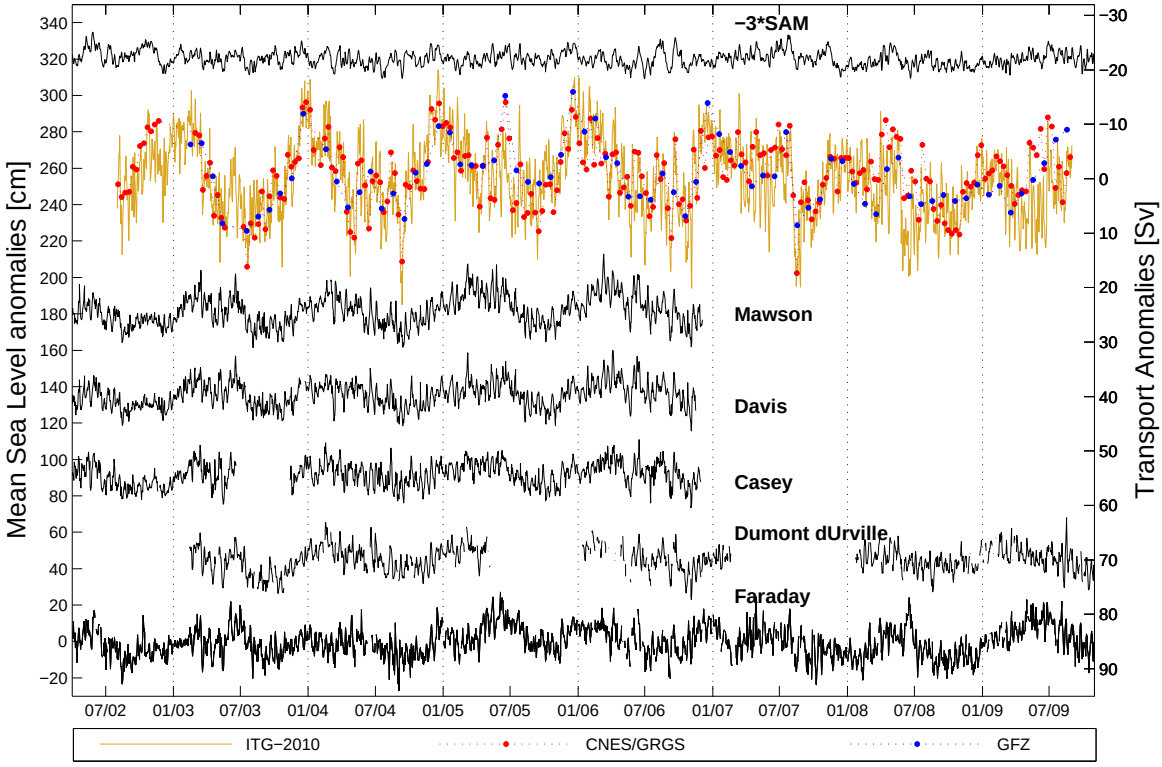

Figure 7.6: Geostrophic ACC transport anomalies (unfiltered, up to daily resolution) as derived from different GRACE products with regression factor $r = 2.0$ Sv/hPa, time-series of sea-level variations at different coastal tide gauges. Geostrophic daily values of SAM index (normalized values multiplied with factor -3 on left axis), transport estimated from different GRACE solutions and (IB-corrected) sea-level at Mawson, Davis, Casey, Dumont d'Urville and Faraday.

For the high-frequency variability with periods below 10 days, correlations for ITG-GRACE2010 vary for all tide gauges between -0.15 and -0.27 which is consistent with the value of 0.2 as found from OMCT model data, underlining the weak but significant connection between geostrophic transport variabilities and sea-level variations even on the shortest time-scales considered.

Linear regression coefficients of transport variations estimated from GFZ RL04, CNES/GRGS and ITG-GRACE2010 solutions and 30-day low pass filtered mean sea-level data from tide gauges varies between -0.43 to -0.51 Sv/cm, -0.33 to -0.63 Sv/cm and -0.35 to -0.58 Sv/cm each. Even in the low pass filtered band the time-series of tide gauge stations show more variability than estimated transport variations from GRACE, which might be related to local effects affecting the tide gauges (e.g. sea ice, fresh water fluxes from the continent) which are not sensed by a satellite gravity mission.

Table 7.3: Correlation between observed time-series[1]

	SAM	ITG-GRACE2010	CNES/GRGS	GFZ
(A) periods longer than 30 days				
Faraday	-0.44	-0.46 (0.47)	-0.39 (0.37)	-0.56 (0.58)
Dumont d'Urville	-0.56	-0.52 (0.54)	-0.45 (0.47)	-0.45 (0.47)
Casey	-0.64	-0.55 (0.50)	-0.59 (0.55)	-0.52 (0.53)
Davis	-0.49	-0.46 (0.39)	-0.52 (0.54)	-0.50 (0.55)
Mawson	-0.63	-0.51 (0.45)	-0.61 (0.60)	-0.58 (0.61)
SAM		0.67 (-0.58)	0.72 (-0.70)	0.63 (-0.60)
(B) periods between 10 and 30 days				
Faraday	-0.38	-0.27 (0.18)	-0.15 (0.13)	
Dumont d'Urville	-0.43	-0.33 (0.29)	-0.34 (0.35)	
Casey	-0.38	-0.31 (0.24)	-0.33 (0.32)	
Davis	-0.35	-0.30 (0.21)	-0.28 (0.31)	
Mawson	-0.39	-0.30 (0.22)	-0.26 (0.29)	
SAM		0.52 (0.26)	0.46 (-0.39)	
(C) periods shorter than 10 days				
Faraday	-0.16	-0.22 (0.19)		
Dumont d'Urville	-0.36	-0.23 (0.22)		
Casey	-0.26	-0.27 (0.23)		
Davis	-0.30	-0.19 (0.16)		
Mawson	-0.28	-0.17 (0.14)		
SAM		0.32 (0.15)		

[1] mean sea-level at various tide gauges all along the coast of Antarctica (Faraday, Dumont d'Urville, Casey, Davis, Mawson), geostrophic transport derived from ocean bottom pressure gradients (ocean bottom pressure variations of southern path) across the Pacific as seen by different GRACE products [ITG-GRACE010, CNES/GRGS, GFZ], and an index for the Southern Annular Mode (SAM).

7.1.6 ACC transports from model and GRACE and the Southern Annular Mode

There is strong evidence in terms of both observations and theoretical reasoning (see Meredith, 2004, for a summary) that a strong relation exists between ACC transport variability and the prevailing surface wind field in middle latitudes of the Southern Hemisphere. By means of the ECCO model and monthly GRACE solutions, Ponte & Quinn (2009) demonstrated a connection between ocean bottom pressure variations and zonal wind stress anomalies which is induced by Ekman dynamics in the Southern Ocean. ACC transports from OMCT and GRACE as well as sea-level observations are therefore contrasted against an index for the Southern Annular Mode (SAM) provided by the CPC (Climate Prediction Center,

http://www.cpc.ncep.noaa.gov). This normalized daily index is based on a loading pattern obtained from the leading EOF of geopotential height anomalies at the 700 hPa level in the Southern Hemisphere poleward of 20° over a base period of two decades, multiplied with the daily pressure distribution. As for all time- series considered in this study , trend as well as annual and semi-annual harmonics are removed. The reduced index is displayed in Fig. 7.6 and has been subsequently separated into the three different frequency bands.

A linear regression of daily OMCT transport variations and the SAM index gives a ratio of 2.6 Sv/[unit SAM]. The time-series of the SAM index has a standard deviation of 1.1 [unit SAM]. This result is close to the values estimated by Hughes (2003) with modeled transport of OCCAM (2.8 Sv/[unit SAM]). In the 30 day low pass filtered domain correlations between SAM and transport in Drake Passage and in the South Pacific lie in the range of 0.61 to 0.62 (-0.67 for SACCF; see Tab. 7.2).

Comparing SAM with GRACE results and sea-level variations from Antarctic tide gauges for periods longer than 30 days, wind variability is strongly correlated with sea-level records from all five available stations, with highest correlations of 0.64 obtained for Casey. In addition, correlations between SAM and the transports from different GRACE products are equally high, approaching 0.72 for the CNES/GRGS solutions. These values are substantially higher than any of the correlations between GRACE and a single tide gauge record, indicating that GRACE indeed sees hemispherically coherent mass variations that are connected to the prevailing winds.

Correlations between SAM and GRACE are substantially weaker for the band-pass filtered signals with periods between 10 and 30 days, with maximum correlations of 0.52 obtained for the ITG-GRACE2010 bottom pressure estimates and 0.32 for periods below 10 days. These correlations are slightly lower than estimates from OMCT model results (0.56 for band pass filter and 0.41 for high pass filter) and appear plausible since the noise level is generally increasing at higher frequencies (and hence shorter averaging intervals), where transient weather features start to dominate local observations.

Finally, lagged correlations between bottom pressure gradients from ITG-GRACE2010 and SAM in the low pass filtered band reveal a time shift of one day. This is in contrast to the results given by Wearn & Baker (1980) who found a time lag of nine days when correlating hemispherically wind and transport variations in Drake Passage. Even in the high pass filtered band the time lag is less than one day. A comparable time-lag has been obtained by Wearn & Baker (1980) only for the relation of local wind and sub-surface pressure variation in Drake Passage. Initial results obtained here from ITG-GRACE2010 indicate that the adjustment of

bottom pressure to changing surface winds is even on a hemispheric scale much faster than thought before.

7.1.7 Summary and Conclusions

Newly available gravity field solutions with higher than monthly temporal sampling have been evaluated in terms of their information content on Southern Ocean dynamics. Validation of bottom pressure distributions against a limited number of available in-situ records indicates that GRACE is indeed able to provide bottom pressure variability with periods down to a few days, when advanced processing concepts such as the Kalman filtering approach developed at the University of Bonn are applied.

Pressure gradients from GRACE across the Pacific translated into geostrophic transport anomalies of the ACC in Drake Passage with applying a regression coefficient of 2.0 Sv/hPa vary in a range of ±20 Sv. They are strongly correlated with sea-level variability along the Antarctic coast as inferred from coastal tide gauge data. Correlation is in particularly apparent on time-scales longer than 30 days, but significant correlations also exist on periods below 10 days.

In addition, GRACE-based meridional bottom pressure gradients reveal significant (>0.6) correlations with the SAM on periods above 30 days, which is even higher than correlations achieved with any of the tide gauge records. This underlines once more the strong relation of the transport variations (i.e., the bottom pressure distributions they are based on) with the dominant pattern of large-scale atmosphere dynamics on the Southern Hemisphere.

This study indicated that GRACE is able to observe bottom pressure variability that goes beyond the a-priori knowledge contained in the background model OMCT. Similar conclusions have been also drawn by Bonin & Chambers (2011) from comparisons with satellite-based sea-level anomalies for the ITG-GRACE2010 solutions. For the upcomming release 05 of GRACE, a new OMCT version with 1° resolution (see section 7.1.4.4) is incorporated, that shows substantially improved bottom pressure variability in particular on sub-weekly periods. In addition to conventionally improved background models, further developments in combining numerical model information with data either by means of incorporating stochastic a-priori information into the gravity field determination process, or by means of incorporating high resolution geodetic observations into a numerical ocean model by means of data assimilation approaches (Saynisch & Thomas, 2012), appear promising to cope with the high-frequency non-tidal ocean mass variability sensed by satellite gravity missions.

With new GRACE products available at daily resolution, a combination with more traditional oceanographic observation types can be aspired. This might include the removal of mean barotropic variability from campaign-like current meter observations that are occupied only for a limited time span. Combinations with complementary satellite observations covering identical time-frames become also now feasible. While the barotropic flow component is obtained from GRACE, sea-surface height anomalies from the satellite altimetry mission TOPEX/Poseidon and its successors can provide information on a large part of the baroclinic variability (Gille *et al.*, 2001). Improved re-tracking algorithms suitable to obtain highly accurate sea-level anomalies also near the coasts (see, e.g., Gommenginger *et al.*, 2011, for recent technological developments), in connection with an independently obtained high-resolution geoid from GOCE (Rummel *et al.*, 2011) serving as a reference surface for calculating absolute surface geostrophic velocities, calls for a re-assessment of previous studies that attempted to monitor the variability of the Antarctic Circumpolar Current from space.

7.2 Ocean bottom pressure variations in the North Pacific[3]

GRACE based OBP variability in the northern Pacific shows strong signals along the flank between the subpolar and subtropical gyre. Seasonal and interannual OBP fluctuations are connected to changes in the upper wind field (see Ch. 2.2.5). The barotropic oceanic transport is locally balanced by the curl of the surface wind stress (Bingham & Hughes, 2006; Song & Zlotnicki, 2008). Whereas correlation analysis of the interannual OBP variations reveal a relation to the ENSO phenomena, secular trends in OBP are rather referenced to the PDO (Cheng *et al.*, 2013). Petrick *et al.* (2014) used simulated ocean bottom pressure and sea level pressure (SLP) as representative for the surface wind field from NCAR's Community Earth System Model (CESM) and the RL04 version of OMCT to investigate the relation between OBP and large-scale atmospheric variability and to identify the actual physical mechanism in the northern Pacific. Additionally, observations of SLP from ERA-interim and OBP from GRACE have been used. All data sets were de-trended, de-seasonalized and the regional spatial mean has been reduced.

In the first step, the direct relation between OBP and SLP has been investigated. Therefore, an Empirical Orthogonal Function (EOF) decomposition of the modeled SLP data has been performed to find the dominant pattern in the surface wind field. Afterwards, a robust multiple linear regression approach has been used to define a functional relation between

[3]This section is a summary of the work of Petrick *et al.* (2014) where contributing work has been done by the author by processing and analyzing of the GRACE based OBP fields as stated in the text.

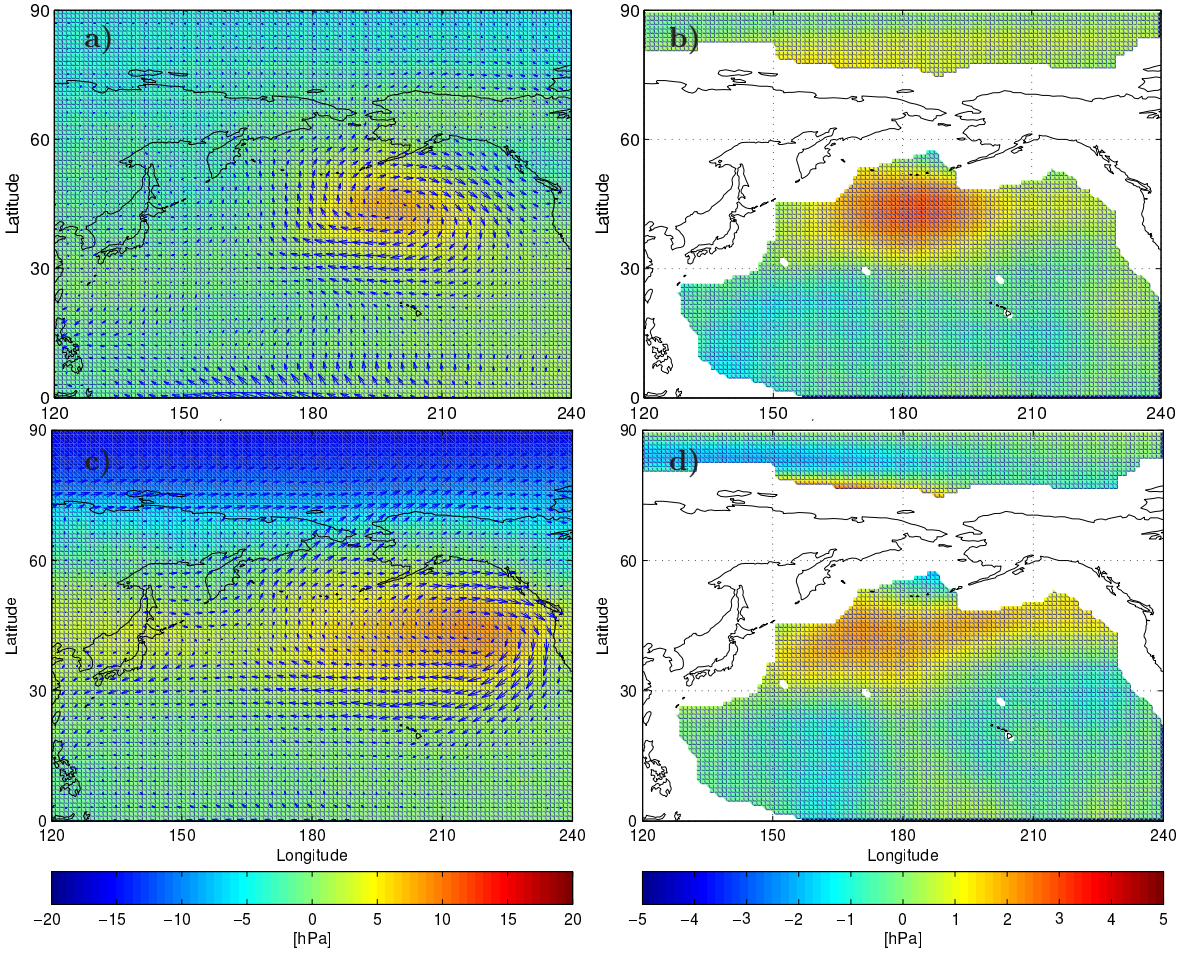

Figure 7.7: Composite mean differences for (top) the Southern Oscillation Index and (bottom) the NAM index of 10-years of ERA-interim atmospheric pressure (a,c) and GRACE ocean bottom pressure (b,d). The vector field in a) and c) indicates the corresponding surface wind field.

SLP and OBP. The first, second and forth EOF only allow to reconstruct the modeled OBP signal from SLP with the major features and realistic amplitudes. These EOF patterns are related to the Aleutian low and the Pacific North American Pattern (EOF 1), the North Pacific Oscillation (EOF 2) and a covarying signal located on the Aleutian low and over the Arctic (EOF 4). High correlations (0.85) of the modeled and reconstructed OBP time series show empirical evidence for OBP variations in response to the surface winds in the North Pacific.

In the next step, the relation of observed OBP and a distinct climate mode is assessed. Two climate modes were considered. The first one is the Southern Oscillation Index (SOI) as representative for the ENSO phenomena. It is defined as the double-standardized difference in SLP between Tahiti (131°E, 13°S) and Darwin (210°E,18°S). The second one is the Northern

Annular Mode (NAM), defined as the first EOF of de-seasonalized SLP north of 20°N. Both climate modes are calculated from ERA-interim. Composite mean differences of monthly GRACE based OBP fields have been calculated by definition of the maximum (larger than 1 standard deviation) and minimum (smaller than -1 standard deviation) conditions of the indices.

The Aleutian Low (centered at 45°N, 160°E; see Fig. 7.7 a) is 7 hPa lower during the maximum and minimum peaks of ENSO (El Niño and La Niña). The respective OBP pattern (Fig. 7.7 b) shows a negative pressure anomaly at the northern flank of the subtropical gyre. For NAM, similar SLP patterns are found compared to ENSO but a dominant pressure anomaly of around 10 hPa is seen at the eastern part of the north Pacific that is more enhanced than the Aleutian low during El Niño (Fig. 7.7 c). Corresponding changes in OBP are rather located at the western part of the North Pacific (Fig. 7.7 d) for NAM than for ENSO.
Those findings are in line with the analysis of Li & Wettstein (2012) on driving processes of the North Pacific atmospheric jets, which are both thermally and eddy driven. Thermal driving originates in the tropics and is communicated to higher latitudes by the Hadley circulation. Eddy momentum flux convergence is instead related to the midlatitude dynamics. The good correspondence of OBP variations to both indices is an indication for the relation to surface wind conditions characterized by both tropical and extratropical atmospheric variability.
The relation of the secular trend behavior in OBP more to the PDO results from the definition of the PDO. It is characterized by a specific temperature anomaly in the subtropical north Pacific and also connected to sea level anomalies at the Aleutian Islands. Therefore, an overlap of the SLP field of ENSO and NAM with PDO is given. Finally, it is not possible to refer OBP variations in the North Pacific just to one specific climate mode. The surface wind regime in the northern Pacific area is reflected in the OBP variability. GRACE based observations are an integrated measure of these atmospheric surface pressure and wind conditions in this region.

Chapter 8

Summary and conclusions

Data of the GRACE mission over one decade (2003–2013) from different releases of several processing centers have been used for two important oceanographic applications. On global scales, GRACE data provide the opportunity to estimate temporal variations of the global ocean mass and therefore the eustatic contribution to changes in sea level. With the latest RL05 data of GFZ an ocean mass rate of 1.36±0.1 mm/yr has been estimated. For completeness of the mass signal, degree-1 terms were estimated by application of a further development of the method of Swenson *et al.* (2008). Therefore, three different test cases have been calculated for the consideration of the eustatic signal. Additionally, the processing strategy has been iterated for five times. The results showed fast convergence for all tested cases and were leading to practically identical results of degree-1 coefficients and also to global ocean mass variations. Whereas initially the eustatic contribution has been included by a global homogeneous distribution (Bergmann-Wolf *et al.*, 2014), in a more recent development effects of Loading and Self-Attraction have been taken into account which led to regionally different relative sea level variations. Due to LSA effects, the rate of eustatic sea level variations has been reduced to 1.23 mm/yr which is a difference of 0.13 mm/yr compared to the results of Bergmann-Wolf *et al.* (2014) and still in range with previous studies (e.g. Baur *et al.*, 2013). In the second application part, the focus has been laid on mass transport variations of the Antarctic Circumpolar Current and its connection to the atmospheric dynamics on the Southern Hemisphere. Three different GRACE products have been used here: (1) monthly data from RL04 of GFZ, (2) 10-day solutions of CNES/GRGS (RL02) and (3) daily data from the University of Bonn (ITG-GRACE2010). Those data sets were analyzed together with in situ observations of OBP recorders and tide gauges along the Antarctic coast in three different frequency bands. The estimated transport variations ranged between +/-20 Sv and showed significant correlations for the low-frequency ($>$ 30 days) but also for the high frequency ($<$

10 days) domain. The Southern Annular Mode has been chosen as representative for the main features of the atmospheric dynamics on the southern hemisphere. Correlations of GRACE based transport variations and SAM index are larger than 0.6 even for the high frequencies. Additional investigation of model based OBP and estimated transport variations revealed the ability of GRACE to observe high frequency variations which are not modeled by the background model OMCT available at the time of the GRACE processing.
Besides those oceanographic applications, work has been done for the development of the latest release 05 of the OMCT model used for the generation of the AOD1B product. The differences between RL04 and RL05 were compared to in situ OBP observations and applied for correcting altimetry based SSH measurements.

The GRACE mission is an ongoing success for the geo-scientific community. For the first time, GRACE-based mass estimates contributing to current sea level rise were included into the IPCC Fifth Assessment Report which has a significant impact on decisions of policymakers concerning environmental and development policy. At the same time, the approval of the GRACE Follow-On (GRACE-FO) mission to guarantee continuous gravity observations demonstrates the importance of the work over the last 12 years. Planned for launch in August 2017, GRACE-FO will continue the global monitoring of the Earth's gravity field but with updated sensor versions of the microwave ranging instrument, the GPS receivers and the accelerometers. Additionally, a laser ranging interferometer (LRI) will be tested for improved satellite-to-satellite tracking measurement performance. Simulations of the GRACE-FO orbit scenario have shown an improvement in the determination of near zonal coefficients above degree 60 when using LRI data instead of data from the microwave instrument (Flechtner *et al.*, 2015). These improvements will result in slightly less striping patterns in the spatial domain compared to GRACE data.
In addition, studies for next generation gravity missions with new orbit constellations and improved instrumentations of the satellites are already performed in order to realize higher spatial and temporal resolution (Sneeuw *et al.*, 2004; Panet *et al.*, 2013) and for reducing aliasing effects by assessing the error budget in the background models (Wiese *et al.*, 2009; Dobslaw *et al.*, 2016). Gruber *et al.* (2014) presented a mission concept for a longterm high precision and homogeneous determination of the time variable gravity field which is a synthesis of three previous gravity mission studies (two ESA studies and e.motion mission proposal). A double pair mission is proposed with a nearly polar pair like GRACE and additionally an inclined pair with an inclination of 70°. Each pair is flying in an orbit altitude of around 420 km and with an inter satellite distance of 100 km. With that configuration, a monthly geoid height error of 1 mm at a minimum spatial resolution of 200 km should be reachable. Numerical simulations with this double pair constellation indicate improved geoid performance but

still model errors of the background models will play an important role in the error budget of the satellite mission.

For the improvement of ocean models, time series and error budgets of GRACE based OBP variations have been used in assimilation strategies (Koehl *et al.*, 2012; Saynisch *et al.*, 2015). Assimilating GRACE based OBP data together with other oceanographic data sets (e.g. altimetry) in the GECCO-2 ocean model results showed just small changes compared to other introduced data sets but lead to significant changes in the barotropic stream function in the GECCO2-model (Koehl *et al.*, 2012). Due to the large errors in the GRACE products, improvements in the modeled barotropic circulation have not been expected because of the same range of changes in model values and the GRACE error budget. Therefore, Saynisch *et al.* (2015) included the maximum error budget of the CSR, GFZ and JPL monthly GRACE solutions in their assimilation strategy and focussed solely on the information in the GRACE data, neglecting other data sets. On the one hand, improved modeled OBP anomalies could be achieved compared with the GRACE observed fields and on the other hand, better agreements with independent in situ observations have been reached, showing the potential of information content in future gravity data if the error budget and higher order correlated errors will be reduced.

Until the launch of GRACE-FO a gap of presumably one year could be necessary to be bridged bringing along the necessity of using other observations and methods for closing the observational gap of time variable global gravity field products. Joint inversion methods mainly based on GPS measurements in a network of permanent stations (Kusche & Schrama, 2005; Wu *et al.*, 2006; Rietbroek *et al.*, 2014) based on the loading inversion method by Blewitt *et al.* (2001) are often favored. Due to the heterogeneous distribution of GPS stations in the network the method is sensitive to spatial aliasing effects. For sparse station coverage the estimated loading signal is damped or falsely amplified which results in a spatial shift of the maximum signal (Rietbroek *et al.*, 2014). To answer the question, where GPS stations should be located to reproduce the loading signal reliable, Kuhlmann *et al.* (2015) applied an EOF decomposition on GRACE data to reconstruct the non-tidal ocean loading (NTOL) signal. Around 5 to 10 stations are sufficient for the reconstruction of the global NTOL distribution for monthly up to daily GRACE data whereas the locations of the estimated stations are dependent on the temporal resolution of the GRACE data. Using EOF patterns estimated from GRACE as prediction, the reconstruction method might also be able to fill the data gap between GRACE and GRACE-FO.

Appendix A

Ocean Bottom Pressure Recorders - database

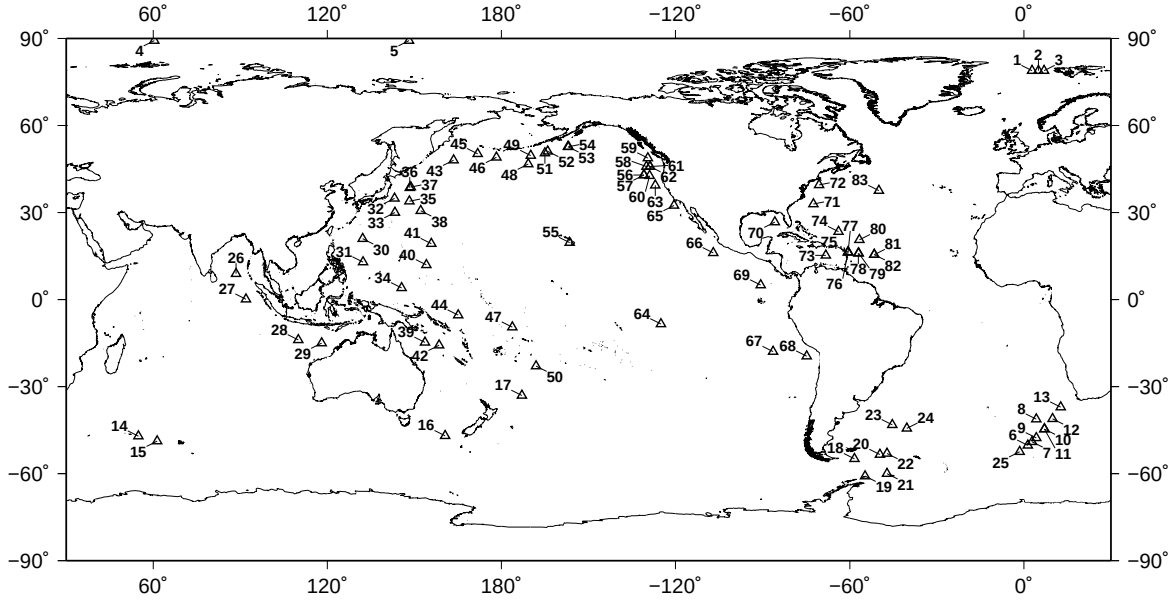

Figure A.1: Global distributed OBPR stations from Macrander *et al.* (2010). Metadata information for each station is given in Table A.1.

Table A.1: Metadata of global distributed OBPR stations from Macrander *et al.* (2010).

Station Number	Station Name	Longitude [°]	Latitude [°]	Depth [m]
Arctic				
1	AWI F8	2.7932	78.8312	2505
2	AWI F6	5.0145	78.8322	2712
3	AWI F4	7.0048	78.8385	1420
4	APL ABPR-1	60.3597	89.2543	4300
5	APL ABPR-3	148.1257	89.2475	4300
Southern Ocean				
6	AWI ANT11	1.4325	-50.2622	3889
7	AWI ANT10	2.8338	-49.0107	4059
8	AWI ANT537	4.2528	-41.1828	4867
9	AWI ANT9	4.2617	-47.6560	4568
10	AWI ANT7-2	7.0822	-44.6640	4616
11	AWI ANT7-1	7.0838	-44.6625	4619
12	AWI ANT5	9.9438	-41.1340	4733
13	AWI ANT3	12.7693	-37.0927	4848
14	POL IO1	54.9008	-47.1167	3944
15	POL IO2	61.2797	-48.8317	3917
16	DART 55015	160.5620	-46.9220	n.a.
17	DART 54401	-172.9850	-33.0050	n.a.
18	POL ND2	-58.3568	-54.9432	1148
19	POL SD2	-54.7133	-60.8505	1080
20	POL SHAGEX2	-49.5303	-53.3868	1510
21	POL MYRTLE	-47.1700	-60.0497	2354
22	POL SHAGEX1	-47.1020	-53.0810	1504
23	POL GRACE-3	-45.3017	-43.1983	5141
24	POL GRACE-2	-40.3698	-44.4200	5114
25	AWI ANT13a	-1.4007	-52.5070	2823
Indian Ocean				
26	DART 23401	88.5400	8.9050	n.a.
27	DART 53401	91.8990	0.0500	n.a.
28	DART 56001	110.0040	-13.9610	n.a.
29	DART 56003	117.9890	-15.0210	n.a.
Pacific Ocean				

30	DART 52404	132.2230	20.9490	n.a.
31	DART 52405	132.3330	12.8810	n.a.
32	KESS E1	143.1600	34.8300	5420
33	KESS S1	143.3100	30.0200	6056
34	DART 52403	145.5970	4.0330	n.a.
35	KESS F6	148.2400	33.8500	6325
36	KESS N1	148.3400	38.5100	5824
37	DART 21418	148.6940	38.7110	n.a.
38	DART 21413	152.1180	30.550	n.a.
39	DART 55023	153.5850	-14.8030	n.a.
40	DART 52402	154.1160	11.8830	n.a.
41	DART 52401	155.7660	19.2860	n.a.
42	DART 55012	158.5000	-15.8000	n.a.
43	DART 21416	163.4880	48.0440	n.a.
44	DART 52406	165.0810	-5.3320	n.a.
45	DART 21415	171.8490	50.1830	n.a.
46	DART 21414	178.2810	48.9380	n.a.
47	DART 51425	-176.2450	-9.4930	n.a.
48	DART d171	-170.7976	46.6369	n.a.
49	DART 46408	-169.8710	49.6260	n.a.
50	DART 51426	-168.0980	-22.9930	n.a.
51	DART d165	-165.0389	50.4405	4936
52	DART 46402	-164.0110	51.0690	n.a.
53	DART d157	-157.1640	52.5907	4484
54	DART 46403	-156.9320	52.6360	n.a.
55	DART 51407	-156.5160	19.6490	n.a.
56	DART 46405	-130.9090	42.9030	n.a.
57	DART d130	-130.9065	42.9065	3467
58	DART nemo	-130.0000	45.8610	n.a.
59	DART 46419	-129.6170	48.7620	n.a.
60	DART 46407	-128.9000	42.6040	n.a.
61	DART 46404	-128.7780	45.8590	n.a.
62	DART d128	-128.7720	45.8610	n.a.
63	DART 46411	-127.0130	39.3310	n.a.
64	DART d125	-125.0140	-8.4887	n.a.
65	DART 46412	-120.5610	32.4570	n.a.

66	DART 43412	-107.0010	16.0340	n.a.
67	DART 32412	-86.3920	-17.9750	n.a.
68	DART 32401	-74.8130	-19.5470	n.a.
Atlantic Ocean				
69	DART 32411	-90.6850	4.9230	n.a.
70	DART 42409	-85.7910	26.6580	n.a.
71	DART 41424	-72.4700	32.9280	n.a.
72	DART 44402	-70.5940	39.4870	n.a.
73	DART 42407	-68.2460	15.2560	n.a.
74	DART 41421	-63.9010	23.3990	n.a.
75	MOVE M3b	-60.5053	16.3333	4951
76	MOVE M1a	-60.5050	16.3400	4944
77	MOVE M3c	-60.4963	16.3475	4939
78	MOVE M2b	-57.0027	15.9403	5008
79	MOVE M2	-56.9500	15.9867	4978
80	MOVE M6	-56.6797	20.5918	5093
81	MOVE M1	-51.5265	15.4502	4965
82	MOVE M1b	-51.5100	15.4500	4967
83	DART 44401	-50.0000	37.5620	n.a.

References

Baur, O., Kuhn, M. & Featherstone, W. E. (2013). Continental mass change from GRACE over 2002-2011 and its impact on sea level, *J. Geod.*, **87**, 117–125, doi:10.1007/s00190-012-0583-2.

Bergmann, I. & Dobslaw, H. (2012). Short-term transport variability of the Antarctic Circumpolar Current from satellite gravity observations, *J. Geophys. Res.*, **117**, C05,044, doi:10.1029/2012JC007872.

Bergmann, I., Ramillien, G. & Frappart, F. (2012). Climate-driven interannual ice mass evolution in Greenland, *Global Planet. Change*, **82-83**, 1–11, doi:10.1016/j.gloplacha.2011.11.005.

Bergmann-Wolf, I., Dill, R., Forootan, E., Klemann, V., Kusche, J., Sasgen, I. & Dobslaw, H. (2014). *Updating ESA's Earth System Model for Gravity Mission Simulation Studies: 2. Comparison with the Original Model*, *Tech. rep.*, GFZ German Research Centre for Geosciences, doi:doi:10.2312/GFZ.b103-14088.

Bergmann-Wolf, I., Zhang, L. & Dobslaw, H. (2014). Global Eustatic Sea-Level Variations for the Approximation of Geocenter Motion from GRACE, *J. Geod. Sci.*, **4**, 37–48, doi:10.2478/jogs-2014-0006.

Bettadpur, S. V. (2012). *GRACE 327-742 UTCSR Level-2 Processing Standards Document (For Level-2 Product Release 05)*, *Tech. rep.*, Centre for Space Research, The University of Texas at Austin.

Beutler, G., Jaeggi, A., Mervart, L. & Meyer, U. (2010). The celestial mechanics approach: application to data of the GRACE mission, *J. Geod.*, **84**, 661–681, doi:10.1007/s00190-010-0402-6.

Bingham, R. J. & Hughes, C. W. (2006). Observing seasonal bottom pressure variability in the North Pacific with GRACE, *Geophys. Res. Lett.*, **33**, L08,607, doi:10.1029/2005GL025489.

Bingham, R. J. & Hughes, C. W. (2008). Determining North Atlantic meridional transport variability from pressure on the western boundary: A model investigation, *J. Geophys. Res.*, **113**, C09,008, doi:10.1029/2007JC004679.

Bingham, R. J. & Hughes, C. W. (2009). Geostrophic dynamics of meridional transport variability in the subpolar North Atlantic, *J. Geophys. Res.*, **114**, C12,029, doi:10.1029/2009JC005492.

Blewitt, G., Lavallée, D., Clarke, P. & Nurutdinov, K. (2001). A new global mode of Earth deformation: seasonal cycle detected., *Science (New York, N.Y.)*, **294**, 2342–5, doi:10.1126/science.1065328.

Bonin, J. A. & Chambers, D. P. (2011). Evaluation of high-frequency oceanographic signal in GRACE data: Implications for de-aliasing, *Geophys. Res. Lett.*, **38**, L17,608, doi:10.1029/2011GL048881.

Böning, C., Timmermann, R., Danilov, S. & Schröter, J. (2010). Antarctic circumpolar current transport variability in grace gravity solutions and numerical ocean model simulations, in: *System Earth via Geodetic-Geophysical Space Techniques*, edited by Flechtner, F. M., Gruber, T., Güntner, A., Mandea, M., Rothacher, M., Schöne, T. & Wickert, J., Advanced Technologies in Earth Sciences, Springer Berlin Heidelberg, p. 187–199, doi:10.1007/978-3-642-10228-8_15.

Böning, C., Timmermann, R., Macrander, A. & Schröter, J. (2008). A pattern-filtering method for the determination of ocean bottom pressure anomalies from GRACE solutions, *Geophys. Res. Lett.*, **35**, L18,611, doi:10.1029/2008GL034974.

Bruinsma, S., Lemoine, J.-M., Biancale, R. & Valès, N. (2010). CNES/GRGS 10-day gravity field models (release 2) and their evaluation, *Adv. Space Res.*, **45**, 587–601, doi:10.1016/j.asr.2009.10.012.

Butterworth, S. (1930). On the Theory of Filter Amplifiers, *Experimental Wireless and the Wireless Engineer*, **7**, 536–541, URL `www.gonascent.com/papers/butter.pdf`.

Carrere, L. & Lyard, F. (2003). Modeling the barotropic response of the global ocean to atmospheric wind and pressure forcing - comparisons with observations, *Geophys. Res. Lett.*, **30**, 1275, doi:10.1029/2002GL016473.

Cazenave, A., Dominh, K., Guinehut, S., Berthier, E., Llovel, W., Ramillien, G., Ablain, M. & Larnicol, G. (2009). Sea level budget over 2003-2008: A reevaluation from GRACE space gravimetry, satellite altimetry and Argo, *Global Planet. Change*, **65**, 83–88, doi:10.1016/j.gloplacha.2008.10.004.

Chambers, D., Wahr, J., Tamisiea, M. & Nerem, R. (2010). Ocean mass from GRACE and glacial isostatic adjustment, *J. Geophys. Res.*, **115**, B11,415, doi:10.1029/2010JB007530.

Chambers, D. P. (2004). Preliminary observations of global ocean mass variations with GRACE, *Geophys. Res. Lett.*, **31**, L13,310, doi:10.1029/2004GL020461.

Chambers, D. P. (2009). Calculating trends from GRACE in the presence of large changes in continental ice storage and ocean mass, *Geophys. J. Int.*, **176**, 415–419, doi:10.1111/j.1365-246X.2008.04012.x.

Chambers, D. P. (2011). ENSO-correlated fluctuations in ocean bottom pressure and wind-stress curl in the North Pacific, *Ocean Sci.*, **7**, 685–692, doi:10.5194/os-7-685-2011.

Chambers, D. P. & Bonin, J. A. (2012). Evaluation of Release-05 GRACE time-variable gravity coefficients over the ocean, *Ocean Sci.*, **8**, 859–868, doi:10.5194/os-8-859-2012.

Chambers, D. P. & Schroeter, J. (2011). Measuring ocean mass variability from satellite gravimetry, *J. Geodyn.*, **52**, 333–343, doi:10.1016/j.jog.2011.04.004.

Chambers, D. P. & Willis, J. K. (2008). Analysis of large-scale ocean bottom pressure variability in the North Pacific, *J. Geophys. Res.*, **113**, doi:10.1029/2008JC004930.

Chambers, D. P. & Willis, J. K. (2009). Low-frequency exchange of mass between ocean basins, *J. Geophys. Res.*, **114**, C11,008, doi:10.1029/2009JC005518.

Chen, J., Rodell, M., Wilson, C. & Famiglietti, J. (2005). Low degree spherical harmonic influences on Gravity Recovery and Climate Experiment (GRACE) water storage estimates, *Geophys. Res. Lett.*, **32**, doi:10.1029/2005GL022964.

Chen, J. L. & Wilson, C. R. (2008). Low degree gravity changes from GRACE, Earth rotation, geophysical models, and satellite laser ranging, *J. Geophys. Res.*, **113**, doi:10.1029/2007JB005397.

Chen, J. L., Wilson, C. R., Eanes, R. J. & Nerem, R. S. (1999). Geophysical interpretation of observed geocenter variations, *J. Geophys. Res.*, **104**, 2683, doi:10.1029/1998JB900019.

Cheng, M., Shum, C. & Tapley, B. (1997). Determination of long-term changes in the Earth's gravity field from satellite laser ranging observations, *J. Geophys. Res.*, **102**, 22,377–22,390, doi:10.1029/97JB01740.

Cheng, M., Tapley, B. & Ries, J. (2010). Geocenter Variations from Analysis of SLR data, in: *IAG Commission 1 Symposium (2010), Marne-Le-Vallee, France*.

Cheng, X., Li, L., Du, Y., Wang, J. & Huang, R.-X. (2013). Mass-induced sea level change in the northwestern North Pacific and its contribution to total sea level change, *Geophys. Res. Lett.*, **40**, 3975–3980, doi:10.1002/grl.50748.

Christensen, J., Krishna Kumar, K., Aldrian, E., An, S.-I., Cavalcanti, I., de Castro, M., Dong, W., Goswami, P., Hall, A., Kanyanga, J., Kitoh, A., Kossin, J., Lau, N.-C., Renwick, J., Stephenson, D., S.-P., X. & Zhou, T. (2013). Climate Phenomena and their Relevance for Future Regional Climate Change, in: *Climate Change 2013: The Physical Science Basis. Cortribution of Working Group I to the Fifth Assessment Report of the Intergorvernmental Panel on Climate Change*, edited by Stocker, T., Qin, D., Plattner, G.-K., Tignor, M., Allen, S., Boschung, J., Nauels, A., Xia, Y., Bex, V. & Midgley, P., Cambridge University Press, Cambridge, United Kingdom and New York, NY, USA, URL `http://www.ipcc.ch/report/ar5/wg1/`.

Church, J., Clark, P., Cazenave, A., Gregory, J., Jevrejeva, S., Levermann, A., Merrifield, M., Milne, G., Nerem, R., Nunn, P., Payne, A., Pfeffer, W., Stammer, D. & Unnikrishnan, A. (2013). Sea Level Change, in: *Climate Change 2013: The Physical Science Basis. Contribution of Workinggroup I to the Fifth Assessment Report of the Intergovernmental Panel on Climate Change*, edited by Stocker, T., Qin, D., Plattner, G.-K., Tignor, M., Allen, S., Boschung, J., Nauels, A., Xia, Y., Bex, V. & Midgley, P., Cambridge University Press, Cambridge, United Kingdom and New York, NY, USA, URL `http://www.ipcc.ch/report/ar5/wg1/`.

Clarke, P., Lavallee, D., Blewitt, G., van Dam, T. & Wahr, J. (2005). Effect of gravitational consistency and mass conservation on seasonal surface mass loading models, *Geophys. Res. Lett.*, **32**, doi:10.1029/2005GL022441.

Cox, C. & Chao, B. (2002). Detection of a large-scale mass redistribution in the terrestrial system since 1998, *SCIENCE*, **297**, 831–833, doi:10.1126/science.1072188.

Crétaux, J.-F. (2002). Seasonal and interannual geocenter motion from SLR and DORIS measurements: Comparison with surface loading data, *J. Geophys. Res.*, **107**, 2374, doi:10.1029/2002JB001820.

Cromwell, D., Shaw, A. G. P., Challenor, P., Houseago-Stokes, R. E. & Tokmakian, R. (2007). Towards measuring the meridional overturning circulation from space, *Ocean Sci.*, **3**, 223–228, doi:10.5194/os-3-223-2007.

Cunningham, S., Alderson, S., King, B. & Brandon, M. (2003). Transport and variability of the Antarctic Circumpolar Current in Drake Passage, *J. Geophys. Res.*, **108**, doi:10.1029/2001JC001147.

Cunningham, S. & Pavic, M. (2007). Surface geostrophic currents across the Antarctic circumpolar current in Drake Passage from 1992 to 2004, *Prog. Oceanogr.*, **73**, 296–310, doi:10.1016/j.pocean.2006.07.010.

Dahle, C. (2014). Release Notes for GFZ GRACE Level-2 Products - version RL05, Last update: 02.06.2014, www.isdc.gfz-potsdam.de.

Dahle, C., Flechtner, F., Gruber, C., könig, C., König, R., Michalak, G. & Neumayer, K.-H. (2012). *GFZ GRACE Level-2 Processing Standards Document for Level-2 Product Release 0005*, *Tech. rep.*, Deutsches GeoForschungsZentrum, doi:10.2312/GFZ.b103-12020.

Davis, J. L. (2004). Climate-driven deformation of the solid Earth from GRACE and GPS, *Geophys. Res. Lett.*, **31**, L24,605, doi:10.1029/2004GL021435.

Dee, D. P., Uppala, S. M., Simmons, A. J., Berrisford, P., Poli, P., Kobayashi, S., Andrae, U., Balmaseda, M. A., Balsamo, G., Bauer, P., Bechtold, P., Beljaars, A. C. M., van de Berg, L., Bidlot, J., Bormann, N., Delsol, C., Dragani, R., Fuentes, M., Geer, A. J., Haimberger, L., Healy, S. B., Hersbach, H., Hólm, E. V., Isaksen, L., Kå llberg, P., Köhler, M., Matricardi, M., McNally, A. P., Monge-Sanz, B. M., Morcrette, J.-J., Park, B.-K., Peubey, C., de Rosnay, P., Tavolato, C., Thépaut, J.-N. & Vitart, F. (2011). The ERA-Interim reanalysis: configuration and performance of the data assimilation system, *Q. J. Roy. Meteor. Soc.*, **137**, 553–597, doi:10.1002/qj.828.

Dickey, J., Marcus, S., de Viron, O. & Fukumori, I. (2002). Recent Earth oblateness variations: Unraveling climate and postglacial rebound effects, *SCIENCE*, **298**, 1975–1977, doi:10.1126/science.1077777.

Dill, R. (2008). *Hydrological model LSDM for operational Earth rotation and gravity field variations*, *Tech. rep.*, GFZ German Research Centre for Geosciences, doi:11.2312/GFZ.b103-08095.

Dill, R. & Dobslaw, H. (2013). Numerical simulations of global-scale high-resolution hydrological crustal deformations, *J. Geophys. Res.*, **118**, 5008–5017, doi:10.1002/jgrb.50353.

Dobslaw, H., Bergmann-Wolf, I., Dill, R., Forootan, E., Klemann, V., Kusche, J. & Sasgen, I. (2014). *Updating ESA's Earth System Model for Gravity Mission Simulation Studies:*

1. Model Description and Validation, *Tech. rep.*, GFZ German Research Centre for Geosciences, doi:10.2312/GFZ.b103-14079.

Dobslaw, H., Bergmann-Wolf, I., Forootan, E., Dahle, C., Mayer-Gürr, T., Kusche, J. & Flechtner, F. (2016). Modeling of Present-Day Atmosphere and Ocean Non-Tidal De-Aliasing Errors for Future Gravity Mission Simulations, *J. Geod.*, 1–14.

Dobslaw, H., Flechtner, F., Bergmann-Wolf, I., Dahle, C., Dill, R., Esselborn, S., Sasgen, I. & Thomas, M. (2013). Simulating high-frequency atmosphere-ocean mass variability for dealiasing of satellite gravity observations: AOD1B RL05, *J. Geophys. Res.*, **118**, 3704–3711, doi:10.1002/jgrc.20271.

Dobslaw, H. & Thomas, M. (2007). Simulation and observation of global ocean mass anomalies, *J. Geophys. Res.*, **112**, C05,040, doi:10.1029/2006JC004035.

Drijfhout, S., Heinze, L. M., C. & Maier-Reimer, E. (1996). Mean circulation and internal variability in an ocean primitive equation model, *J. Phys. Oceanogr.*, **26**, 559–580, doi:10.1175/1520-0485(1996)026<0559:MCAIVI>2.0.CO;2.

Dziewonski, A. M. & Anderson, D. L. (1981). Preliminary reference Earth model, *Phys. Earth Planet Int.*, **25**, 297 – 356, doi:http://dx.doi.org/10.1016/0031-9201(81)90046-7.

Eanes, R. (2000). SLR solutions from the University of Texas Center for Space Research, Geocenter from TOPEX SLR/DORIS, 1992-2000, http://sbgg.jpl.nasa.gov/dataset.html, IERS Spec. Bur. for Gravity/Geocent., Pasadena, Calif.

Ettema, J., van den Broeke, M. R., van Meijgaard, E., van de Berg, W. J., Bamber, J. L., Box, J. E. & Bales, R. C. (2009). Higher surface mass balance of the Greenland ice sheet revealed by high-resolution climate modeling, *Geophys. Res. Lett.*, **36**, L12,501, doi:10.1029/2009GL038110.

Farrell, W. E. & Clark, J. A. (1976). On postglacial sea level, *Geophys. J. Int.*, **46**, 647–667, doi:10.1111/j.1365-246X.1976.tb01252.x.

Fasullo, J. T., Boening, C., Landerer, F. W. & Nerem, R. S. (2013). Australia's unique influence on global sea level in 2010-2011, *Geophys. Res. Lett.*, **40**, 4368–4373, doi:10.1002/grl.50834.

Flechtner, F. (2007). *GRACE AOD1B Product Description Document for Product Releases 01 to 04, GRACE 327-750*, *Tech. rep.*, Deutsches GeoForschungsZentrum.

Flechtner, F. & Dobslaw, H. (2013). *AOD1B Product Description Document for Product Release 05*, *Tech. rep.*, Deutsches GeoForschungsZentrum.

Flechtner, F., Neumayer, K.-H., Dahle, C., Dobslaw, H., Fagiolini, E., Raimondo, J.-C. & Güntner, A. (2015). What can be expected from the GRACE-FO Laser Ranging Interferometer for Earth Science applications, *Surv. Geophys.*, submitted.

Fletcher, R. (1971). *A Modified Marquardt Subroutine for Non-Linear Least Squares*, *Tech. rep.*, United Kingdom Atomic Energy Authority, Harwell, Berkshire, England.

Fritsche, M., Dietrich, R. & Rülke, A. (2010). Low-degree earth deformation from reprocessed GPS observations, *GPS Solut.*, **14**, 165–175, doi:10.1007/s10291-009-0130-7.

Gill, A. E. & Niiler, P. P. (1973). The theory of the seasonal variability in the ocean, *Deep-Sea Res.*, **20**, 141–177, doi:10.1016/0011-7471(73)90049-1.

Gille, S. T. (2008). Decadal-scale temperature trends in the Southern Hemisphere ocean, *J. Clim.*, **21**, 4749–4765, doi:10.1175/2008JCLI2131.1.

Gille, S. T., Stevens, D. P., Tokmakian, R. T. & Heywood, K. J. (2001). Antarctic Circumpolar Current response to zonally averaged winds, *J. Geophys. Res.*, **106**, 2743, doi:10.1029/1999JC900333.

Godin, G. (1972). *The Analysis of Tides*, University of Toronto Press, Toronto, ISBN-13: 978-0802017475.

Gommenginger, C., Thibaut, P., Fenoglio-Marc, L., Quartly, G., Deng, X., Gomez-Enri, J., Challenor, P. & Gao, Y. (2011). Retracking Altimeter Waveforms Near the Coasts, in: *Coastal Altimetry*, edited by Vignudelli, S., Kostianoy, A. G., Cippolini, P. & Benveniste, J., Springer, Berlin, p. 61–101, doi:10.1007/978-3-642-12796-0.

Gruber, T., Bamber, J. L., Bierkens, M. F. P., Dobslaw, H., Murböck, M., Thomas, M., van Beek, L. P. H., van Dam, T., Vermeersen, L. L. a. & Visser, P. N. a. M. (2011). Simulation of the time-variable gravity field by means of coupled geophysical models, *Earth System Science Data*, **3**, 19–35, doi:10.5194/essd-3-19-2011.

Gruber, T., Murböck, M., Baldesarra, M., Brieden, P., Danzmann, K., Daras, I., Doll, B., Feili, D., Flechtner, F., Flury, J., Heinzel, G., Iran, P. S., Kusche, J., Langemann, M., Löcher, A., Müller, J., Müller, V., Naeimi, M., Pail, R., Raimondo, J., Reiche, J. C., Reubelt, T., Sheard, B., Sneeuw, N. & Wang, X. (2014). *e^2.motion, Earth System Mass Transport Mission (Square), - Concept for a Next Generation Gravity Field Mission - Final Report of Project "Satellite Gravimetry of the Next Generation (NGGM-D)"*, *Tech. rep.*, Technische Universität München.

Hagemann, S. & Dümenil, L. (1997). A parametrization of the lateral waterflow for the global scale, *Clim. Dynam.*, **14**, 17–31, doi:10.1007/s003820050205.

Heiskanen, W. & Moritz, H. (1967). *Physical Geodesy*, Freeman, San Francisco.

Hibler, I., W. D. (1979). A dynamic thermodynamic sea ice model, *J. Phys. Oceanogr.*, **9**, 815–846, doi:10.1175/1520-0485(1979)009<0815:ADTSIM>2.0.CO;2.

Hughes, C. W. (2003). Coherence of Antarctic sea levels, Southern Hemisphere Annular Mode, and flow through Drake Passage, *Geophys. Res. Lett.*, **30**, 1464, doi:10.1029/2003GL017240.

Hughes, C. W., Meredith, M. P. & Heywood, K. J. (1999). Wind-Driven Transport Fluctuations through Drake Passage: A Southern Mode, *J. Phys. Oceanogr.*, **29**, 1971–1992, doi:10.1175/1520-0485(1999)029<1971:WDTFTD>2.0.CO;2.

Hughes, C. W., Tamisiea, M. E., Bingham, R. J. & Williams, J. (2012). Weighing the ocean: Using a single mooring to measure changes in the mass of the ocean, *Geophys. Res. Lett.*, **39**, L17,602, doi:10.1029/2012GL052935.

Huybrechts, P. (2002). Sea-level changes at the LGM from ice-dynamic reconstructions of the Greenland and Antarctic ice sheets during the glacial cycles, *Quaternary Sci. Rev.*, **21**, 203–231, doi:10.1016/S0277-3791(01)00082-8.

IOC (1985). Manual on Sea Level Measurement and Interpretation - Volume I: Basic Procedures, *Manual and Guides*, **14**, URL http://www.psmsl.org/train_and_info/training/manuals/.

Ivins, E. & James, T. (2005). Antarctic glacial isostatic adjustment: a new assessment, *Antarct. Sci.*, **17**, 541–553, doi:10.1017/S0954102005002968.

Jansen, M. J. F., Gunter, B. C. & Kusche, J. (2009). The impact of GRACE, GPS and OBP data on estimates of global mass redistribution, *Geophys. J. Int.*, **177**, 1–13, doi:10.1111/j.1365-246X.2008.04031.x.

Jekeli, C. (1981). *Alternative methods to smooth the Earth's gravity field*, *Tech. rep.*, Dep. of Geod. Sci. and Surv., Ohio State Univ., Columbus.

Jensen, L., Rietbroek, R. & Kusche, J. (2013). Land water contribution to sea level from GRACE and Jason-1 measurements, *J. Geophys. Res.*, **118**, 212–226, doi:10.1002/jgrc.20058.

Klees, R., Zapreeva, E. a., Winsemius, H. C. & Savenije, H. H. G. (2007). The bias in GRACE estimates of continental water storage variations, *Hydrol. Earth Syst. Sc.*, **11**, 1227–1241, doi:10.5194/hess-11-1227-2007.

Klemann, V. (2013). Surface Loading, in: *Lecture Notes from the Summer School of DFG SPP1257 Global Water Cycle*, vol. Heft 30, edited by Eicker, A. & J., K., Rheinische Friedrich-Wilhelms Universität, Institut für Geodäsie und Geoinformation.

Klemann, V. & Martinec, Z. (2011). Contribution of glacial-isostatic adjustment to the geocenter motion, *Tectonophysics*, **511**, 99–108, doi:10.1016/j.tecto.2009.08.031.

Koehl, A., Siegismund, F. & Stammer, D. (2012). Impact of assimilating bottom pressure anomalies from GRACE on ocean circulation estimates, *J. Geophys. Res.*, **117**, doi:10.1029/2011JC007623.

Kuhlmann, J., Dobslaw, H., Petrick, C. & Thomas, M. (2013). Ocean bottom pressure signals around Southern Africa from in situ measurements, satellite data, and modeling, *J. Geophys. Res.*, **118**, 4889–4898, doi:10.1002/jgrc.20372.

Kuhlmann, J., Dobslaw, H. & Thomas, M. (2011). Improved modeling of sea level patterns by incorporating self-attraction and loading, *J. Geophys. Res.*, **116**, C11,036, doi:10.1029/2011JC007399.

Kuhlmann, J., Rogozhina, I., Dill, R., Bergmann-Wolf, I. & Thomas, M. (2015). A method for reconstructing global ocean-induced surface displacements from land-based in-situ stations, *J. Geodyn.*, **83**, 18–27, doi:10.1016/j.jog.2014.10.003.

Kuhlmann, J., Thomas, M. & Schuh, H. (2013). Self-Attraction And Loading Of Oceanic Masses, in: *Handbook of Geomathematics*, vol. 1, edited by Freeden, W., Zuhair Nashed, M. & Sonar, T., Springer Verlag, URL http://springer.com/mathematics/applications/book/978-3-642-01545-8.

Kurtenbach, E. (2011). *Entwicklung eines Kalman-Filters zur Bestimmung kurzzeitiger Variationen des Erdschwerefeldes aus Daten der Satellitenmission GRACE*, Ph.D. thesis, Univ. of Bonn, Germany, URL http://nbn-resolving.de/urn:nbn:de:hbz:5N-25739.

Kurtenbach, E., Mayer-Gürr, T. & Eicker, A. (2009). Deriving daily snapshots of the Earth's gravity field from GRACE L1B data using Kalman filtering, *Geophys. Res. Lett.*, **36**, L17,102, doi:10.1029/2009GL039564.

Kusche, J. (2007). Approximate decorrelation and non-isotropic smoothing of time-variable GRACE-type gravity field models, *J. Geod.*, **81**, 733–749, doi:10.1007/s00190-007-0143-3.

Kusche, J., Schmidt, R., Petrovic, S. & Rietbroek, R. (2009). Decorrelated GRACE time-variable gravity solutions by GFZ, and their validation using a hydrological model, *J. Geod.*, **83**, 903–913, doi:10.1007/s00190-009-0308-3.

Kusche, J. & Schrama, E. (2005). Surface mass redistribution inversion from global GPS deformation and Gravity Recovery and Climate Experiment (GRACE) gravity data, *J. Geophys. Res.*, **110**, doi:10.1029/2004JB003556.

Lavallée, D. A., van Dam, T., Blewitt, G. & Clarke, P. J. (2006). Geocenter motions from GPS: A unified observation model, *J. Geophys. Res.*, **111**, B05,405, doi:10.1029/2005JB003784.

Li, C. & Wettstein, J. J. (2012). Thermally Driven and Eddy-Driven Jet Variability in Reanalysis, *J. Clim.*, **25**, 1587–1596, doi:10.1175/JCLI-D-11-00145.1.

Llovel, W., Willis, J. K., Landerer, F. W. & Fukumori, I. (2014). Deep-ocean contribution to sea level and energy budget not detectable over the past decade, *Nature Climate Change*, **4**, 1031–1035, doi:10.1038/NCLIMATE2387.

Lorbacher, K., Marsland, S. J., Church, J. A., Griffies, S. M. & Stammer, D. (2012). Rapid barotropic sea level rise from ice sheet melting, *J. Geophys. Res.*, **117**, C06,003, doi:10.1029/2011JC007733.

Lyard, F., Lefevre, F., Letellier, T. & Francis, O. (2006). Modelling the global ocean tides: modern insights from FES2004, *Ocean Dynam.*, **56**, 394–415, doi:10.1007/s10236-006-0086-x.

Macrander, A., Böning, C., Boebel, O. & Schröter, J. (2010). Validation of GRACE Gravity Fields by In-Situ Data of Ocean Bottom Pressure, in: *System Earth via Geodetic-Geophysical Space Techniques*, edited by Stroink, L., Mosbrugger, V., Wefer, G., Flechtner, F. M., Gruber, T., Güntner, A., Mandea, M., Rothacher, M., Schöne, T. & Wickert, J., Advanced Technologies in Earth Sciences, Springer Berlin Heidelberg, p. 169–185, doi:10.1007/978-3-642-10228-8_14.

Meredith, M. P. (2004). Changes in the ocean transport through Drake Passage during the 1980s and 1990s, forced by changes in the Southern Annular Mode, *Geophys. Res. Lett.*, **31**, L21,305, doi:10.1029/2004GL021169.

Meredith, M. P., Vassie, J. M., Heywood, K. J. & Spencer, R. (1996). On the temporal variability of the transport through Drake Passage, *J. Geophys. Res.*, **101**, 22,485–22,494, doi:10.1029/96JC02003.

Merrifield, M. A., Thompson, P. R. & Lander, M. (2012). Multidecadal sea level anomalies and trends in the western tropical Pacific, *Geophys. Res. Lett.*, **39**, doi:10.1029/2012GL052032.

Meyer, U., Jaeggi, A. & Beutler, G. (2012). Monthly gravity field solutions based on GRACE observations generated with the Celestial Mechanics Approach, *Earth Planet. Sci. Lett.*, **345**, 72–80, doi:10.1016/j.epsl.2012.06.026.

Mitchum, G., Nerem, R., Merrifield, M. & Gehrels, W. (2010). Modern Sea-Level-Change Estimates, in: *Understanding Sea-Level Rise and Variability*, edited by Church, J., Woodworth, P., Aarup, T. & Wilson, W., Blackwell Publishing Ltd., doi:10.1002/9781444323276.ch5.

Murray, T., Scharrer, K., James, T. D., Dye, S. R., Hanna, E., Booth, A. D., Selmes, N., Luckman, A., Hughes, A. L. C., Cook, S. & Huybrechts, P. (2010). Ocean regulation hypothesis for glacier dynamics in southeast Greenland and implications for ice sheet mass changes, *J. Geophys. Res.*, **115**, doi:10.1029/2009JF001522.

Olbers, D., Borowski, D., Völker, C. & Wölff, J.-O. (2004). The dynamical balance, transport and circulation of the Antarctic Circumpolar Current, *Antarct. Sci.*, **16**, 439–470, doi:10.1017/S0954102004002251.

Olbers, D. & Lettmann, K. (2007). Barotropic and baroclinic processes in the transport variability of the Antarctic Circumpolar Current, *Ocean Dynam.*, **57**, 559–578, doi:10.1007/s10236-007-0126-1.

Orsi, A., Whitworth III, T. & Nowlin Jr., W. (2001). Locations of the various fronts in the Southern Ocean, URL `http://data.aad.gov.au/aadc/metadata/metadata_redirect.cfm?md=AMD/AU/southern_ocean_fronts`.

Orsi, A. H., Whitworth, T. & Nowlin, W. D. (1995). On the meridional extent and fronts of the Antarctic Circumpolar Current, *Deep-Sea Res. Pt. I*, **42**, 641–673, doi:10.1016/0967-0637(95)00021-W.

Panet, I., Flury, J., Biancale, R., Gruber, T., Johannessen, J., van den Broeke, M. R., van Dam, T., Gegout, P., Hughes, C. W., Ramillien, G., Sasgen, I., Seoane, L. & Thomas, M. (2013). Earth System Mass Transport Mission (e.motion): A Concept for Future Earth Gravity Field Measurements from Space, *Surv. Geophys.*, **34**, 141–163, doi:10.1007/s10712-012-9209-8.

Park, J.-H., Watts, D. R., Donohue, K. A. & Jayne, S. R. (2008). A comparison of in situ bottom pressure array measurements with GRACE estimates in the Kuroshio Extension, *Geophys. Res. Lett.*, **35**, L17,601, doi:10.1029/2008GL034778.

Paulson, A., Zhong, S. & Wahr, J. (2007). Inference of mantle viscosity from GRACE and relative sea level data, *Geophys. J. Int.*, **171**, 497–508, doi:10.1111/j.1365-246X.2007.03556.x.

Peltier, W. R. (2004). Global glacial isostasy and the surface of the ice-age earth: The ice-5G (VM2) model and grace, *Annu. Rev. Earth Pl. Sc.*, **32**, 111–149, doi:10.1146/annurev.earth.32.082503.144359.

Peltier, W. R., Argus, D. F. & Drummond, R. (2015). Space geodesy constrains ice age terminal deglaciation: The global ICE-6G_C (VM5a) model, *J. Geophys. Res.*, **120**, 450–487, doi:10.1002/2014JB011176.

Petit, G. & Luzum, B. (2010). *IERS Convention (2010) (IERS Technical Note no. 36)*, *Tech. rep.*, Verlag des Bundesamtes für Kartographie und Geodäsie, Frankfurt am Main, URL http://www.iers.org/IERS/EN/Publications/TechnicalNotes/tn36.html.

Petrick, C., Dobslaw, H., Bergmann-Wolf, I., Schoen, N., Matthes, K. & Thomas, M. (2014). Low-frequency ocean bottom pressure variations in the North Pacific in response to time-variable surface winds, *J. Geophys. Res.*, **119**, 5190–5202, doi:10.1002/2013JC009635.

Pond, S. & Pickard, G. (1983). *Introductory Dynamical Oceanography*, Pergamon Press Ltd.

Ponte, R. (1999). A preliminary model study of the large-scale seasonal cycle in bottom pressure over the global ocean, *J. Geophys. Res.*, **104**, 1289–1300, doi:10.1029/1998JC900028.

Ponte, R. M. & Quinn, K. J. (2009). Bottom pressure changes around Antarctica and wind-driven meridional flows, *Geophys. Res. Lett.*, **36**, doi:10.1029/2009GL039060.

Quinn, K. & Ponte, R. (2010). Uncertainty in ocean mass trends from GRACE, *Geophys. J. Int.*, **181**, 762–768, doi:10.1111/j.1365-246X.2010.04508.x.

Ray, R. D. (1998). Ocean self-attraction and loading in numerical tidal models, *Mar. Geod.*, **21**, 181–192, doi:10.1080/01490419809388134.

Rietbroek, R., Brunnabend, S.-E., Dahle, C., Kusche, J., Flechtner, F., Schröter, J. & Timmermann, R. (2009). Changes in total ocean mass derived from GRACE, GPS, and ocean modeling with weekly resolution, *J. Geophys. Res.*, **114**, C11,004, doi:10.1029/2009JC005449.

Rietbroek, R., Fritsche, M., Brunnabend, S.-E., Daras, I., Kusche, J., Schröter, J., Flechtner, F. & Dietrich, R. (2012). Global surface mass from a new combination of GRACE, modelled OBP and reprocessed GPS data, *J. Geodyn.*, **59-60**, 64–71, doi:10.1016/j.jog.2011.02.003.

Rietbroek, R., Fritsche, M., Dahle, C., Brunnabend, S.-E., Behnisch, M., Kusche, J., Flechtner, F., Schroeter, J. & Dietrich, R. (2014). Can GPS-Derived Surface Loading Bridge a GRACE Mission Gap?, *Surv. Geophys.*, **35**, 1267–1283, doi:10.1007/s10712-013-9276-5.

Rietbroek, R., LeGrand, P., Wouters, B., Lemoine, J.-M., Ramillien, G. & Hughes, C. W. (2006). Comparison of in situ bottom pressure data with GRACE gravimetry in the Crozet-Kerguelen region, *Geophys. Res. Lett.*, **33**, L21,601, doi:10.1029/2006GL027452.

Rintoul, S. R., Hughes, C. & Olbers, D. (2001). The Antarctic Circumpolar Current System, in: *Ocean Circulation & Climate*, edited by Siedler, G., Church, J. & Gould, J., chap. 4.6, Academic Press, p. 271–302.

Riva, R. E. M., Bamber, J. L., Lavallee, D. A. & Wouters, B. (2010). Sea-level fingerprint of continental water and ice mass change from GRACE, *Geophys. Res. Lett.*, **37**, doi:10.1029/2010GL044770.

Robinson, I. (2004). *Measuring the Oceans from Space - The principles and methods of satellite oceanography*, Springer.

Rowlands, D. D., Luthcke, S. B., McCarthy, J. J., Klosko, S. M., Chinn, D. S., Lemoine, F. G., Boy, J. P. & Sabaka, T. J. (2010). Global mass flux solutions from GRACE: A comparison of parameter estimation strategies-Mass concentrations versus Stokes coefficients, *J. Geophys. Res.*, **115**, doi:10.1029/2009JB006546.

Rummel, R., Horwath, M., Yi, W., Albertella, A., Bosch, W. & Haagmans, R. (2011). GOCE, Satellite Gravimetry and Antarctic Mass Transports, *Surv. Geophys.*, 643–657, doi:10.1007/s10712-011-9115-5.

Sallée, J. B., Speer, K. & Morrow, R. (2008). Response of the Antarctic Circumpolar Current to Atmospheric Variability, *J. Climate*, **21**, 3020–3039, doi:10.1175/2007JCLI1702.1.

Saynisch, J., Bergmann-Wolf, I. & Thomas, M. (2015). Assimilation of GRACE-derived oceanic mass distributions with a global ocean circulation model, *J. Geod.*, **89**, 121–139, doi:10.1007/s00190-014-0766-0.

Saynisch, J. & Thomas, M. (2012). Ensemble Kalman-Filtering of Earth rotation observations with a global ocean model, *J. Geodyn.*, **62**, 24–29, doi:10.1016/j.jog.2011.10.003.

Schmidt, R., Flechtner, F., Meyer, U., Neumayer, K.-H., Dahle, C., König, R. & Kusche, J. (2008). Hydrological Signals Observed by the GRACE Satellites, *Surv. Geophys.*, **29**, 319–334, doi:10.1007/s10712-008-9033-3.

Siegismund, F., Romanova, V., Köhl, A. & Stammer, D. (2011). Ocean bottom pressure variations estimated from gravity, nonsteric sea surface height and hydrodynamic model simulations, *J. Geophys. Res.*, **116**, C07,021, doi:10.1029/2010JC006727.

Sneeuw, N., Flury, J. & Rummel, R. (2004). Science Requirements on Future Missions and Simulated Mission Scenarios, *Earth Moon Planets*, **94**, 113–142, doi:10.1007/s11038-004-7605-x.

Sokolov, S. & Rintoul, S. R. (2009). Circumpolar structure and distribution of the Antarctic Circumpolar Current fronts: 2. Variability and relationship to sea surface height, *J. Geophys. Res.*, **114**, C11,019, doi:10.1029/2008JC005248.

Song, Y. T. & Zlotnicki, V. (2008). Subpolar ocean bottom pressure oscillation and its links to the tropical ENSO, *Int. J. Remote Sens.*, **29**, 6091–6107, doi:10.1080/01431160802175538.

Stepanov, V. & Hughes, C. (2004). Parameterization of ocean self-attraction and loading in numerical models of the ocean circulation, *J. Geophys. Res.*, **109**, doi:10.1029/2003JC002034.

Stewart, R. (2008). *Introduction To Physical Oceanography*, Texas A & M University, URL `http://oceanworld.tamu.edu/resources/ocng_textbook/PDF_files/book_pdf_files.html`.

Storch, J.-S. V., Eden, C., Fast, I., Haak, H., Hernández-Deckers, D., Maier-Reimer, E., Marotzke, J. & Stammer, D. (2012). An Estimate of the Lorenz Energy Cycle for the World Ocean Based on STORM/NCEP Simulation, *J. Phys. Oceanogr.*, **42**, 2185–2205, doi:10.1175/JPO-D-12-079.1.

Swenson, S. (2002). Methods for inferring regional surface-mass anomalies from Gravity Recovery and Climate Experiment (GRACE) measurements of time-variable gravity, *J. Geophys. Res.*, **107**, 2193, doi:10.1029/2001JB000576.

Swenson, S., Chambers, D. & Wahr, J. (2008). Estimating geocenter variations from a combination of GRACE and ocean model output, *J. Geophys. Res.*, **113**, B08,410, doi:10.1029/2007JB005338.

Swenson, S. & Wahr, J. (2006). Post-processing removal of correlated errors in GRACE data, *Geophys. Res. Lett.*, **33**, doi:10.1029/2005GL025285.

Tamisiea, M. E. (2011). Ongoing glacial isostatic contributions to observations of sea level change, *Geophys. J. Int.*, **186**, 1036–1044, doi:10.1111/j.1365-246X.2011.05116.x.

Tamisiea, M. E., Hill, E. M., Ponte, R. M., Davis, J. L., Velicogna, I. & Vinogradova, N. T. (2010). Impact of self-attraction and loading on the annual cycle in sea level, *J. Geophys. Res.*, **115**, doi:10.1029/2009JC005687.

Tapley, B., Flechtner, F., Watkins, M. & Bettadpur, S. (2014). GRACE Mission: Status and Prospects, in: *GRACE Science Team Meeting 2014, Potsdam, Germany*.

Tapley, B. D. (2004). The gravity recovery and climate experiment: Mission overview and early results, *Geophys. Res. Lett.*, **31**, L09,607, doi:10.1029/2004GL019920.

Thomas, M., Sündermann, J. & Maier-Reimer, E. (2001). Consideration of ocean tides in an OGCM and impacts on subseasonal to decadal polar motion excitation, *Geophys. Res. Lett.*, **28**, 2457, doi:10.1029/2000GL012234.

Thompson, D. W. J. & Wallace, J. M. (2000). Annular Modes in the Extratropical Circulation. Part I: Month-to-Month Variability*, *J. Climate*, **13**, 1000–1016, doi:10.1175/1520-0442(2000)013<1000:AMITEC>2.0.CO;2.

Torge, W. (1991). *Geodesy*, Walter de Gruyter & Co., Berlin.

Tushingham, A. M. & Peltier, W. R. (1991). ICE-3G - A new global-model of late pleistocene deglaciation based upon geophysical predictions of postglacial relative sea-level change, *J. Geophys. Res.*, **96**, 4497–4523, doi:10.1029/90JB01583.

von Storch, H. & Zwiers, F. W. (2003). *Statistical Ananlysis in Climate Research*, Cambridge University Press.

Wahr, J., Molenaar, M. & Bryan, F. (1998). Time variability of the Earth's gravity field: Hydrological and oceanic effects and their possible detection using GRACE, *J. Geophys. Res.*, **103**, 30,205–30,229, doi:10.1029/98JB02844.

Wahr, J., Swenson, S. & Velicogna, I. (2006). Accuracy of GRACE mass estimates, *Geophys. Res. Lett.*, **33**, doi:10.1029/2005GL025305.

Watkins, M. M. & Yuan, D.-N. (2012). *GRACE JPL Level-2 Processing Standards Document For Level-2 Product Release 05*, *Tech. rep.*, Jet Propulsion Laboratory.

Watts, D. R. & Kontoyiannis, H. (1990). Deep-Ocean Bottom Pressure Measurements: Drift Removal and Perfomance, *J. Atmos. Ocean. Tech.*, **7**, 296–306, doi:10.1175/1520-0426(1990)007<0296:DOBPMD>2.0.CO;2.

Wearn, R. B. & Baker, D. (1980). Bottom pressure measurements across the Antarctic circumpolar current and their relation to the wind, *Deep-Sea Res.*, **27**, 875–888, doi:10.1016/0198-0149(80)90001-1.

Weijer, W. & Gille, S. T. (2005). Adjustment of the Southern Ocean to Wind Forcing on Synoptic Time Scales, *J. Phys. Oceanogr.*, **35**, 2076–2089, doi:10.1175/JPO2801.1.

Whitworth III, T. & Peterson, R. G. (1985). Volume transport of the Antarctic Circumpolar Current from bottom pressure measurements, *J. Phys. Oceanogr.*, **15**, 810–816.

Wiese, D. N., Folkner, W. M. & Nerem, R. S. (2009). Alternative mission architectures for a gravity recovery satellite mission, *J. Geod.*, **83**, 569–581, doi:10.1007/s00190-008-0274-1.

Wolff, J., Maier-Reimer, E. & Legutke, S. (1996). *The Hamburg Ocean Primitive Equation Model HOPE*, *Tech. rep.*

Woodworth, P., Hughes, C., Blackman, D., Stepanov, V., Holgate, S., Foden, P., Pugh, J., Mack, S., Hargreaves, G., Meredith, M., Milinevsky, G. & Contreras, J. F. (2006). Antarctic Peninsula sea levels: a real-time system for monitoring Drake Passage transport, *Antarct. Sci.*, **18**, 429–436, doi:10.1017/S0954102006000472.

Wouters, B., Riva, R. E. M., Lavallée, D. A. & Bamber, J. L. (2011). Seasonal variations in sea level induced by continental water mass: First results from GRACE, *Geophys. Res. Lett.*, **38**, L03,303, doi:10.1029/2010GL046128.

Wu, X., Heflin, M. B., Ivins, E. R. & Fukumori, I. (2006). Seasonal and interannual global surface mass variations from multisatellite geodetic data, *J. Geophys. Res.*, **111**, doi:10.1029/2005JB004100.

Wunsch, C. & Stammer, D. (1997). Atmospheric loading and the oceanic "inverted barometer" effect, *Rev. Geophys.*, **35**, 79, doi:10.1029/96RG03037.

Zenner, L., Bergmann-Wolf, I., Dobslaw, H., Gruber, T., Guentner, A., Wattenbach, M., Esselborn, S. & Dill, R. (2014). Comparison of Daily GRACE Gravity Field and Numerical Water Storage Models for De-aliasing of Satellite Gravimetry Observations, *Surv. Geophys.*, **35**, 1251–1266, doi:10.1007/s10712-014-9295-x.

Zenner, L., Fagiolini, E., Daras, I., Flechtner, F., Gruber, T., Schmidt, T. & Schwarz, G. (2012). Non-tidal atmospheric and oceanic mass variations and their impact on GRACE data analysis, *J. Geodyn.*, **59-60**, 9–15, doi:10.1016/j.jog.2012.01.010.

Zhong, S., Paulson, A. & Wahr, J. (2003). Three-dimensional finite-element modelling of Earth's viscoelastic deformation: effects of lateral variations in lithospheric thickness, *Geophys. J. Int.*, **155**, 679–695, doi:10.1046/j.1365-246X.2003.02084.x.

Zlotnicki, V., Wahr, J., Fukumori, I. & Song, Y. T. (2007). Antarctic Circumpolar Current Transport Variability during 2003-05 from GRACE, *J. Phys. Oceanogr.*, **37**, 230–244, doi:10.1175/JPO3009.1.

Zweck, C. & Huybrechts, P. (2005). Modeling of the northern hemisphere ice sheets during the last glacial cycle and glaciological sensitivity, *J. Geophys. Res.*, **110**, doi:10.1029/2004JD005489.

Acknowledgement

First I would like to thank Maik Thomas and Henryk Dobslaw for giving me the chance to do a doctorate right after the end of my study and having the confidence in me therefore, even I was not sure about it at this moment. Again, I thank Henryk for the good supervision of my work through the last four years, helping me with problems but still focussing on finding solutions by myself even if it meant repeating tests over and over again until the results were plausible for at least one of us.
I would also like to thank my colleagues of section 1.3 at GFZ for the friendly working atmosphere and the acceptance of an error loving, well-adjusted geodesists in their community of fanatic theorists and modelers. Many thanks goes to Volker Klemann, who improved not only the layout of this work due to his longtime knowledge of LaTeX but also explaining complex physical process to me in an comprehensively way when I was lost in the purely theoretical aspects.
A special thanks goes to my former colleague Jan Dostal, who shared the office with me for three years and became a good friend with whom I could talk about even delicate issues.
At last, I would like to thank my husband Ronny for his patience with me during these years and dealing with my temper, building me up if again one of the re-computations went wrong for what felt like the hundredth time and giving me besides him the most important person in my life, our little daughter Hannah.

This work has been supported by Deutsche Forschungsgemeinschaft within the priority program SPP1257 “Mass Transport and Mass Distribution in the System Earth” under grant DO1311/2-1 and by the German Federal Ministry of Education and Research (BMBF) within the FONA research program under the grants 03F0654A and 01LP1151A.